UNIVERSITY OF CALIFORNIA, SAN DIEGO

Design and Development of Integrated Multi–Modal Scanning Probe Micrscopy for Structure–Function Imaging of Ion Channels and Receptors

A dissertation submitted in partial satisfaction of the
requirements for the degree
Doctor of Philosophy

in

Bioengineering

by

Brian Richard Meckes

Committee in charge:

Professor Ratnesh Lal, Chair
Professor Gert Cauwenberghs
Professor Renkun Chen
Professor David Kleinfeld
Professor Padmini Rangamani

2015

The dissertation of Brian Richard Meckes is approved, and it is acceptable in quality and form for publication on microfilm and electronically:

_____

_____

_____

_____

_____
Chair

University of California, San Diego

2015

DEDICATION

To Jeanie, my loving and supportive wife

EPIGRAPH

As for all I can tell, the only difference is that what many see we call a real thing, and what only one sees we call a dream.

—CS Lewis

TABLE OF CONTENTS

LIST OF FIGURES

LIST OF TABLES

ACKNOWLEDGEMENTS

First and foremost, I would like to acknowledge my co-advisor Dr. Gina Sosinsky, who recently passed away. She served as the co-sponsor for my NIH fellowship, but more importantly, she was an exceptional teacher and mentor to me during my graduate studies. I am forever greatful for the instruction on the biology of gap junctions that she gave me. During the time that I knew her, she always put a lot of thought and care into her instruction and mentorship, which was representative of her work as a scientist and professor. Her passing will leave a tremendous void in the university and scientific community as a whole.

Any further acknowledgment must first begin with my wife, Jeanie. She has been a constant source of encouragement and wisdom. I know I owe her for any success I have and will achieve. Next, I would like to thank my parents for all the years of support and guidance, which has contributed significantly to this work in many intangible ways. My siblings, Joy, Jameson, and Christopher, also deserve special mention for constantly being there.

The work completed in my dissertation relied upon the collaboration of a multitude of bright and talented people. To start with, I cannot express enough gratitude to my advisor and committee chair, Dr. Ratnesh Lal. He was a creative influence on all the work I have accomplished and taught me how to be a persuasive scientist. I would like to thank Dr. Renkun Chen who gave me advice on microfabrication when I did not have a clue of where to start. I would like to thank my other committee members, Dr. Gert Cauwenbergs, Dr. David Kleinfeld, and Dr. Padmini Rangamani for being supportive and providing feedback on my dissertation.

I need to thank the members of the Lal Lab for Nano-Bio-Imaging and Devices for their help on all of my research. In particular, I would like to thank Dr. Fernando Teran Arce who taught me AFM. Dr. Laura Connelly was instrumental in the realization of the nanopore support system. I would also like to thank Dr. Alan Gillman and Joon Lee for good scientific advice and good times. I would also like to thank Cinzia Ambrosi from Dr. Sosinky's laboratory who taught me how to purify, prepare, and characterize my connexin samples. I appreciate

the help and support of my friends, Dr. Nikhil Rao and Dr. Gaurav Kaushik for discussions of science and "frou".

Additionally, I would like to thank my collaborators who made much of this work possible. Dr. Lital Alfonta and her laboratory at Ben Gurion University greatly contributed to my bacterial studies. Dr. Meni Wanunu and his graduate students Josjeph Larkin and Pradeep Waduge at Northeastern University were instrumental in their support for graphene nanopore preparations.

Finally, I would like to acknowledge the funding sources that made this work possible. The NIH awarded me with a predoctoral fellowship (F31DA034562) that allowed me to complete this work. NIH grants R01DA025296, R01AG028709, R01DA024871 (R.L), and R01GM065937 (G.S) provided project funding.

Chapter 2, in full, is a reprint of the material Meckes B, Arce F T, Connelly L S, Lal R. Insulated Conducting Cantilevered Nanotips and Two-Chamber Recording System for High Resolution Ion Sensing AFM. Scientific Reports. 2014; 4: 4454. The dissertation author was the primary author.

Chapter 3, in full, is a reprint of the material Alfonta L*, Meckes B*, Amir L, Schlesinger O, Ramachandran S, Lal R. Measuring Localized Redox Enzyme Electron Transfer in a Live Cell with Conducting Atomic Force Microscopy. Analytical Chemistry. 2014; 86(15):7674–80. The dissertation author was the primary author.

Chapter 4, in full, is a reprint of the material Meckes B, Ambrosi C, Barnard H, Arce F T, Sosinsky G E, Lal R. Atomic Force Microscopy Shows Connexin26 Hemichannel Clustering in Purified Membrane Fragments. Biochemistry. 2014; 53(47):7407-14 The dissertation author was the primary author.

Chapter 5, in full, is a reprint of the material Connelly L S*, Meckes B*, Larkin J, Gillman A L, Wanunu M, Lal R. Graphene nanopore support system for simultaneous high–resolution AFM imaging and conductance measurements. ACS Applied Materials & Interfaces. 6(7):5290–6. The dissertation author was the primary author.

Chapter 6, in part, is a publication in preparation with Meckes B, Connelly L C, Ambrosi C, Waduge P, Wanunu M, Sosinsky G S, Lal R. The dissertation

author was the primary author.

Chapter 7, in part, is a publication in preparation with Meckes B, Yang Q, Lal R. The dissertation author was the primary author.

VITA

2009	B. S. B. in Bioengineering *cum laude*, Rice Univerisity
2012	C. Phil. in Bioengineering, University of California, San Diego
2015	Ph. D. in Bioengineering, University of California, San Diego

PUBLICATIONS

*Indicates equal authorship

Meckes B, Ambrosi C, Barnard H, Arce F T, Sosinsky G E, Lal R. Atomic Force Microscopy Shows Connexin26 Hemichannel Clustering in Purified Membrane Fragments. Biochemistry. 2014; 53(47):7407-14.

Landon P B, Lee J, Hwang M T, Mo A H, Neuberger A, **Meckes B**, Guiterrez J J, Glinsky G, Lal R. Energetically Biased DNA Motor Containing a Thermodynamically Stable Partial Strand Displacement State. Langmuir. 2014; 30(46):14073-8.

Alfonta L*, **Meckes B***, Amir L, Schlesinger O, Ramachandran S, Lal R. Measuring Localized Redox Enzyme Electron Transfer in a Live Cell with Conducting Atomic Force Microscopy. Analytical Chemistry. 2014; 86(15):7674–80.

Meckes B, Arce F T, Connelly L S, Lal R. Insulated Conducting Cantilevered Nanotips and Two–Chamber Recording System for High Resolution Ion Sensing AFM. Scientific Reports. 2014; 4: 4454.

Connelly L S*, **Meckes B***, Larkin J, Gillman A L, Wanunu M, Lal R. Graphene nanopore support system for simultaneous high–resolution AFM imaging and conductance measurements. ACS Applied Materials & Interfaces. 6(7):5290–6.

Mo A H, Landon P B, **Meckes B**, Yang M M, Glinsky G V, Lal R. An on-demand four-way junction DNAzyme nanoswitch driven by inosine-based partial strand displacement. 2014; 6(3):1462-6.

Arce F T, **Meckes B**, Camp S M, Garcia J G N, Dudek S M, Lal R. Heterogeneous elastic response of human lung microvascular endothelial cells to barrier modulating stimuli. Nanomedicine: Nanotechnology, Biology, and Medicine. 2013; 9(7):875–84.

Leiske D L, **Meckes B**, Miller C E, Wu C Walker T W, Lin B, Meron M, Ketelson H A, Toney M F, Fuller G G. Insertion mechanism of a poly (ethylene oxide)–poly (butylene oxide) block copolymer into a DPPC monolayer. Langmuir. 2011; 27(18):11444–50.

Hwang M T, Landon P B, Lee J, Mo A, **Meckes B** Glinskii G, Lal R. DNA Nano-Carrier for Repeatable Capture and Release of Biomolecules. Nanoscale. 2015; DOI:10.1039/C5NR05124J

ABSTRACT OF THE DISSERTATION

Design and Development of Integrated Multi–Modal Scanning Probe Micrscopy for Structure–Function Imaging of Ion Channels and Receptors

by

Brian Richard Meckes

Doctor of Philosophy in Bioengineering

University of California, San Diego, 2015

Professor Ratnesh Lal, Chair

Understanding cellular behavior and tissue organization requires a deeper understanding of nanoscale structure and activity of proteins and biomacromolecules, including channels and receptors that act as messengers connecting the cell to its surrounding. Channels and receptors respond to a wide variety of electrical, chemical, and mechanical stimuli to facilitate cellular homeostasis, communication, migration, and survival. Ion channels facilitate the passage of ions and metabolites across cellular membranes and are visualized by high-resolution 3D imaging techniques, which include EM and scanning probe microscopies, such as atomic force microscopy (AFM) and scanning ion conductance microscopy (SICM).

However, the current imaging techniques are unable to obtain the intertwined direct relationships between structure and electrical activity of ion channels. My work is dedicated to designing and implementing such an integrated system. This dissertation describes the details about different novel AFM–based nanotechnologies designed and developed for simultaneous structure–activity imaging of various electrically active biological systems. First, a novel AFM probe was developed by insulating tungsten micro-wires, which can measure electrical activity at the nanoscale. These probes, coated in gold, were used to image the structure of *Escherichia coli* that surface express mutants of the redox active enzyme, alcohol dehydrogenase II. Simultaneous structure–function imaging of the bacteria cells revealed improved electron transfer when mediators were placed closer to the NADH binding pocket. Second, a two–chamber system mimicking biological membranes ($\sim$5 nm thick) that enables the imaging of ion channel proteins in lipid membrane models was developed. The two chambers were separated by a 5 nm thick insulated graphene sheet deposited over a 1 μm hole. A TEM was used to drill a $\sim$20 nm pore. The substrate supports lipid membranes for measuring electrical activity. Third, AFM was used to image cell–surround communication channels (Connexin26 hemichannels) in purified membrane plaques as well as in reconstituted lipid membranes revealing channel clustering in high-resolution images. The electrical activity of these hemichannel preparations were then recorded when deposited over the nanopore supports for initial simultaneous electrical recording and imaging. Lastly, the design and development of a parallel SICM–array capable of simultaneous multi-point high-throughput nanoscale imaging was realized.

Introduction

The human body is a macro-to-nano multiscale functional assembly of organs, tissues, cells, and subcellular complexes. At each scale, the combined effects of biochemical and biophysical interactions operate to ultimately determine the overall health and well-being of humans. This thesis explores this biological frontier at the nanoscale, the length scale of fundamental building blocks, like proteins and their macromolecular complexes, including channels and receptors. The nanoscale structure and activity of channels and receptors ultimately drives living systems from embryogenesis to death. Channels and receptors operate by altering their structural conformation that regulates their activity to promote a multitude of cellular behaviors, including cell proliferation, migration, communication, and even cell death. Understanding the changes in and function of ion channel conformation and activity in its native environments in real-time is paramount to determining their role in health and disease. However, much of our understanding of the structure of ion channels is acquired in static systems, which are physiologically limited. Moreover, these static methods rarely allow correlated studies of structure and activity simultaneously. This prohibits a more detailed understanding of biological systems as the structural conformation and activity of these macromolecules are intrinsically dependent and essential to human life.

To better understand the role of ion channels in health and disease, simultaneous examination of the activity and structure of ion channels is necessary. This requires the development of novel enabling tools that can operate at the nanoscale and image samples in an active, physiologically–relevant environment. I present research and development of novel nanotechnologies for integrated and multi-modal scanning probe microscopy, a non-electromagnetic imaging technology that relies

on the interaction between a cantilever tip and the sample surface to map the surface topography. The nanotechnologies developed herein enable simultaneous imaging of nanostructure while recording the activity of enzymes and ion channels.

The objective of this thesis was as to create novel nanotechnologies for simultaneous imaging of structure and activity recording of biomacromolecular complexes by developing upon the nanoscale imaging capabilities of atomic force microscopy. Chapter 2 focuses on the design and development of an AFM conducting cantilever probe that is insulated everywhere except the tip apex that allows highly sensitive recording of electrical activity. This novel cantilever probe was utilized to image the structure of nanoporous materials. Chapter 3 focuses on the use of the conducting probe to image and record the electrical activity of bacteria designed for improved bioelectronics. In Chapter 4, AFM was utilized to image purified connexin26 hemichannels, a class of ion channel proteins, that were expresed in insect cell plasma membranes, as well as reconstituted in liposomes that were deposited as bilayers. Chapter 5 focuses on another development, a two–chamber system for simultaneous structural imaging and electrical recording of biomolecules within active membrane models. This system utilizes a graphene membrane that contains a single nanopore that supports simultaneous imaging and recording. Chapter 6 describes current progress in the use of the graphene-based nanoporous substrate for imaging and recording of connexin26 hemichannel activity. Lastly, chapter 7 describes the design and fabrication of parallel AFM-based technology for simultaneous multipoint imaging.

Chapter 1

Background

1.1 Scanning Probe Microscopy

Scanning probe microscopy (SPM) was first invented with scanning tunneling microscopy (STM) in 1981 [1]. The operation of STM is based upon the principle of quantum tunneling, which depends on the distance between a sharp conducting probe and a surface. The development of this microscope enabled imaging of nanoscale structures and molecules on a conducting surface. This principle was later expanded upon by the development of new SPMs, such as atomic force microscopy (AFM) [2], scanning ion conductance microscopy (SICM)[3], scanning electrochemical microscopy (SECM) [4], along with many more [5, 6].

1.2 Atomic Force Microscopy

1.2.1 Principles of Imaging

AFM is a high resolution SPM capable of imaging in air as well as liquid environments [7]. Unlike STM, which requires a voltage bias between the sample and imaging probe, AFM relies soley on the physical interaction between a nano–sharp tip at the end of a cantilever beam and a surface. The interaction between the tip and the surface is a combination of attractive and repulsive forces, including Van Der Waals interactions, solvation forces, capillary forces, electrostatic forces, and

Pauli repulsion. The combination of these forces that occur between the tip and the surface can be described by the Lennard–Jones potential, which summarizes the interactive force to be dependent on distance, r, as attractive forces occur at larger distances and repulsive forces at close proximity.

$$V_{LJ} = 4\epsilon \left[\left(\frac{\sigma}{r}\right)^{12} - \left(\frac{\sigma}{r}\right)^{6} \right]$$

In the equation, r is the distance between atoms and σ is the distance where the sum interaction potential is zero. ϵ is the depth of the potential well. In AFM, as the tip approaches the surface, a repulsive force occurs between the tip and the surface resulting in deflection of the cantilever. The deflection of the cantilever is governed by Hooke's law where the force, F, is proportional to the deflection, x, and the spring constant of the cantilever k.

$$F = -kx$$

The interaction force between the cantilever and the sample surface can be directly measured by monitoring the deflection of the cantilever through either optical, piezoresistive/piezoelectric, or capacitance read-out systems (Figure 1.1) [8, 9, 10].

1.2.2 Imaging Modes

AFM imaging can be performed utilizing different feedback modes that allow for control over the force applied to the surface. Briefly, the two most common modes of imaging, contact and tapping mode are explained. Contact mode operates by maintaining a constant cantilever deflection, *i.e.* a constant force, during imaging. Tapping mode or intermittent contact mode is performed by vibrating the cantilever at its resonant frequency. As the cantilever tip approaches the surface, the amplitude of the vibrations are dampened. During imaging, a constant amplitude of vibration is maintained [11]. To maintain a constant deflection or amplitude of vibration for the cantilever, a feedback system is used consisting of a piezoelectric tube that adjusts the distance between the sample and the probe while also performing raster scans across the surface (Figure 1.1).

In addition to imaging, AFM can also be used to measure the mechanical properties of a materials by nanoindentation [12, 13, 14]. A series of indentations

are performed on different locations on the material. Each indentation results in a cantilever deflection–distance curve that can be fit to different contact models depending on tip geometry and substrate thickness to determine the Young's modulus, E, of the material being probed. This feature allows for mapping the spatially dependent mechanical properties of a surface at the nanoscale.

1.2.3 Imaging Resolution and Applications

AFM, unlike other imaging technologies utilized in biological sciences, such as electron microscopy, x-ray diffraction, and x-ray crystallography, allows high resolution imaging of samples in active aqueous environments at the 1–2 nm scale. The spatial resolution of the AFM is limited by the size of a defect on the tip, which allows structures smaller than the tip radius to be observed. Unlike electromagnetic imaging techniques, the resolution of AFM is limited by the instrumentation and not the wavelength of the radiation source. Limitations of the instrumentation include the piezo-electric scanner, the cantilever deflection detection (a photodiode and laser in most commercial technologies), and the cantilever properties. In addition, the noise in the system, including mechanical vibrations, electrical (60 Hz noise and Johnson–Nyquist Noise), and thermal motion could affect the AFM performance [15]. AFM has been successfully used to image crystalline materials that are $<$1 nm in structure [16, 17]. Non–crystalline materials including single molecules have also been imaged at sub-nanometer resolution [18]. Biological materials, such as individual lipid head groups as well as protein subunit structures have been imaged using AFM [19, 20, 21, 22, 23]. However, AFM imaging of biological samples often pose a slight challenge due to the presence of fluid, temperature requirements, and mobility of the sample.

The temporal resolution of AFM is heavily dependent on the properties of the cantilever, instrument, and spatial resolution. Newly developed AFM models can capture single images in $\sim$1 s, while more traditional AFMs perform a high resolution imaging on the scale of minutes. High-speed AFM imaging requires smaller cantilevers as reducing the length of the cantilever is the only means to keep the spring constant small while increasing the resonant frequency [24, 25].

Integrated piezoelectric actuators on the cantilever can also achieve high speed imaging by circumventing the long response times of the piezotube [26].

AFM has been successfully utilized to study a broad range of solid state and biological materials. Cells and tissue have been successfully imaged in fluids mimicking physiological conditions [12, 27, 13, 28]. Membrane bound structures, such as receptors and ion channels, have been observed in active systems [29, 30, 21, 31]. Real-time conformational changes in ion channel structure, as well as mechanical properties of ion channels, have been imaged using AFM [21, 32]. Due to the open architecture of the AFM, it can be easily modified to enable simultaneous imaging of spatially localized conducting and thermal properties of materials [33, 34, 35].

1.3 Scanning Ion Conductance Microscopy

1.3.1 Principles of Imaging

The scanning ion conductance microscope (SICM), like AFM, is a type of SPM, but does not rely on any physical interaction between the imaging probe and the surface. The technique is fully non–contact and –destructive. The topography of a surface is generated by mapping localized measurements of ionic conductance. A probe is utilized with a small conducting region located at the apex of the probe tip. A counter electrode is then present in the conducting medium (Figure 1.2 A). At large distances from probe tip to sample, the bulk current is measured. However, as the probe approaches the surface, there is limited access of ions to the conducting tip region, which reduces the ionic current (Figure 1.2 B–C).

1.3.2 Imaging Modes

Imaging with SICM is performed by modulating the current. It can operate in a DC mode, where the probe scans at a constant current maintained using a feedback system that controls the distance between the probe and surface. AC mode, which is analogous to tapping mode in AFM, can also be performed by

vibrating the tip at a constant amplitude and measuring the root mean square current (i_{rms}) while maintaining a constant rms value during imaging.

1.3.3 Resolution and Applications

The resolution of SICM is limited by the diameter of the imaging electrode opening on the probe. Additionally, the electrical noise, especially the Johnson–Nyquist noise, limits the resolution. SICM has been used to successfully image the structure of pores of various sizes [36, 37, 38, 39, 40, 34].

It has been cobmined with AFM for simultaneous topography mapping with ion sensing. However, high-resolution imaging has proven to be non-trivial in practice as the non-conducting coatings often have micro-fissures allowing leakage currents to pass[41, 42, 43]. This has limited the resolution of the probes, and thus has not been successful in the study of small ion channels with nanometer-size pore diameters.

SICM has also been utilized to image biological samples due to its non-destructive nature as it can operate in non-contact modes and identify pores that are conducting [34, 44, 45]. SICM has been used effectively to non-destructively image pores within suspended lipid bilayers [36]. It has also been used in whole cell imaging for identifying single ion channels, but with limited resolution, such that the structure and conformation could not be observed [46].

1.4 Ion Channel Proteins

Ion channels are an important class of proteins that regulate cellular homeostasis by controlling the flow of ions in and out of cells. These proteins are located in the plasma membrane of cells and are barrel in shape, hence an open-ended channel through which ions flow. The activity of ion channels is regulated by different conformational states that control the flow of ions through the protein in response to a variety of stimuli, including ligand binding and changes in voltage, light, temperature, and ionic concentrations. Ion channels affect the behavior of cells and tissues, either directly or indirectly, by translating upstream signals

to downstream pathways. Abnormal channel conformations and activities play an important role in drug addiction and substance abuse mediated cell death, as well as in the pathogenic processes of several neurodegenerative disorders including Alzheimer's disease and Parkinson's diseases [29]. Additionally, an important behavior of ion channels and receptors is clustering, which has been observed in AFM studies [7, 31]. This phenomena can result in altered activity of individual ion channels due to the organization and behavior of ion channel ensembles.

1.5 Gap Junction Channels and Hemichannels

1.5.1 Structure

Classically, gap junction (GJ) channels are a subset of ion channel proteins that span the plasma membranes of apposing cells that have docked together (For a thorough review of gap junction channels [47]). The structure of the gap junction was first elucidated through x-ray diffraction studies that determined the size of the gap between the two membranes connected by a channel, which was found to be $\sim$2 nm (Figure 1.3) [48]. Each channel is a hexamer composed of subunits, termed connexins (Cx). Each subunit of a hemichannel is composed of 4 transmembrane regions resulting in two extracellular loops, one intercellular loop, and both the C– and N–termini being located intracellularly. These structures are conserved across mammalian species. Each hexamer can form a physiologically active and unique single membrane channel referred to as a hemichannel (HC) (Figure 1.4).

Cx subunits are categorized by the molecular weight of the proteins, *e.g.* the Cx weighing 26 KDa is named Cx26. The N–termini, transmembrane regions, and intracellular and exctracullular loops are largely conserved between Cx family proteins. The increased size of the proteins is reflected in the length of the C–terminal strand, which functions to bind other intracellular proteins in forming larger assemblies and performing regulatory functions. This region is less rigid making direct visualization of the cytoplasmic faces of larger connexin species more difficult with techniques like AFM [49]. The Cxs can also be classified into other broad categories based on their sequence homology. Cxs with similar sequence

homology are capable of forming heteromeric and heterotypic structures where two different sized Cx proteins form part of hexamer, or two different hexamer composed of different Cx subunits dock to form a GJ channel [50, 51, 52].

GJ channels and HCs have shown clustering behavior. In the case of GJ channels, the clustering is driven by physical the properties of the membranes and minimization of energy [53, 54]. The activity of GJ channels appears to show cooperative behavior, which is dependent on the clustering properties. Activity of gap junction channels only occurs in large clusters when coupling two cells with Cx43 [55]. The activity of the channels is focused on the central regions of the cluster, while much smaller activity occurs in the periphery. However, the mechanism for the activity is not defined.

1.5.2 Function in Health and Disease

In humans, Cx proteins are found in nearly all cell types due to their importance in cell–cell communication, and ionic and metabolic homeostasis through shared electrical and chemical signals [56, 57]. GJ channels effectively couple cells together allowing for flow of ions, metabolites, and other small molecules between two cells. They are particularly critical during embryonic development as the formation of GJs facilitates cell differentiation during development [58, 59]. GJ channels have been shown to play critical roles in cell death through the passage of apoptotic signals between damaged or diseased cells [60, 61].

The activity and regulation of Cx HCs channels remain controversial because their properties are poorly understood under physiological conditions. However, several studies show that HCs play an important functional role in many cell types [62, 63, 64]. For example, Cx43, the most ubiquitous Cx, has been shown to form functional HCs in cardiac tissues in clusters [65]. The activity of other Cx HCs have also been shown in artificial systems through dye transfer assays, for Cx26 and Cx32 [66, 67]. Cellular volume can be controlled through the opening and closing of HCs, thus could affect a broad range of cellular functions and responses [30]. HCs have been linked with release of neurotransmitters and nucleotides such as ATP [62]. Structural evidence of HC function has been gathered using AFM

imaging [65, 68, 21]. HC conformation undergoes changes in response to stimuli such as Voltage, Ca^{2+}, pH, calmodulin, and phosphorylation [69, 68, 21, 70].

HCs play a functional role in cell death due to oxidative stress-induced apoptosis, which is involved in several pathologies associated with smoking as well as neurodegenerative diseases, such as Parkinson's disease and Alzheimer's disease [71, 72, 73, 74]. It is proposed that smoking causes cells to produce metabolites that can alter the membrane potential. This can result in changes to the membrane fluidity which in turn alter the activity of the HCs [74]. Altering the opening and closing kinetics of individual HCs can disrupt ionic homeostasis resulting in abnormal cell function [30]. Increased levels, or buildup, of Ca^{2+} inside the cells can activate signaling pathways, including kinases, calmodulin, and other cellular second messengers that lead to necrotic or apoptotic cell degeneration and death [75, 76, 77].

1.5.3 Connexin26

Part of the research in this thesis focuses on Cx26, the smallest connexin expressed in humans. Its smaller size makes it more stable and less susceptible to protease activity, which allows the cytoplasmic surfaces of the protein to be imaged. The structure of the protein has also been well studied with techniques that include x-ray crystallography, electron microscopy, AFM, and x-ray diffraction [78, 79, 48, 80, 69].

While the structure is well defined in GJs, the activity and the structure of HCs is much less understood. Due to the disorder of the clusters and lack of superstructure, HCs are difficult to identify and image in native and quasi–native environments. The electrophysiology of Cx26 HCs is only partially understood. Multiple conductance states have been reported for the protein with very large ($\sim$300 pS) conductance reported for some proteins while the structural differences between these conductance states are not defined [81, 82]. The structures and modulating factors that account for the variation in the conductance state are not understood.

In addition to the unique and complicated structural and electrophysiologi-

cal properties of Cx26, they also play many important physiological roles in health and disease. Mutations in the *gjbeta2* gene, which encodes for Cx26, is a cause of neonatal non-syndromic and syndromic deafness as well as thickening of the skin in hands and feet [83, 84]. Mutations in this gene result in a loss of function in GJ channels, which appears to be due to changes in the pore structure of the protein resulting in alterred passage of metabolites and ions [83, 85, 86, 87]. Increasing our understanding of the structure and activity of Cx26 can help provide new avenues for therapeutic intervention.

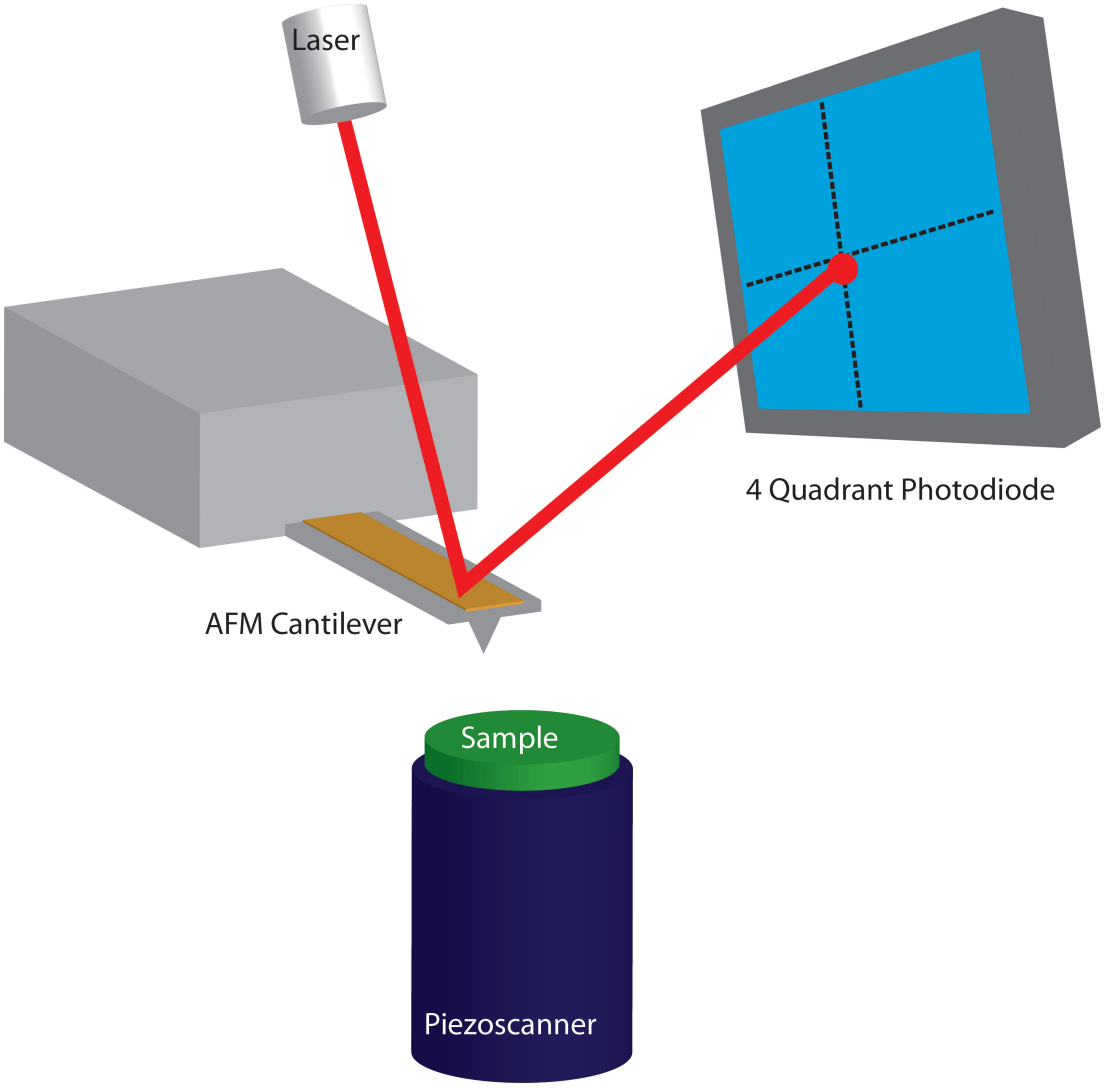

Figure 1.1: **AFM Schematic.** A laser is reflected off the end of the cantilever and is incident on a 4–quadrant photodiode. The photodiode reports the deflection of the cantilever as it interacts with the sample surface. The piezoelectric scanner moves the sample laterally in a raster scanning motion, while providing modulation of the height of the sample during imaging to maintain a constant force as determined by the cantilever deflection.

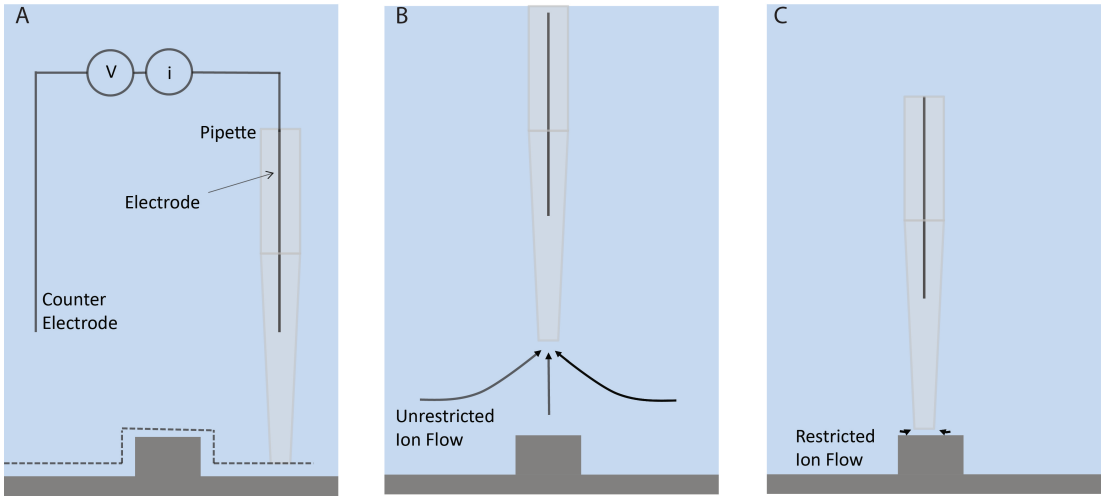

Figure 1.2: **Schematic of SICM Operation.** **(A)** The ionic currents are measured with a glass micropipette containing an Ag/AgCl electrode. An Ag/AgCl bath electrode acts as the counter electrode. The current is then measured between the two electrodes as the pipette scans across the surface. A constant current is maintained during imaging to map the surface topography. **(B)** At far distance sfrom the surface, the bulk conductance is observed by the micropipette electrode. **(C)** At close proximty to the surface, the flow of ions to the probe is restricted resulting in a reduced observed current.

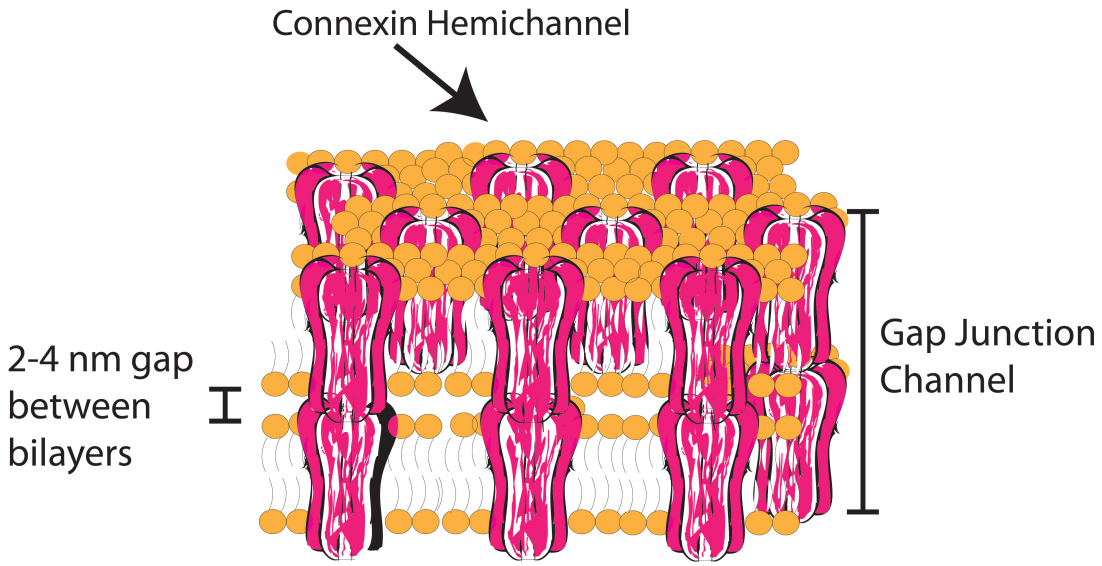

Figure 1.3: **Structure and Architecture of Gap Junction.** A gap junction consists of connexin hemichannels that have docked together in the plasma membrane of two apposing cells. The channels assemble to form a 2D crystalline structure in the lipid membrane. The separation distance of the two bilayers is maintained at ∼2 nm with pore to pore lattice spacing of the channels of ∼ 9 nm.

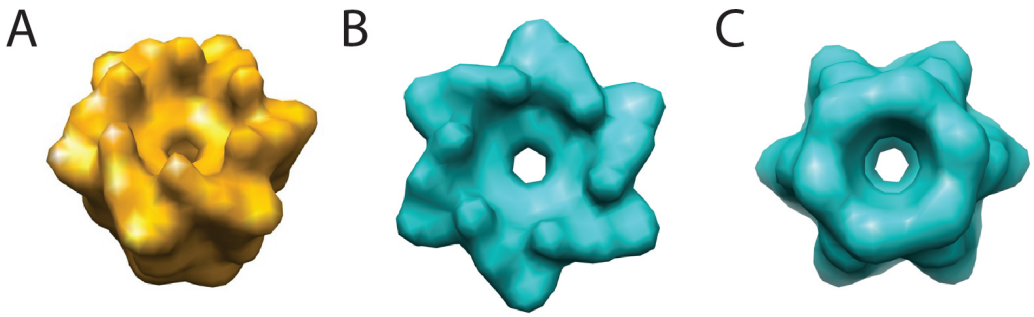

Figure 1.4: **Electron Density Projections of Cx26.** A series of density maps are shown, including a tilt view **(A)** as well as the cytoplasmic **(B)** and extracellular **(C)** faces of a hemichannel.

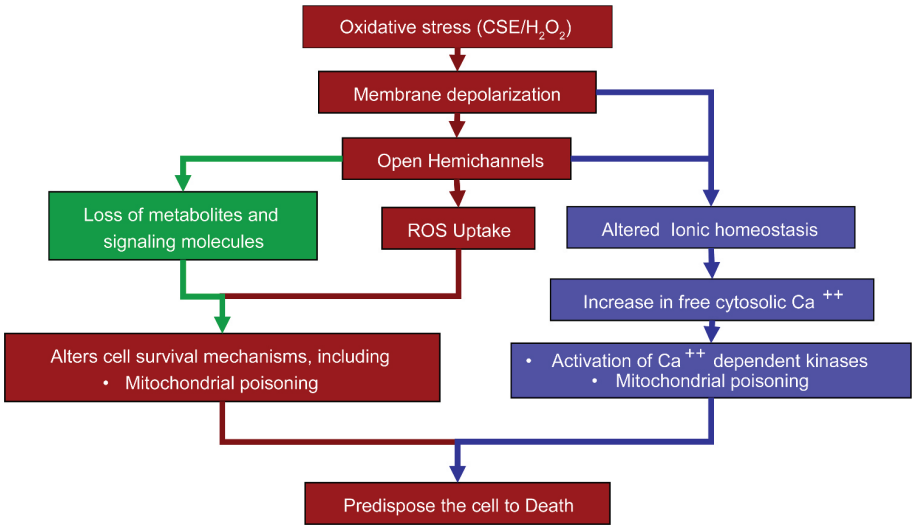

Figure 1.5: **A model of oxidative stress induced apoptosis mediated by hemichannel.** Adapted from [74]

Chapter 2

Insulated Conducting Cantilevered Nanotips and Two-Chamber Recording System for High Resolution Ion Sensing AFM

2.1 Abstract

Biological membranes contain ion channels, which are nanoscale pores allowing controlled ionic transport and mediating key biological functions underlying normal/abnormal living. Synthetic membranes with defined pores are being developed to control various processes, including filtration of pollutants, charge transport for energy storage, and separation of fluids and molecules. Although ionic transport (currents) can be measured with single channel resolution, imaging their structure and ionic currents simultaneously is difficult. Atomic force microscopy enables high resolution imaging of nanoscale structures and can be modified to measure ionic currents simultaneously. Moreover, the ionic currents can also be used to image structures. A simple method for fabricating conducting AFM cantilevers to image pore structures at high resolution is reported. Tungsten microwires with nanoscale tips are insulated except at the apex. This allows si-

multaneous imaging via cantilever deflections in normal AFM force feedback mode as well as measuring localized ionic currents. These novel probes measure ionic currents as small as picoampere while providing nanoscale spatial resolution surface topography and is suitable for measuring ionic currents and conductance of biological ion channels.

2.2 Introduction

Nanoscale transport of ionic species plays an essential role in determining the properties of biological as well as synthetic systems. In biological systems, ionic currents are primarily transported through the controlled activity of membrane pores called ion channels. Currently, ionic currents through individual channels are measured with the patch clamp technique and the 3D structures are imaged with EM, X-ray diffraction, and AFM. However, there is no technique available for simultaneous study of single channel structure and activity. Atomic force microscopy [2] (AFM) allows high resolution 3D imaging using the probe-sample interaction force as a feedback signal. Scanning ion conductance microscopy (SICM), a variant of AFM, allows high resolution microscopy utilizing ionic current between a conducting probe and a reference electrode as the feedback signal [3]. Scanning electrochemical microscopy (SECM), another variation of AFM, uses electrochemical current gradients for positioning [4]. All of these imaging modalities allow for non-contact, non-destructive structural imaging and measurement of the localized currents in fluid, a necessity for studying native biological systems, including ion channels and receptors [36, 88, 89, 45, 44, 90].

SICM and SECM usually do not have the force feedback control of an AFM. In order to image the surface topography of, and the currents through, an ion channel, SICM was originally combined with AFM to study porous membrane topography with force feedback modes of AFM, while simultaneously measuring the ionic current passing through the micro-porous membrane [34, 91]. This approach was further expanded for the study of the transport of electrochemically active species through pores while measuring the membrane structure [43, 40, 38]. In this com-

bined AFM-SICM, the probes utilized were created from glass pipettes that allowed localized ionic current measurements. However, the size of the pipette-tip was too large (>30 nm) to provide single channel resolution. For high resolution ionic current measurement and 3D imaging, the cantilever probes require a nanoscale conducting tip apex while the remainder of the probe is fully insulated from ions, such as in insulated wires [43, 41], and microfabricated probes [40, 92, 93]. Wire cantilevers offer the benefit of simple fabrication compared to microfabricated or glass pipette AFM cantilevers. Tungsten wires have been utilized in extracellular as well as intracellular neural recording and STM imaging due to their strength and electrochemical properties that allow for fine etching of the tip [94, 95]. Significantly, tungsten wire electrodes insulated with non-conducting coating except for 3–5 micrometer of the conducting tip, called Solid-Conductor Intracellular NanoElectrodes (SCINEs), have been used to record intracellular neuronal action potential (AP) as well as subthreshold currents with 10 kHz temporal resolution [96]. However, the large conducting region of the wire electrodes reduces its electrical current sensitivity - currently available wire electrodes measure currents too large for recording single ion channel current and conductance, which is usually in picoamperes (pA) for biologically relevant potential differences.

Here, we present a simplified method for fabrication of tungsten wire AFM probes capable of high resolution imaging of the structure of, and very low (pA) ionic currents through pores. These tungsten probes were coated with non-conducting materials except for a nanoscale area on probe apex in order to record small ionic currents flowing through the pores. In addition, we also designed a two chamber electrical recording and molecular transport system for imaging currents passing through micro– and nano–porous membranes. Topography of 20 nm pores was successfully imaged while simultaneously measuring localized pA currents using this system. This approach allows for probes that can be integrated with any AFM system for high resolution structure–activity imaging of biomolecules.

2.3 Methods

Tungsten wires coated in Epoxylite with 40 μm shafts etched over 5 mm were purchased from FHC (Bowdoin, ME). All experiments were performed in Dubecco's phosphate buffered saline obtained from Cellgro (Manassas, VA).

2.3.1 Probe Fabrication

Tungsten wires coated in Epoxylite were prepared and attached to a custom fabricated support chip with inert, non-water soluble Two Ton Epoxy (Devcon, Danvers, MA). The preinsulation of the wires along with the epoxy prevent currents from leaking from the wire to the steel support chip (2 mm $\times$ 1 mm $\times$ 2 mm) (Figure 1A). The wires were attached such that the sharp end of the wire overhung the edge of the support chip by 2.5 mm. After drying overnight, the wires were bent with tweezers to create a tip for AFM imaging with a tip length of 0.5 mm creating a cantilever of 2 mm. The cantilevers were then reinsulated through three coatings with Clearclad electro-deposition paint (Clearclad Coating Inc, Harvey, Il). Each coating was performed with 30 s of deposition at 10 V followed by 20 min of baking at 160 °C with the tip pointing upward to prevent insulating the apex. Mirrors for laser detection in AFM were fabricated by sputtering gold onto a silicon substrate with a DC magnetron sputter to a thickness of 200 nm. Gold was then attached to the bend of the cantilever with a single drop of Two Ton Epoxy.

2.3.2 Two–chamber AFM Setup

A two–chamber AFM setup was designed and implemented for measuring electrical currents through porous membranes. The two-chamber system consists of a bottom cup constructed from polycarbonate (Lexan) and a top cup (also polycarbonate) with a hole for ions to pass between the bottom cup to the top cup. A silver wire, electroplated with 1 M KCl at 1 V for 5 min, functioned as the Ag/AgCl reference electrode that was inserted into two-chamber AFM through a small hole in the bottom cup. Anodic aluminum oxide (AAO) membranes (d_{pore}

= 20 nm) (Synkera, Longmont, CO) and track-etched polycarbonate filters (d_{pore} = 0.8 μm) (Whatman, UK) were used in imaging experiments. AAO membranes were fixed with vacuum grease to a silicon substrate with a 200 μm square pore (App Nano, CA). The silicon substrate with the membrane was attached with vacuum grease over the hole connecting the two–chambers and PBS was added above and below the membrane.

2.3.3 AFM Imaging

A multimode AFM equipped with a Nanoscope IVa controller and a fluid cell (all from Bruker, Santa Barbara, CA) was used to image the AAO membrane in tapping mode. The bath electrode and the tip were connected to a patch clamp amplifier (Dagan, Minneapolis, MN) for simultaneous recording of ionic currents passing through the membrane. The currents were passed into the AFM controller for plotting of the data collected in current recording. Slow scan rates of 0.1–1 Hz along with a 20 Hz lowpass filter were used in all imaging to reduce noise. All electrical recording was performed in a homemade Faraday cage to eliminate noise. Images were processed following imaging using Nanoscope Analysis Version 1.40 (Bruker, Santa Barbara, CA). All images were flattened and lowpass filtered gaussian filter of 10 pixels in the horizontal and vertical axis.

2.3.4 I-V Curve Recording

Voltages were ramped between +/– 200 mV at varying rates using the Nanoscope Iva controller and patch clamp amplifier. An AAO membrane was in place between the tip and the counter electrode. The tungsten probe was withdrawn from the surface to prevent reduction of the current. The current was recorded using the setup previously described in the AFM imaging. For electrochemical experiments, 0.1 M $Fe(CN)_6{}^{4-}$ was used as the redox active species in 0.1 M phosphate buffer at pH 6.9. Voltammograms were ramped at rates of 0.05 V/s between +/– 500 mV against an Ag/AgCl reference/counter electrode utilizing the same setup as the PBS results.

2.3.5 SEM Imaging

Imaging of AAO membranes and tungsten proves was performed on an ultrahigh resolution SEM (FEI, Hillsboro, OR). The membranes were sputter coated in a thin layer (1–2 nm) of chromium to make them conducting for imaging.

2.4 Results

2.4.1 Cantilever Fabrication and Device Setup

Etched sharp tungsten wires (15 cm length) coated in epoxylite were attached to custom steel chips (1.6 mm $\times$ 2 mm) such that 2-3 mm of the wire, the sharpened end, extended off the front edge of the chip. The blunt end of the wire was used to form an electrical connection to relay feedback signal to the AFM. The sharp end of the wire was bent at 75° such that the tip pointed downward. The wires were subsequently further insulated in electrophoretic paint to fill in gaps in the insulation while maintaining the exposed tip apex (Figure 2.1 C). Gold mirrors were fixed to the end of the cantilever (as described in methods) to allow for optical detection of cantilever deflection in AFM imaging (Figure 2.1 A). A custom built two chamber AFM setup was configured for imaging ionic currents across a porous aluminum oxide membrane (Figure 2.1 A,B) where the tungsten cantilever served as a working electrode in the top cup while a Ag/AgCl counter electrode was placed in the bottom cup. Ionic currents between the top and bottom chambers were imaged through membranes placed over a single hole connecting the two chambers. The tungsten wire probe was used with the fluid cell cantilever holder of our AFM, with the blunt end of the tungsten wire exposed and connected to a patch clamp amplifier to pass the currents to the AFM. Testing of the cantilevers found resonance frequencies between 3–7 kHz in fluid.

2.4.2 Principle of Operation

Principle of AFM force-feedback mode imaging is well described and relies simply on using the cantilever deflection (due to force-field interaction between

the tungsten wire probe and sample) for controlling/measuring the probe-sample distance as the cantilever wire probe raster scans over the sample. For measuring the ionic current for feedback (SICM, SECM modes), the system operates by limiting the ionic currents that are able to access the exposed tip of the probe as the probe approaches the surface [3, 4, 89]. The measured current is determined by the exposed area of the probe when at far distances from the surface. Small electrode areas lead to small currents (pA range). For imaging of currents through pores (Figure 2.1 C), the currents passing through the pore will be defined by the geometry of the pore and the thickness of the membrane. However, when the area of the working electrode (i.e. the probe) is much smaller than the pore, the measured ionic currents will be dominated by the exposed probe area as the current density through the probe will be much higher. The current observed over the pore will remain approximately the same for the entire area of the probe whether it is in the center of the probe or the periphery (Figure 2.1 C). This is true for large pores (>1 μm) and nanopores where the measured currents are small due to the electrode area being significantly less than the pore area.

2.4.3 Probe Characterization

I–V curves of fully-coated wire cantilevers were performed following wire mounting and reinsulation to characterize the quality of the probes. These measurements were performed when the probe was withdrawn to distances far above the surface (>100 μm) to prevent inhibited ion transport currents seen with SICM probes [3]. Currents were measured as the voltage was ramped at different rates across a 400 mV range. The measured ionic currents in phosphate buffered saline (PBS) were in the pA range indicating that only a small portion of the probe was not insulated (Figure 2.2 A). Hysteresis in the curves was observed at greater voltage scanning rates. This is indicative of capacitance from incomplete sealing of the metal [42].

I–V curves were also performed in the presence of the electrochemically active specie ferrocyanide ($Fe(CN)_6^{4-}$). These voltage ramps were performed in a two-electrode setup to provide an estimate of the exposed area of the probe. I–V

curves performed over a 1 V range (Figure 2.2 B) show characteristic oxidation peaks. The area of the probes was estimated based on the steady-state currents observed using [97]:

$$i_{lim} = 2\pi nFDC^* r_{app}$$

In this equation, i_{lim} is the observed steady-state oxidative/reductive current. n is the number of electrons transferred per a redox event. F is the Faraday constant. C^* is the bulk concentration of the active species, which was 100 mM. D is the diffusion coefficient (6.7×10^{-6} cm^2/s). Measuring the steady state current allows for approximation of effective radius (r_{app}). From our measurements we found active radii ranging from 5–10 nm. This value likely overestimates the radii as it applies to the entire probe including any leakage not near the tip apex. It also includes currents generated from activity of tungsten.

Scanning electron microscopy (SEM) images of these probes used in the electrochemical measurements show features at the end of the tip in the nanoscale that are capable of obtaining high resolution images of the surface (Figure 2.2 C). The gaps in the insulation utilized for electrical recording here, are not visible due their small size and the presence of a chromium coating utilized to image the probes in the SEM.

Ionic currents showed a dependence on the distance of the exposed cantilever probe tip from the surface. As the probe approaches the surface, the current begins to decrease due to reduced ionic access to the probe. This decrease occurs prior to deflection of the probe due to interaction with a mica surface (Figure 2.2 D). Approach curves onto a track-etched polycarbonate membranes in non-porous regions show a similar decrease as those observed on the mica surface when utilizing a different probe with a different geometry. The retraction of the probe from the surface resulted in a recovery of the ionic current (Figure 2.2 E). Observed hysteresis in these curves could be due to tip adhesion to the surface, as the retraction currents are reduced compared to the approach currents for the same height.

2.4.4 Structure and Ionic Currrent Imaging of Micro- and Nano-pores

Imaging of ionic currents through pores with simultaneous surface topography imaging was performed on synthetic porous membranes. Track-etched polycarbonate membranes with 0.8 μm pores were mounted in the two chamber AFM system. The tungsten wire cantilever was utilized to image the surface topography while simultaneously measuring the ionic current (Figure 2.3 A–C). Ionic currents imaged over the pore increased by $\sim$3 pA compared to when the probe was positioned over regions without pores. High correlation is observed between the pore locations in both modes of operation.

AFM imaging of the anodic aluminum oxide (AAO) membrane demonstrates pores on the order of 18 nm in height mode (Figure 2.4). This is consistent with the expected pore diameters for the membrane. Current mode imaging, taken simultaneously with topographic imaging, confirms the presence of multiple pores in the membrane. The location and size of the pores are in the same location and of similar diameter in both concurrent imaging modes, confirming accurate reading. Scanning electron microscopy (SEM) images of the AAO membrane demonstrated similar structures to those imaged with the AFM (Figure 2.5).

Scanning ion conductance microscopy (SICM) was also performed with the tungsten wire cantilevers. This imaging mode used the ionic current as the feedback signal for z positioning of the probe since the observed current is dependent on the probe distance from the surface. Imaging of the AAO membranes in SICM mode resulted in structures similar to those observed with AFM and SEM (Figure 2.6). However, greater noise in this mode resulted in low resolution quality compared to the image using force feedback with ionic currents as the carry-along signal.

2.5 Discussion

Imaging of ionic currents through micro- and nano-porous samples requires a system that allows for highly localized current measurements while limiting leakage current bias. The use of electrophoretic paints for insulating sharp wires have

been demonstrated to be an effective means to limit the conductive surface to the nanoscale [43, 40, 98] which is the technique we pursued. Two insulating coatings were used in the fabrication in this paper to 1) reduce the presence of cracks in the insulation and 2) allow the coating to get closer to the probe apex. Ionic currents measured by this probe were restricted to the pA ranges. This is indicative of successful insulation of the probes.

Imaging of the ionic currents on the AAO membrane show some overlap in the signal from multiple pores (Figure 2.4). This occurs due to the close proximity of the pores to one another, as seen in SEM and AFM, and the size of the probe (Figure 2.4 and 2.5). The ionic currents measured in this study are significantly smaller than the ionic currents passing through the porous membranes. For nanoscale pores, the currents would be in the nA to μA range. However, the observed currents are in the pA range. This occurs due to the restricted small electrode area for the ions to access (Figure 2.1 C).

Extensive work has been performed in improving SICM probe resolutions to the nanoscale [36, 45, 90, 37]. However, combined SICM-AFM probes have been more limited. The tungsten probe presented here allows for simple fabrication of conducting probes such that only the tip apex remains conducting while being suitable for ion sensing AFM. The use of wire based cantilever probes for SPM has been previously reported for larger pores sizes of 600 nm [40]. However, the tungsten cantilevered probes reported here improve upon the resolutions of these previous SICM/SECM-AFM probes [34, 38, 92] while reducing the complexity of fabrication.

Chapter 2, in full, is a reprint of the material *Meckes B, Arce F T, Connelly L S, Lal R. Insulated Conducting Cantilevered Nanotips and Two-Chamber Recording System for High Resolution Ion Sensing AFM. Scientific Reports. 2014; 4: 4454.* The dissertation author was the primary author.

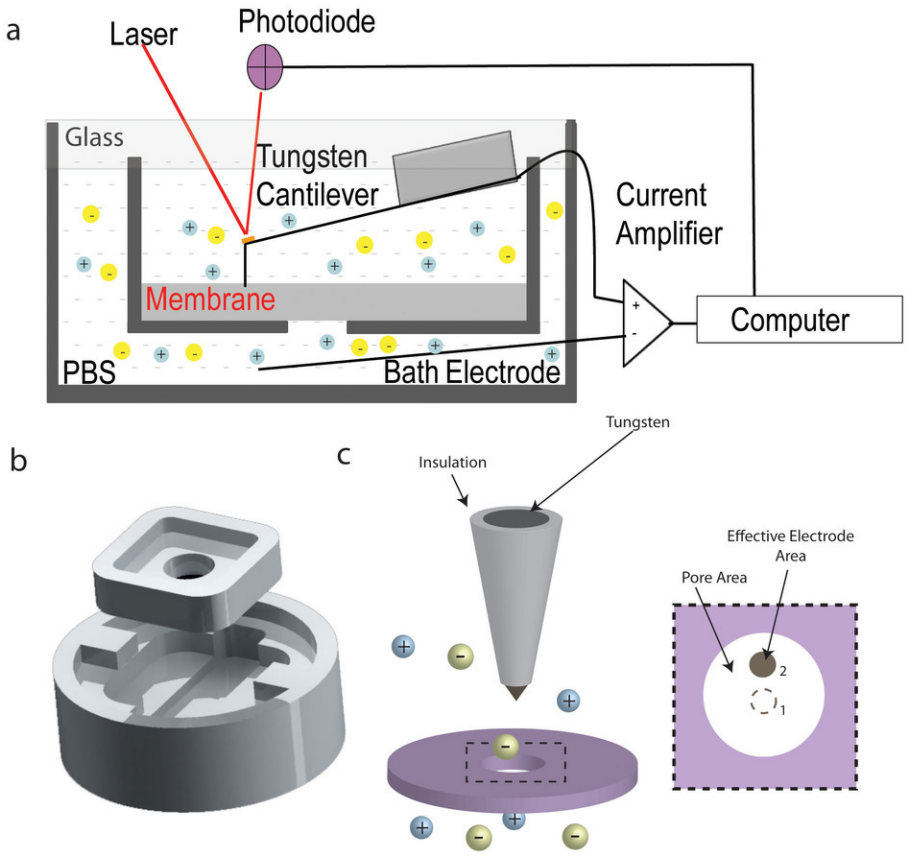

Figure 2.1: **Schematic of the device setup and operation.** **(A)** The ionic currents are measured with a conducting tungsten cantilever probe. A Ag/AgCl bath electrode acts as the counter electrode that is electrically separated from the tungsten probe by a membrane. The current measured between the two electrodes is passed through a current amplifier to the AFM controller. **(B)** The two chamber AFM system for imaging ionic currents passing through membranes. **(C)** Schematic of the probe over a pore. The effective electrode area determines the probe conduction behavior when the exposed area near the tip apex is smaller than the pore diameter.

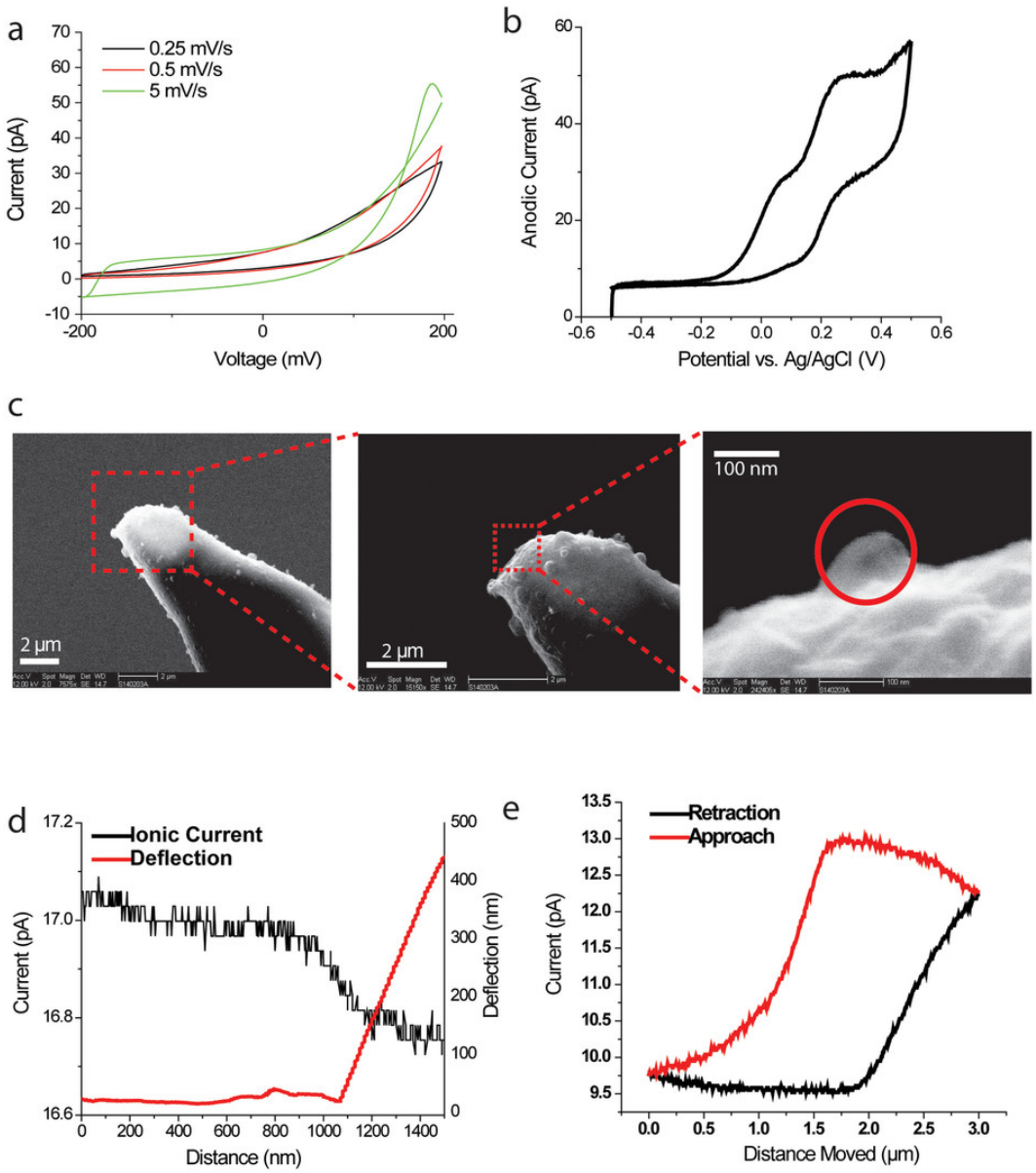

Figure 2.2: **Characterization of tungsten probes.** **(A)** I–V curves a tungsten wire cantilevers in PBS. The voltages were ramped between +/– 200 mV at rates of 0.25 mV/s, 0.5 mV/s, and 5 mV/s. **(B)** Cyclic voltammograms of the probe in the presence of 0.1 M $Fe(CN)_6^{4-}$. An oxidation peak is observed near 0.2 V, not present in PBS. **(C)** SEM images of a tungsten cantilever probe at multiple scales. **(D)** Approach curve of tungsten electrode engaging a mica surface with both cantilever deflection and ionic current plotted. **(E)** Approach and retraction curves of a tungsten probe as it approaches a track etched polycarbonate membrane.

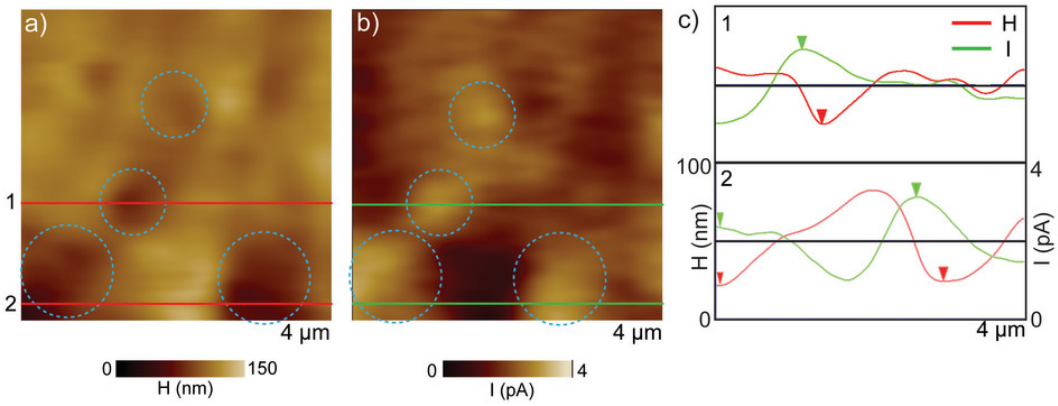

Figure 2.3: **AFM Images of micropore topography and ionic current.** Simultaneous height **(A)** and ionic current **(B)** AFM images of a track etched polycarbonate membrane with nominal pore diameters of 0.8 μm. Lighter colors indicate higher currents. As shown in the images and the two cross sections across three pores **(C)**, high correlation is seen between the height and currents at the locations of the three pores indicated by triangles. Red lines are used for height (H) and green for current (I). The scales are the same for both cross sections.

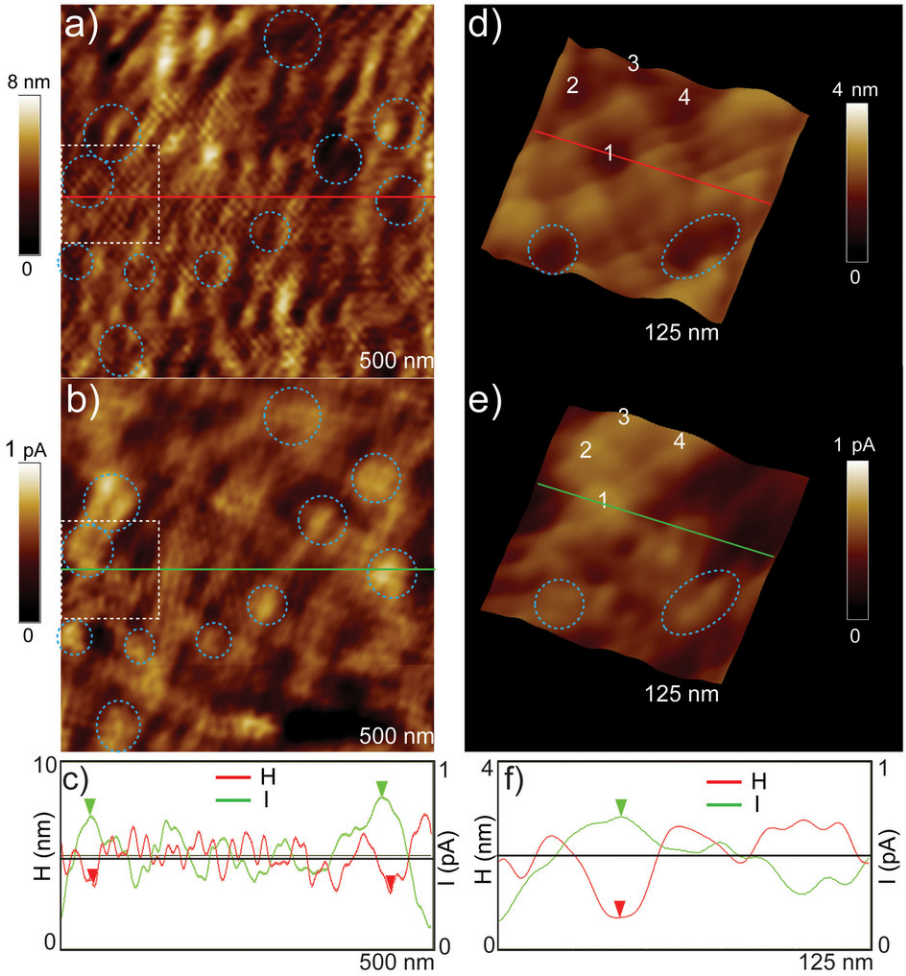

Figure 2.4: **AFM Images of Nanopore Topography and Ion Current.** Simultaneous **(A)** Height and **(B)** current images show similar geometry to SEM images and have good correlation with each other. **(C)** A cross section of the ionic current acquired simultaneously with the height image. Dashed circles indicate pores observed in both images. **(D–F)** similar images and line profiles for the 125×125 nm^2 region indicated by dashed squares in **(A–B)** show that individual pores (marked with numbers 1–4 and dashed circles) are resolved in the height and current images. Red lines are used for height (H) and green for current (I). Images were Fourier filtered to remove noise.

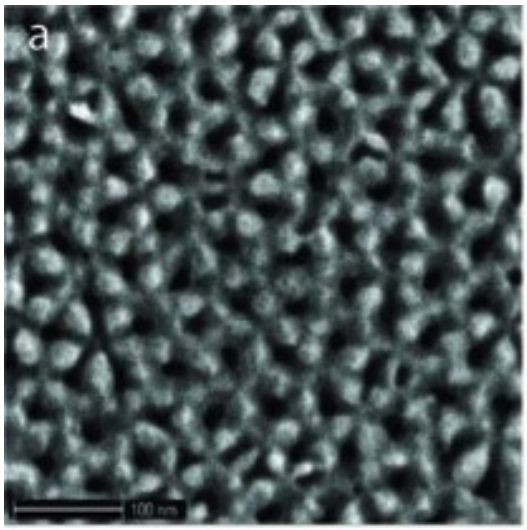

Figure 2.5: **SEM image of an AAO membrane with 18 nm pore diameters.**

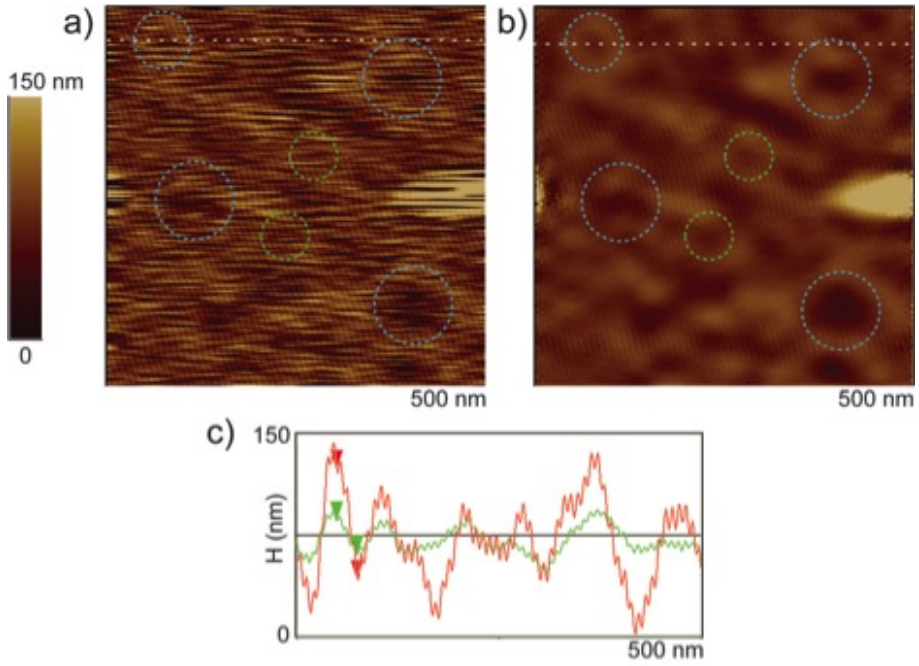

Figure 2.6: **SICM mode image of an AAO membrane with nominal pore diameters of 20 nm using the ionic conductance for the probe height feedback.** **(A)** and **(B)** show images with different degrees of Fourier filtering. Even though large depths are measured in **(A)**, noise contributes significantly to the depth measured. **(C)** Height profile across one of the pores. As noise is removed, the pore depths approach the smaller depths measured in the AFM images shown in figure 4. Blue dashed circles indicate pores recognized clearly in both images. The green circles indicate structures which appear to be pores after filtering, but are not well-defined in **(A)**.

Chapter 3

Measuring Localized Redox Enzyme Electron Transfer with Conducting Wire Cantilevers

3.1 Abstract

Bacterial systems are being extensively studied and modified for energy, sensors, and industrial chemistry; yet, their molecular scale structure and activity are poorly understood. Designing efficient bioengineered bacteria requires cellular understanding of enzyme expression and activity. An atomic force microscope (AFM) was modified to detect and analyze the activity of redox active enzymes expressed on the surface of E. coli. An insulated gold-coated metal microwire with only the tip conducting was used as an AFM cantilever and a working electrode in a three–electrode electrochemical cell. Bacteria were engineered such that alcohol dehydrogenase II (ADHII) was surface displayed. A quinone, an electron transfer mediator, was covalently attached site specifically to the displayed ADHII. The AFM probe was used to lift a single bacterium off the surface for electrochemical analysis in a redox-free buffer. An electrochemical comparison between two quinone containing mutants with different distances from the NAD^+ binding site in alcohol dehydrogenase II was performed. Electron transfer in redox active proteins

showed increased efficiency when mediators are present closer to the NAD^+ binding site. This study suggests that an integrated conducting AFM used for single cell electrochemical analysis would allow detailed understanding of enzyme electron transfer processes to electrodes, the processes integral to creating efficiently engineered biosensors and biofuel cells.

3.2 Introduction

Understanding the electrical and chemical activity of individual cells will play a critical role in designing and developing future bioelectronics. High-resolution functional imaging is critical for understanding molecular scale activity and its underlying structural substrate. Atomic force microscopy (AFM) allows for high resolution imaging as well as simultaneous study of various physicochemical properties [2, 3, 4, 31, 34, 99]. Coupling of AFM and electrochemical analysis (EC) has been developed, although mostly for measuring the conductance in nonliving systems [100, 101]. It has been used to study diffusional species in solution with the imaged substrate surface acting as a working electrode for self-assembled monolayers on the surface [102] and the switch of redox states of a single metallo-protein bound to the surface [103, 104]. Recently, EC-AFM has been used for potential dependent adsorption/desorption of inorganic molecules [105]. However, selective removal of a single cell from a surface and subsequent electrochemical study of a specific redox protein expressed by the cells has not been reported.

Nicotineamide adenine dinucleotide (NADH) serves as a cofactor in over 300 redox enzymes, including alcohol dehydrogenase II (ADHII), the enzyme of interest in the bacterial system studied here. These dehydrogenases are being used in catalytic electrochemical oxidation processes in biosensors and in biofuel cells among other bioelectronic applications. The large overpotentials that are needed to oxidize NADH to NAD^+ render it useless for these purposes [106]. To overcome overpotentials, it was suggested to modify the surface of an electrode with quinones [107]. In this study and others, the possibility of covalent incorporation of electron-transfer mediating groups attached to the surface of the electrode was

suggested and studied. Other studies have demonstrated a remarkable decrease in overpotentials needed for NADH oxidation [108, 109].

We have previously developed a novel approach for bacterial redox enzyme modification and expression [110]. We have shown that these engineered bacteria can be successfully used in a biofuel cell and can even be used as active and viable biocatalysts for more than a week with relatively high power outputs. Briefly, E. coli was modified to display the redox enzyme, ADHII, on the surface using an autodisplay system [111]. The unnatural amino acid para-azido-l-phenylalanine (Az) was incorporated into a specific site of the enzyme using the stop codon suppression strategy [112]. When attached to Az, a quinone facilitates electron transfer between the enzyme and an electrode. In order to attach the bacteria carrying the surface displayed enzyme to a surface, a quinone linker **(1)** containing an alkyne and a thiol moiety on opposite ends was synthesized and attached to the dehydrogenase site specifically through a copper(I)-catalyzed azide–alkyne cycloaddition reaction [113]. Using this approach, we were able to covalently link bacteria to gold-coated surfaces. The orientation of the redox enzyme on the surface of the electrode can be controlled, and the distances for electron transfer between the enzyme active site and the electrode surface are predetermined.

In order to enable the characterization of the bacterial surface and its electrochemical properties, we have coupled the imaging abilities of atomic force microscopy (AFM) with those of electrochemical techniques. The AFM cantilever, coated in gold and insulated such that the tip is the conducting surface, served both as an imaging probe and as a working electrode in the electrochemical cell. The bacteria express ADHII with a linker **1** attached site specifically to their surface. An exposed thiol on the linker **1** facilitates the gold AFM cantilever attachment to the bacteria. This novel approach was created to determine: (1) What will happen if a quinone is covalently attached site specifically into a predetermined site, in a hydrogenase that uses NAD^+ as its cofactor. (2) How it will affect its oxidation overpotentials. (3) How the distance of the NAD^+ from the electrode surface will affect its electron transfer (ET) properties. Utilizing our modified AFM probes, we successfully imaged and measured the electrochemical activity of a single bacterium

with different ADHII mutants. Through these studies, we demonstrated improved activity in ADHII mutants with electron transfer mediators close to the NAD^+ binding site. This approach for studying enzymes can be applied and adapted to study the electrochemistry of other redox enzymes and electrogenic bacteria as well as synthetic electrochemically active nano/microparticles.

3.3 Methods

3.3.1 Chemicals and Reagents

All chemical reagents were purchased from Sigma-Aldrich (Rehovot, Israel) or Acros (Geel, Belgium) and used without further purification. The unnatural amino acid AzPhe was purchased from Bachem (Bubendorf, Switzerland). PCR was performed with the Kapa HiFi PCR Kit (Kapa Biosystems, Woburn, MA). Plasmid DNA isolation was performed with the QIAprep spin miniprep kit (QIAGEN, Hilden, Germany). Oligonucleotides were supplied by Sigma (Rehovot, Israel) and by IDT (Jerusalem, Israel).

3.3.2 Modified Bacteria Preparations

A full description of modified bacteria can be found in our previous report [110]. Briefly, site-directed mutagenesis on pJM7-ADH (plasmid encoding for Autodisplay of ADHII) was performed using a QuikChange II kit according to the manufacturer's instructions, using the primers for PCR, containing mutation sites for ADHIIV66Az or for ADHIID314Az. (A full list of primers is depicted in ref [110])

3.3.3 Surface Modifications

Glass microscope slides (Marienfeld, Lauda-Königshofen, Germany) were cleaned using the UVOCS ozone cleaning system (Lansdale, PA) for 10 min. A 5 nm chromium adhesion layer and a 20 nm gold layer were deposited using K575X

sputter coater (Quorum Technologies, Kent, UK). Bacteria were attached to the surface as described in ref [110].

3.3.4 Preparation of AFM Probe/Working Electrode

The AFM probe was created utilizing a sharp tungsten wire coated in epoxylite with a shaft diameter of 40 μm (FHC, Bowdoin, ME). Gold was sputtered onto the wire to a thickness of 25–50 nm. The wire was reinsulated through 3 coatings with ClearClad HSR (Chicago, IL) following the manufacturer's instructions. The wire was attached to a custom cantilever holding chip, and a gold mirror was affixed for laser detection with Two-Ton Epoxy (Devcon, Danvers, MA).

3.3.5 AFM Sequence of Operations and Imaging

Images and adhesion measurements were taken with a Multimode AFM with a Nanoscope V controller (Bruker, Santa Barbara, CA). Images were taken with a custom tungsten probe ($k \simeq$10 N/m) in contact mode with the force minimized to reduce damage to the bacteria. Bacteria were imaged at scan rates of 2–5 Hz. The probe was then zoomed onto a single bacteria, and the scan area was set to 0 μm^2. After localization of bacteria, force images were taken with ramp sizes of 500 nm. The probe remained in contact with the surface with a constant force when initial electrochemical measurements were taken.

3.3.6 Electrochemical Measurements

An EMstat^{3+} potentiostat was used (PalmSens BV, The Netherlands) for cyclic voltammetric measurements. A three-electrode electrochemical cell was assembled where the working electrode was a tungsten AFM tip coated with gold (Figure 3.10). The reference electrode was Ag/AgCl wire prepared by electroplating in 1 M KCl for 30 min at 1 V. The wire was prepared as a reference electrode daily prior to all experiments to reduce electrical drift; a reference solution of 1:1 ratio 10 mM $Fe(CN)_6{}^{3-/4-}$ in TRIS buffer was made and used daily to verify the reference potential of the reference electrode (Figure **??**). The reference electrode

was present with a large junction to allow a large access area. The counter electrode was a platinum wire. All electrodes were assembled in a liquid AFM cell (Bruker, Santa Barbara, CA) equipped with several ports for electrodes. The working volume was ∼100 μL. Electrolyte solution was 0.1 M Tris buffer, pH = 8.0. Measurements were conducted in the range of –0.8 to 0.1 V vs Ag/AgCl with varying scan rates. Electrode surface area determinations were conducted using a 10 mM solution of $Fe(CN)_6^{3-/4-}$ (1:1 ratio mixed solution), in a range of (–0.1) to (+0.6) V vs Ag/AgCl. Cathodic peaks determination was done by drawing a baseline between forward and reverse curves and measuring the region with the largest current from the baseline for each scan rate. The potential at the largest current point was determined as the cathodic potential, and the current at that point was determined as the cathodic peak current.

3.4 Results

3.4.1 Electrochemical Cell Configuration

The electrochemical cell was configured with the gold coated tungsten microwire acting as a cantilever tip while serving as the working electrode in the three-electrode electrochemical cell. The probe was insulated to limit the active electrode area to the tip of the probe (described in the Experimental Section). Platinum and Ag/AgCl wires acted as the counter and reference electrodes, respectively (Figure 3.1). The Ag/AgCl wire was placed directly in contact with the fluid creating a large access junction to prevent junction clogging as would occur in a small junction glass electrode.

3.4.2 Imaging of Bacteria

Three different mutants of alcohol dehydrogenase II (ADHII) were displayed on the surface of E. coli. Each mutant was generated with varying distances from the NAD^+ binding pocket; mutants V66Az and P182Az were generated with approximate distances of ∼5 Å each from the binding pocket and mutant D314Az

with a distance of ∼42 Å from the binding pocket (Figure 3.5, Table 3.1). In this study, we have excluded mutant P182Az as V66Az is a similar distance (∼5 Å) from the NAD^+ binding pocket. The modified bacteria were covalently attached to gold-sputtered glass slides via linker **1**. Slides with attached bacteria were imaged with the wire AFM cantilever. Figure 3.2 A shows an image of multiple bacteria on the surface of a slide. A bacterium was localized with the AFM for subsequent electrochemical analysis. Figure 3.2 B–D shows individual bacterium of different mutants, V66Az, D314Az, and wild type bacteria (WT), selected for electrochemical measurements. The presence of bacteria on the gold substrates was confirmed with light microscopy imaging (3.2 E).

3.4.3 Picking up a Single Bacterium

A bacterium was picked up by the conducting AFM probe through the following steps as summarized in Figure 3.10. After localization of a bacterium, the gold-coated conducting AFM probe was allowed to remain in controlled contact with the bacterium surface without imaging to facilitate gold–thiol bond formation between the linker **1** site specifically attached to ADHII and the probe for ∼5 min (Figure 3.10 B). The chemical structure of the thiol containing linker **1** is shown in the inset of Figure 3.10. The tip was then disengaged from the surface (Figure 3.10 C). Successful attachment of the bacterium to the tip inhibited reimaging of the surface. This was further confirmed through observed changes in cyclic voltammograms. The activity of the probe before imaging the bacteria was recorded (Figure 3.6, background). During the selection of a single bacterium, electrochemical measurements were conducted to check whether electrochemical activity could be detected (Figure 3.6, surface mode). This served as our first indication of a successful transfer of a bacterium from the surface to the tip. Upon selecting and attaching a bacterium to the AFM tip, we commenced with our electrochemical analysis of electron transfer (ET) processes (Figure 3.6, withdrawn mode). Coupling both the AFM imaging abilities with the electrochemical signals demonstrated that we have collected a redox active bacterium off the surface. However, this did not exclude the possibility that only part of the bacteria was

removed.

In order to ascertain gold–thiol bond formation between the enzymes on the bacterial surface and the cantilevered tip, we measured the adhesion forces while engaging a single bacterium. Figure 3.7 shows examples of the measured adhesion using the force mode for mutants D314Az and V66Az. As a control measurement, adhesion forces were also measured for a bare Au surface. In addition, only upon observing these adhesion forces could electrochemical activity be detected on the surface of the AFM tip (serving as our working electrode). Combining all this evidence together with the actual size of our working electrode (ca. 100 μm^2) indicates that the probe and system is capable of picking up a single bacterium or a fragment. Control experiments conducted with surfaces modified with WT non-modified bacteria that were nonspecifically bound to the surface as well as surface modified bacteria displaying WT-ADHII did not yield any visible electrochemical signals. This occurred neither when the probe engaged the bacteria on the surface nor when the probe was subsequently withdrawn.

3.4.4 Determination of Electrode Size and Surface Coverage

Due to the fabrication processes and customization of the working electrodes for AFM, there existed heterogeneity in electrode surface areas. In order to avoid large differences between the measured surfaces, we have used a 10 mM solution of $Fe(CN)_6^{3-/4-}$ for an initial determination of our actual active surface, basing our calculations on the Randles-Sevcik equation for diffusional species. Thus, tips that have shown large redox currents indicating surface areas larger than 100 μm^2 were excluded.

Figure 3.8 shows the cyclic voltammograms collected using a mutant V66Az modified AFM tip (lavender colored line), a mutant D314Az modified tip (rose colored line), and a background measurement of the unmodified working electrode (lime green colored line) collected at a scan rate of 0.05 $V \cdot s^{-1}$. When studying the electrochemical properties of linker **1**, based on eq 1, plotted I_p values against scan rates determined a surface coverage of $\Gamma = 2.3 \times 10^{-10}$ $mol \cdot cm^{-2}$. However, surface coverage values calculated for the surface modified bacteria containing linker **1**

bound to the surface of the electrode yielded values of $\Gamma_\circ = 8.0 \times 10^{-11}$ mol·cm^{-2} and $\Gamma_R = 1.0 \times 10^{-11}$ mol·cm^{-12} for mutant V66Az, oxidized and reduced forms, respectively, whereas the values of surface coverage for mutant D314Az were $\Gamma_\circ = 2.7 \times 10^{-11}$ mol·cm^{-2} and $\Gamma_R = 8.0 \times 10^{-2}$ mol·cm^{-2}, for the oxidized and reduced forms. The much lower conversion values for the mutants, compared to those measured for linker bf 1 by itself, suggest that there is an additional process that is involved, namely, the redox reaction of NADH. Taking into account the redox potential measured for mutant D314Az and the fact that it is identical to the redox potential of linker **1**, but with much lower reversibility, it is suggested that the degree of mediation of ET between NAD^+ and the quinone containing linker is much lower than for mutant V66Az.

Using the calculated values based on eq 1 and knowing the approximate surface area of our electrode, we could estimate the number of active enzymes bound to the surface.

$$\text{Equation 1: } I_P = \frac{\left[n^2 F_2 \Gamma A v\right]}{4RT}$$

where I_P is the current at the peak (anodic peak or cathodic peak), n is the number of electrons in the reaction, F is the Faraday constant, R is the gas constant, T is the temperature in Kelvin (in this case, 298 K), A is the electrode surface area in cm^2, Γ is the surface coverage in mol·cm^{-2} for the anodic or the cathodic process, and is the potential scan rate in V s^{-1}.

These values can be translated to the number of redox active enzyme copies displayed per bacterium that varied between ∼160,000 copies for bacteria displaying mutant D314Az and ∼480,000 copies for bacteria displaying mutant V66Az. These numbers are in good agreement with the reported performance of the bacterial autodisplay system [114]. However, these numbers do not agree with our previously reported numbers based on our attachment of gold nanoparticles to the enzymes and a cautious count of the number of nanoparticles, when we reported an approximate 11,000 copies per cell [110]. The difference could stem from several reasons: one was our avoidance of counting gold nanoparticles that have aggregated, and another could be that gold nanoparticles failed to bind all displayed enzymes.

3.4.5 ET Measurements and Mutant Comparisons

We have used Laviron's analytical approach for cases of peak to peak separation of $\Delta E_P > 200$ mV/n (n being the number of electrons)[115] to calculate the transfer coefficient α and the apparent rate constant k_{app} for mutants V66Az and D314Az. We did not conduct calculations for mutant P182Az since it has exhibited similar peak potentials as mutant V66Az, probably due to similar distances from the NAD^+ binding pocket. Figure 3.9 A shows the voltammograms collected upon picking up a bacterium that displayed ADHII mutant V66Az on its surface. Due to very low peak currents compared to catalytic currents present in the voltammograms, we are not showing the full range of potentials that were scanned in each experiment, only the region in which the peaks have appeared (the full scale voltammograms are shown in Figure 3.10). For mutant V66Az, the formal potential, $E^{0'}$ was calculated to be –250 mV vs Ag/AgCl. This relatively high potential is an indication that indeed the electrons are being transferred from NADH through the quinone and not just from the quinone that is directly bound to the surface. The middle point potential that was measured for the quinone used in this study is –350 mV vs Ag/AgCl (Figure S2B, Supporting Information). Transfer coefficients α and 1– α were calculated to be 0.4 and 0.6, respectively, whereas k_{app}, the electron transfer rate constant, varied in the different measurements between 5.6 and 7.2 s^{-1}. These values are in good agreement with values reported in the literature for electrodes modified with quinone derivatives to mediate NADH enzymatic oxidation, where the enzymes were randomly oriented relative to the electrode [116]. These values are significantly higher than values reported for ADH/toluidine blue O/nafion electrodes modified nonspecifically, at a value of 0.12 s^{-1} [109].

The same measurements were conducted with surfaces modified with bacteria displaying mutant D314Az (Figure 3.9 B). The measured formal potential was $E^{0'}$ = –350 mV vs Ag/AgCl. Since this potential is the same as the one that we have measured for linker **1** alone, we assume that we have measured in this case the ET process between the quinone and the electrode almost exclusively without the ability to successfully mediate ET between the quinone and the NAD^+ in the remote binding pocket. Using Laviron's approach for the analysis of the ET

process for this mutant, the transfer coefficients, α and $1 - \alpha$, were calculated to be 0.15 and 0.85, respectively. The measured k_{app} was 1.2–1.5 s^{-1}. Here, we must note that the measurements for the cathodic peaks of both mutants were done by a mathematical deconvolution (detailed explanation appears in the Experimental Section) due to reductive catalytic peaks that appeared in more negative potentials probably due to bacterial lysis on the surface. Furthermore, due to a very small number of redox active molecules on the surface (in the range of hundreds of thousands only per measurement), measured currents are extremely low, in the picoampere range, the limit of our measuring abilities. Nonetheless, in the region of middle point potentials, a marked increase in capacitive currents was observed, which lead us to believe that a Faradaic process is taking place in that region. Lysis of bacteria may occur due to large forces applied to bacteria by the AFM tip during imaging caused by the relatively high stiffness of the probe.

The k_{app} value calculated for linker **1** when it was bound to the electrode surface varied between 5.75 and 7.5 s^{-1} in our different measurements with a surface coverage that is about 2.3×10^{-10} mol·cm^{-2}, whereas surface coverage of mutant D314Az was an order of magnitude lower, with a much lower ET rate constant (within the error of the measurement). This value is lower than that calculated for mutant V66Az, where the mediated ET is evident due to the very low conversion rate between oxidized and reduced forms as well as the positively shifted middle point potential. All of these results together strengthen our conclusion that the NADH is hardly involved in this reaction (using mutant D314Az) since it is too far (at least 42 Å away from the quinone). Our earlier studies with the same mutants have shown much lower bioelectrocatalytic activity for mutant D314Az [110].

3.5 Conclusion

Using an integrated conducting AFM for single cell electrochemical analysis, we were able to obtain a detailed understanding of enzyme electron transfer processes to electrodes. We were able to determine the surface coverage of the electrode and, by imaging a single bacterium, calculate the number of surface dis-

played redox enzymes for the first time without using biochemical tools. We could study different mutants and their characteristic ET rate constants as well as redox potentials. Through multidimensional experimental results, we were able to show that, when the distance between a mediator and an active enzyme binding pocket is too large, hardly any mediation occurs. In contrast, when the distance between the enzymatic active site and the redox mediator is small (5 Å in this case), mediation of ET occurs that is reflected in the fast ET as predicted by theory. The surface density by the autodisplayed enzymes is very close to surface densities reported for enzymatic electrodes that contained ADH with larger dimensions [109]. These results strongly suggest that the enzyme expression density in our system is relevant for studies using "enzymatic-like" electrodes. In summary, our combined AFM-electrochemical system can be used as a platform for single cell analysis of enzyme activity; such information is critical for efficient design, development, and study of bioelectronic systems.

Chapter 3, in full, is a reprint of the material *Alfonta L, Meckes B, Amir L, Schlesinger O, Ramachandran S, Lal R. Measuring Localized Redox Enzyme Electron Transfer in a Live Cell with Conducting Atomic Force Microscopy. Analytical Chemistry. 2014; 86(15):7674–80.* The dissertation author was the primary author.

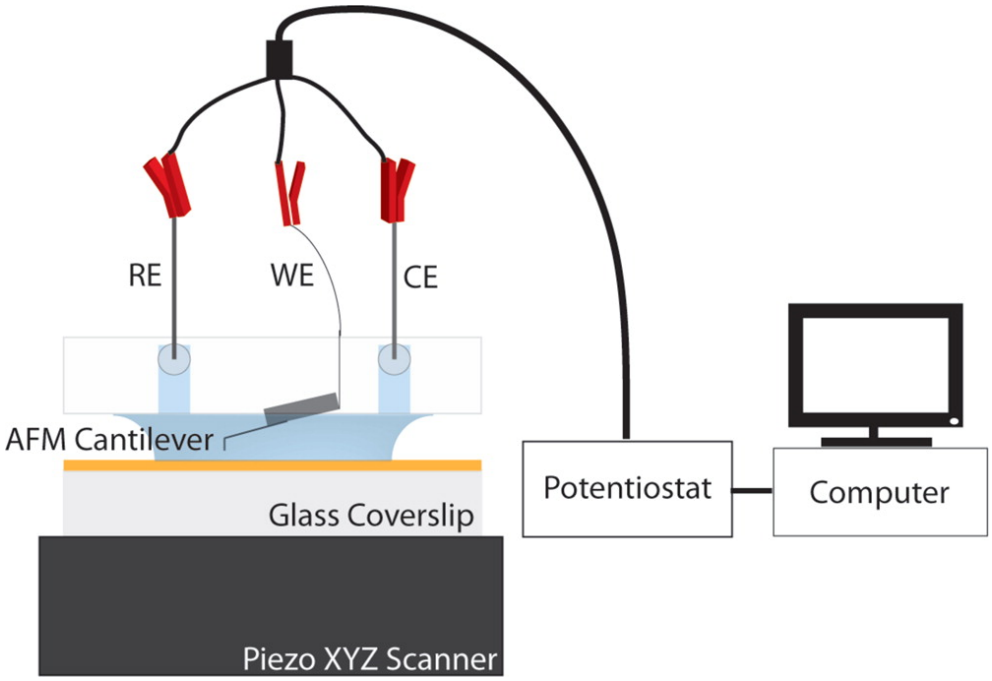

Figure 3.1: **Schematic Description of the EC-AFM Setup.** The materials for the electrodes, reference (RE), working (WE), and counter (CE), were Ag/AgCl, Au, and platinum, respectively.

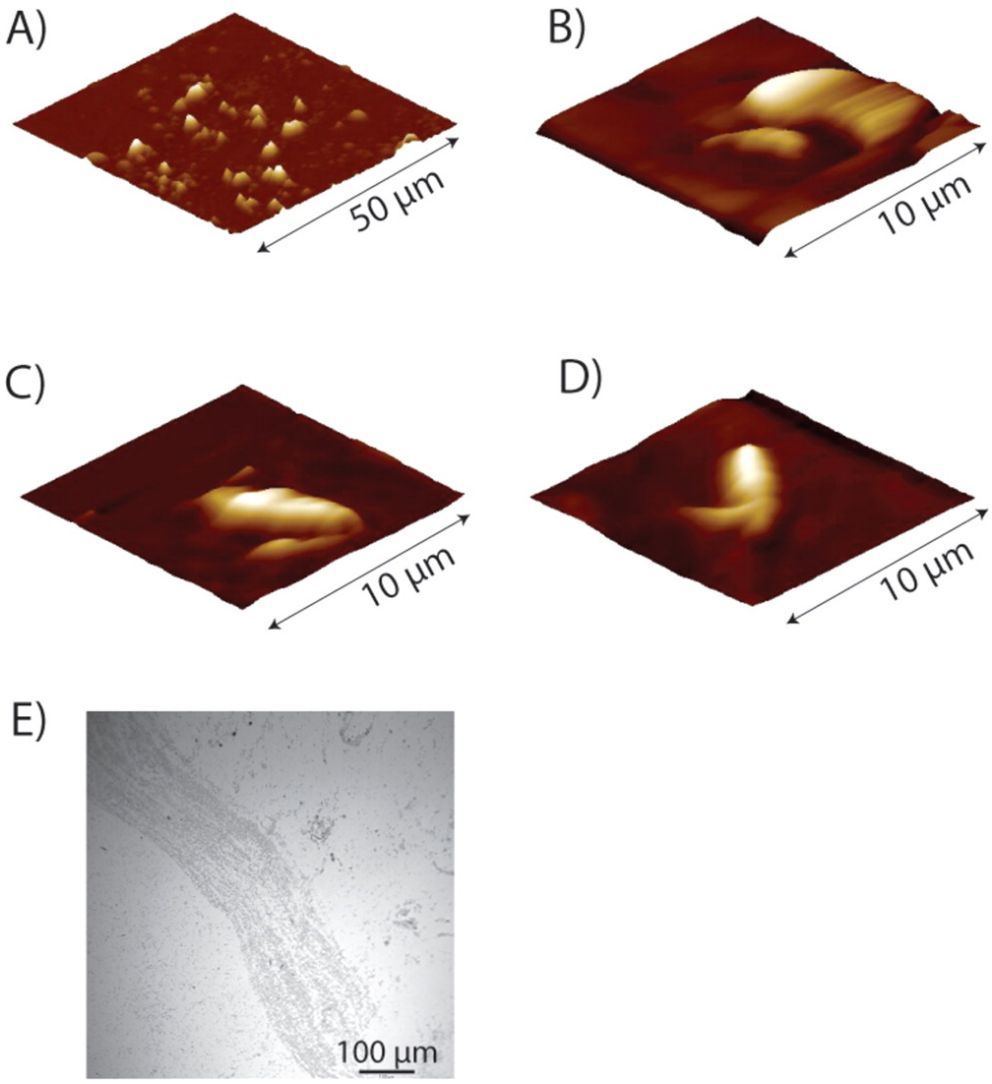

Figure 3.2: **AFM images of the surface with bacteria at different stages of tip manipulations.** **(A)** Large scan area with D314Az mutant bacteria. **(B–D)** Scans of single bacterium used in electrochemical measurements of V66Az **(B)**, D314Az **(C)**, and WT **(D)**. **(E)** Light microscopy images of bacteria attached to the gold substrate.

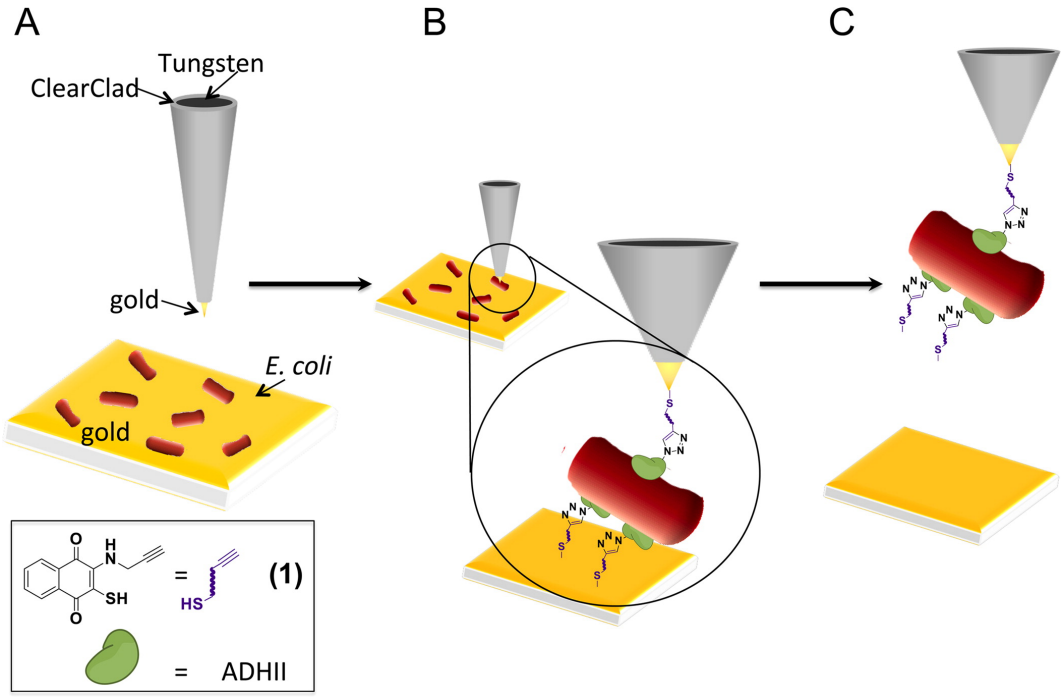

Figure 3.3: **Description of the sequence of operations conducted in order to lift a single bacterium off the surface using a gold coated AFM tip.**

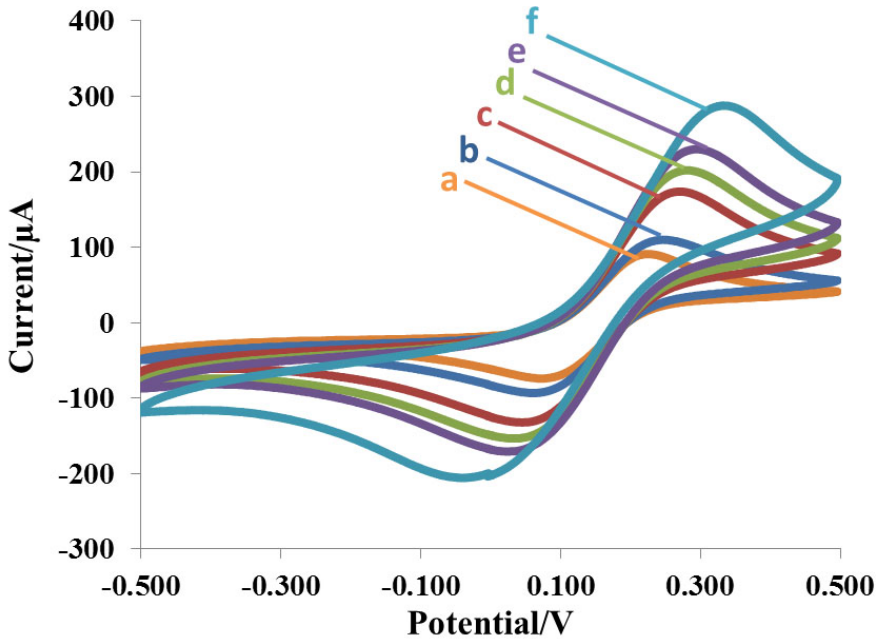

Figure 3.4: **Cyclic voltammograms of 10 mM Hexacyanoferrate (II/III) (1:1 ratio) at various scan rates.** **(a)** 10mV/sec, **(b)** 20mV/sec, **(c)** 50mV/sec, **(d)** 75mV/sec, **(e)** 100mV/sec, **(f)** 200mV/sec. All measurements were performed in 0.1M Tris buffer pH=8 with daily freshly made Ag/AgCl reference electrode.

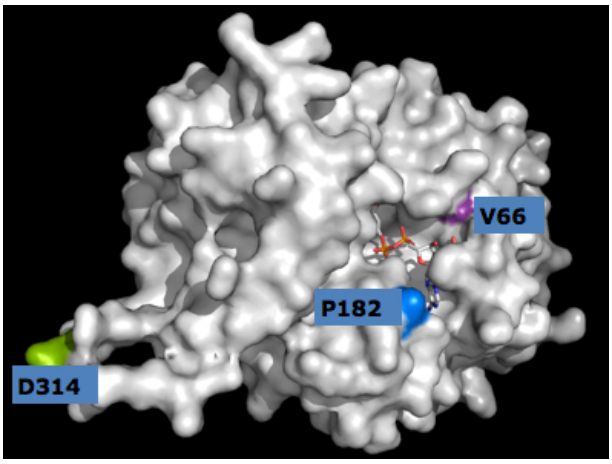

Figure 3.5: **Three-dimensional model of ADHII from** *Z. mobilis*, **with its NAD$^+$ cofactor.** Mutation sites V66, P182 and D314 are highlighted.

Table 3.1: **Distance from the NAD^+ binding pocket for various ADHII mutants are shown**

Mutant	Distance from NAD^+
V66	5.6 Å
P182	4.7 Å
D314	42 Å

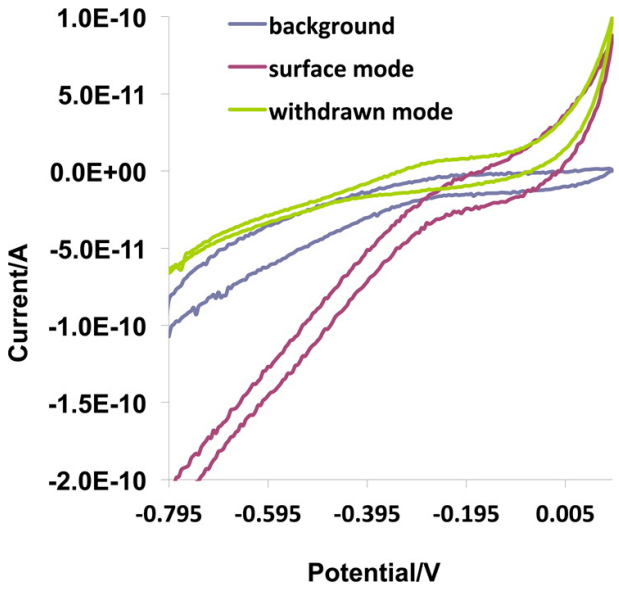

Figure 3.6: **Cyclic voltammograms collected at every mode of bacterium selection.** Background: before engaging the surface. Surface mode: engaging with a single bacterium. Withdrawn mode: withdrawing upon attachment of a bacterium. Scan rates were 0.05 V s^{-1}; reference electrode: Ag/AgCl wire.

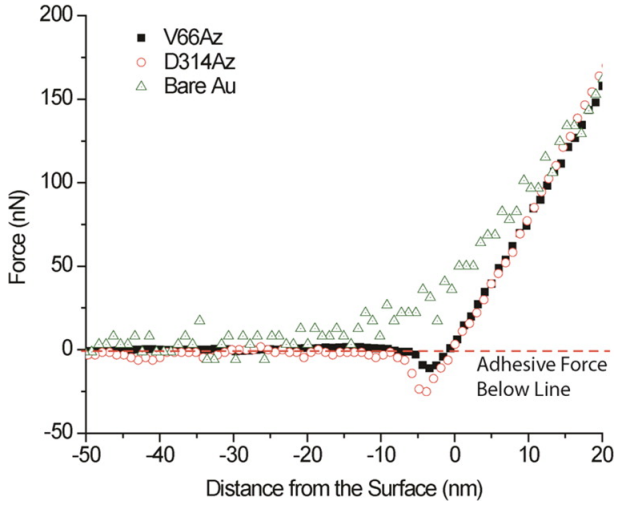

Figure 3.7: **AFM retraction curves are shown for ADHII mutants V66Az and D314Az during cantilever attachment to a single bacterium.** Adhesion forces are visible for both mutants. Bare gold substrates are shown as a control.

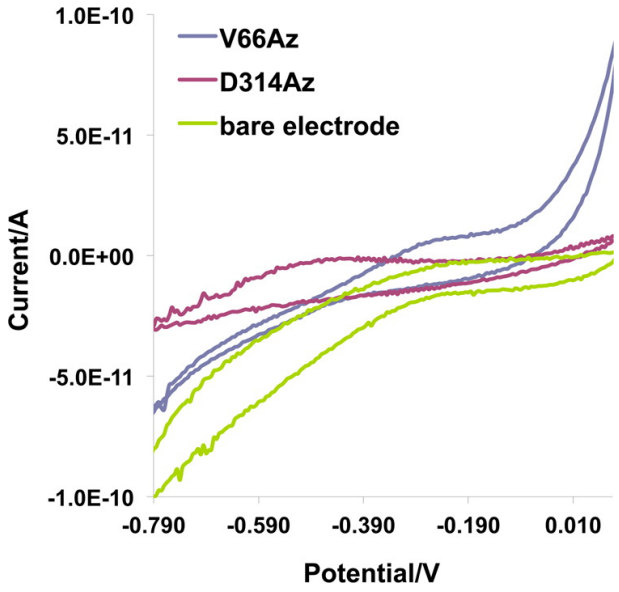

Figure 3.8: **Cyclic voltammograms of the different mutants.** Lavender colored line: mutant V66Az; rose colored line: mutant D314Az; lime green colored line: background measurement with an unmodified working electrode. Scan rates were 0.05 V s^{-1}; reference electrode: Ag/AgCl wire.

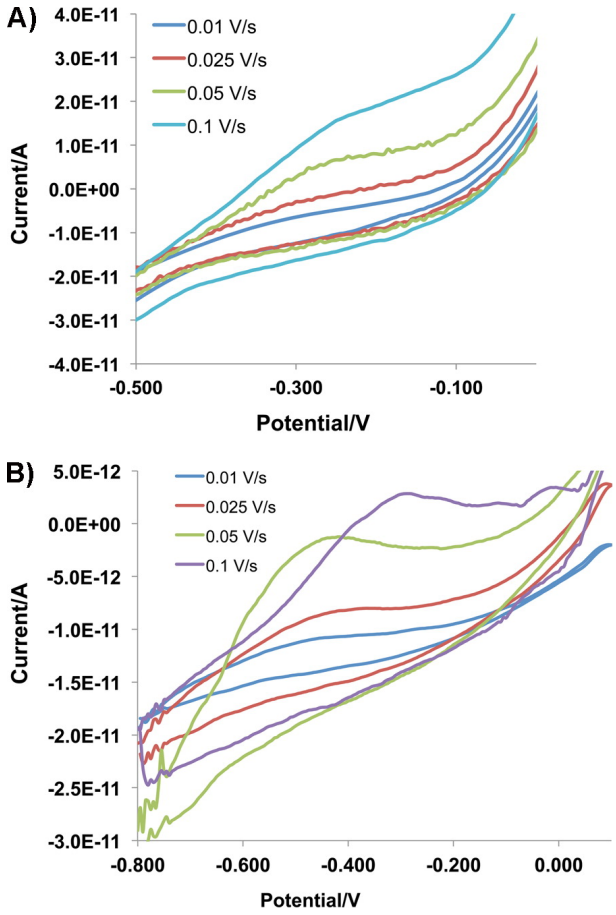

Figure 3.9: **Cyclic voltammograms performed on different bacteria with varying scan rates.** **(A)** Cyclic voltammograms conducted under different scan rates for mutant V66Az. **(B)** Cyclic voltammograms conducted under different scan rates for mutant D314Az. The range was limited to emphasize the peaks.

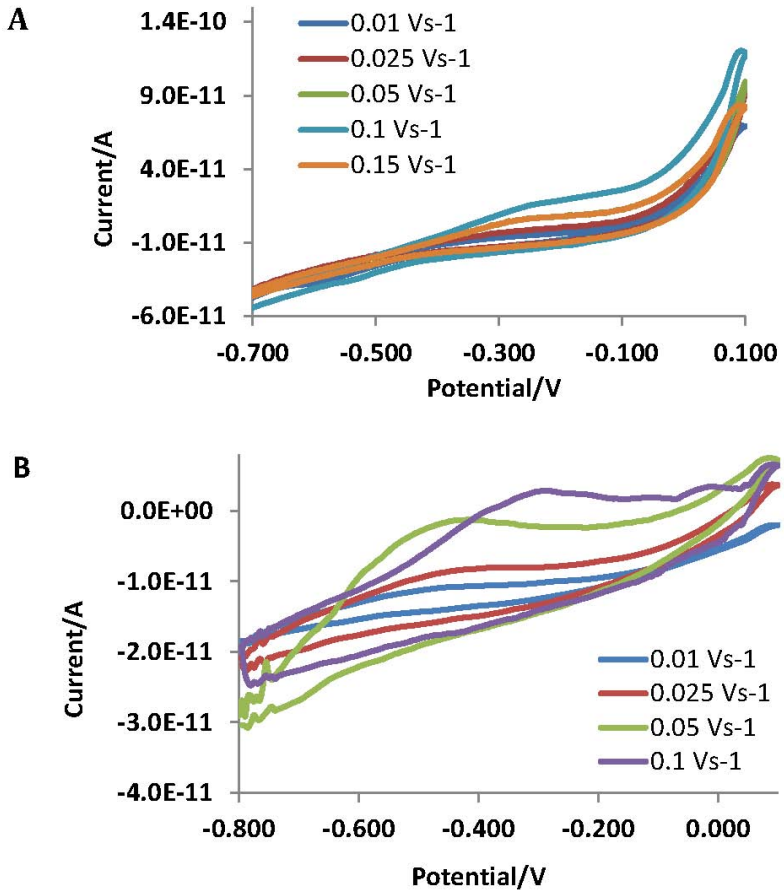

Figure 3.10: **Full range of cyclic voltammograms.** **(A)** Cyclic voltamograms conducted under different scan rates for mutant V66Az. **(B)** Cyclic voltamograms conducted under different scan rates for mutant D314Az.

Chapter 4

Atomic Force Microscopy Shows Connexin26 Hemichannel Clustering in Purified Membrane Fragments

4.1 Abstract

Connexin proteins form hexameric assemblies known as hemichannels. When docked to form gap junction (GJ) channels, hemichannels play a critical role in cell–cell communication and cellular homeostasis, but often are functional entities on their own in unapposed cell membranes. Defects in the Connexin26 (Cx26) gene are the major cause of hereditary deafness arising from dysfunctional hemichannels in the cochlea. Structural studies of Cx26 hemichannels properly trafficked and inserted in plasma membranes, including their clustering that forms a plaque-like feature in whole gap junctions, are limited. We used atomic force microscopy (AFM) to study the surface topography of Cx26 hemichannels using two different membrane preparations. Rat Cx26 containing appended carboxy terminal V5 and hexahistidine tags were expressed in baculovirus/Sf9 cell systems. The expressed Cx26 proteins form hemichannels in situ in Sf9 cells that were then purified either as (1) Sf9 membrane fragments containing Cx26 hemichannels or (2) solubilized hemichannels. The latter were subsequently reconstituted in lipo-

somes. AFM images of purified membrane fragments showed clusters of protein macromolecular structures in the membrane that at higher magnification corresponded to Cx26 hemichannels. Hemichannels reconstituted into DOPC bilayers displayed two populations of channel heights likely resulting from differences in orientations of inserted hemichannels. Hemichannels in the protein rich portions of purified membranes also showed a reduced channel height above the bilayer compared to membranes with reconstituted hemichannels perhaps due to reduced AFM probe access to the lipid bilayer. These preparations of purified membranes enriched for connexin hemichannels that have been properly trafficked and inserted in membranes provide a platform for high-resolution AFM imaging of the structure, interconnexon interactions, and cooperativity of properly trafficked and inserted noncrystalline connexin hemichannels.

4.2 Introduction

The connexin (Cx) family of proteins is a group of ubiquitously expressed transmembrane proteins with high conservation of structure and genetics between species. Cx proteins form assemblies in the cell plasma membranes known as hemichannels (or connexons) consisting of 6 Cx subunits. Hemichannels on apposing cells dock together to form gap junction (GJ) channels that facilitate cell–cell communication through transport of ions, metabolites, and other small molecules between neighboring cells. Undocked hemichannels have been shown to be present in cells [65] and have demonstrated ionic conductance states as well as metabolite, dye, and Ca^{2+} transfer [66, 117, 118, 119, 72]. Gating of hemichannel and GJ channel activity is regulated by many factors, including Ca^{2+}, pH, phosphorylation, and redox state [70, 120, 121, 122]. During oxidative stress, hemichannels lose regulation leading to unchecked hemichannel opening that ultimately results in cell death [74, 123]. To better understand the structures that determine the activity of hemichannels, imaging of these structures within membrane environments must be performed.

Previous imaging has extensively revealed subnanometer resolution 3-D

structures of Cx hemichannels and GJ channels using X-ray crystallography, X-ray diffraction, and electron crystallography [78, 79, 48, 80]. All are based on crystallized or quasi-crystallized arrangements of GJ channels. In contrast, atomic force microscopy (AFM) allows high resolution imaging of noncrystalline biological samples in aqueous, nonstatic environments. Previously, high resolution AFM images of the extracellular surface of Cx26 hemichannels derived from force dissected quasi-crystalline dodecameric channels showed fine details and conformational changes in response to either Ca^{2+} or low pH [69, 124]. However, native undocked hemichannels exist in noncrystalline clusters and populations are often diffuse in the native membrane environment. The open and closed states of Cx43 and Cx40 hemichannels reconstituted in lipid bilayers contained noncrystalline patches of membrane bound hemichannels that showed Ca^{2+} induced conformational changes when exposed to high Ca^{2+} concentrations [21, 68]. However, reconstitution of hemichannels does not always mimic the native composition of eukaryotic plasma membranes and can have widely varying protein densities. It also lacks the cellular control for correct, directed trafficking and insertion of hemichannels into membranes. In order to overcome this limitation, we have utilized purified membrane fragments from cells expressing Cx26 hemichannels at high levels.

In this study, we focused on imaging of noncrystalline Cx26 hemichannels, which allows for easier high resolution imaging due to their shorter cytoplasmic C-terminal domain. Connexins share a common topology with high sequence conservation in their N-terminus, transmembrane domains, and extracellular loops. Connexins larger than 40 kDa have C-termini that contain as much mass as the transmembrane and extracellular domains combined. The amino acid sequences of the connexin C-termini vary considerably, with each containing critical regulatory regions essential to channel function. The cytoplasmic domains are very flexible and probably act similarly to intrinsically disordered proteins [49]. This inherent flexibility has made imaging high resolution structural details difficult.

Here, we report AFM imaging of noncrystalline Cx26-V5-His6 hemichannels expressed through baculovirus infected Sf9 insect cells. We take advantage of the fact that connexins readily form hemichannels or channels in the membranes

of baculovirus infected Sf9 cells that allow for purification of milligram quantities of hemichannels. It is important to emphasize that we studied Cx26 not only for its short C-terminus, but also because genetic defects in the human *gjbeta2* gene (Cx26) are the leading cause of the most common type of hereditary congenital hearing impairment due to altered structure that can prevent docking of hemichannels or alter trafficking of molecules through the channels [125, 126, 127]. We used purified membrane fragments of Sf9 cells containing Cx26 hemichannels to image the structure of dispersed hemichannels in membranes and compared these to images of purified hemichannels reconstituted in 1,2-dioleoyl-sn-glycero-3-phosphatidylcholine (DOPC) liposomes. The hemichannels expressed in the purified membrane fraction of cells showed regions of clustering. The protrusion of hemichannels above the membrane was reduced in comparison to the reconstituted hemichannel preparations.

4.3 Methods

4.3.1 Baculovirus Expression of Hemichannels in Insect Cells

Rat Cx26-V5-His6 (NCBI Reference Sequence: NM_001004099.1) was expressed through cloning into a pBlueBac baculovirus system as previously described [128]. Baculoviruses were generated and used for subsequent infection of *Spodoptera frugiperda* (Sf9) cells. The techniques for applying this to expression of connexin hemichannels have been described extensively in our previous publications [126, 128, 85, 129].

4.3.2 Insect Cell Membrane Purification

In Sf9 cells, Cx26 readily forms channels and hemichannels in the plasma membrane and internal membranes. Hemichannel expressing Sf9 cell membranes were purified using our published protocol [85]

4.3.3 Hemichannel Purification

Solubilized hemichannel proteins were purified from baculovirus expression in Sf9 cells utilizing the hexahistidine tag for affinity purification, as we have previously reported [78, 126, 128, 85, 130].

4.3.4 Reconstitution of Hemichannels

1,2-Dioleoyl-sn-glycero-3-phosphatidylcholine (DOPC) lipids (Avanti Polar Lipids, Alabaster, AL) (5 mg/mL) in chloroform were vacuum-dried. The lipids were then resuspended in 150 mM KCl, 10 mM HEPES, 1.8 mM $MgCl_2$ buffer (pH 7.5) (final DOPC concentration of 0.8 mg/mL) with n-octyl-β-d-glucoside (OG) (5 mg/mL). The mixture was briefly vortexed followed by 15 min of sonication to create mixed detergent–lipid liposomes. Purified Cx26-V5-His6 hemichannels in elution buffer were added at 1:200 to the liposomes. The mixture was sonicated for 2 min and then gently mixed for 1 h at 4 °C. The detergent was removed to create proteoliposomes by treatment with Biobeads (Bio-Rad Laboratories, Hercules, CA) (0.1 g/mL) twice for 2 h or overnight at 4 °C.

4.3.5 AFM Imaging of Hemichannels

Imaging was performed on a multimode atomic force microscope with a Nanoscope IIIA or Nanoscope V controller utilizing a fluid cell (all from Bruker, Santa Barbara, CA). A TRP300A cantilever (Asylum Research, Santa Barbara, CA) with spring constants 0.02 N/m (contact mode) and 0.08 N/m (tapping mode) was used for all imaging. For imaging of the reconstituted hemichannels, proteoliposomes were deposited on freshly cleaved mica (20 μL) and allowed to attach for 30 min. The sample was heated for 5 min at 37°C to induce liposomal fusion. The sample was then rinsed 3 times with "imaging buffer" (10 mM HEPES, 1 mM PMSF, pH 7.4) and then imaged in appropriate buffer. For imaging of membrane fragments containing hemichannels, 20 μL of the Sf9 membrane suspension was deposited on mica. The mica had been incubated with "pretreatment buffer" (10 mM HEPES, 1 mM PMSF, pH 8.5) that we found reduced rolling or folding

of the flexible membranes. After a 10 min incubation to allow absorption of the membrane fragments onto the mica, samples were rinsed twice in "pretreatment buffer" and then rinsed in an imaging buffer (10 mM HEPES, 1 mM PMSF, pH 7.4) just prior to imaging in the buffer. Images were taken with raster scans at rates between 1 and 2 Hz for tapping mode images and 5–10 Hz for contact mode. The samples were imaged with scan sizes ranging from 10 μm $\times$ 10 μm to 100 nm $\times$ 100 nm. High resolution images were taken with pixel sizes less than 1 nm.

4.3.6 Gel and Western Blots

Isolated membranes and purified hemichannels were checked for purity by gel staining for protein bands and Western blots. Between 5 and 15 μL of sample were mixed with 2x Novex Tricine SDS Buffer (Life Technologies, Carlsbad, CA LC1676) in the presence of 5% BME. The samples were boiled for 10 min and loaded on 4–20% SDS-PAGE gel for electrophoresis. For protein staining, the gels were then fixed and stained with SYPRO Ruby solution (Life Technologies S-12000) overnight. For Western blots, the gels were transferred to PVDF membrane using the iBlot dry blotting system. Band detection was performed using the Li-Cor Odyssey Fc (Li-Cor Biosciences, Inc., Lincoln, NE) after reaction with ECL Luminata Forte (EMD Millipore, Billerica, MA).

4.3.7 Analysis of Lipid Bilayers Containing Cx26 Hemichannels

Lipid bilayers were deposited on mica substrates following the procedure described for preparing reconstituted hemichannels for AFM imaging. The mica substrate was broken into pieces and put into 1.5 mL Eppendorf tubes. Twenty microliters of loading sample buffer, Novex Tricine SDS Sample Buffer (Life Technologies) mixed with 5% BME, was added to the tubes. The tubes were then boiled for 10 min in a thermo block and loaded on an SDS gel PAGE 4–20% acrylamide for Western blotting. Band detection was performed with an anti-His primary antibody (Life Technologies) and an anti-mouse fluorescent secondary antibody and

imaged by an Odyssey Fc instrument.

4.3.8 Electron Microscopy

Samples of isolated membranes (5 μL) were applied to carbon coated grids, rinsed with ddH20, negatively stained with 2% uranyl acetate, and then air-dried. Electron microscopy (EM) was performed by using a 120 kV FEI Tecnai transmission electron microscope (FEI, Hillsboro, OR). Images were acquired at 30,000 magnification using a TVIPS TemCam-F224 2k $\times$ 2k CCD camera (TVIPS, Gauting, Germany).

4.3.9 Data Analysis of AFM Data

Images were initially processed using the Nanoscope Analysis 1.4 software package (Bruker, Santa Barbara, CA) to apply image flattening to correct for piezotube motion artifacts and a low pass Gaussian filter to eliminate electrical and mechanical noise. We used the Origin Pro 7.5 software package (OriginLabs, Northampton, MA) to determine the mean bilayer heights by plotting a histogram of the pixel heights and then fitting Gaussian curves to each histogram to determine the peak and standard deviation of the distributions. All subsequent statistical analyses were also performed with Origin Pro 7.5. All statistical values are reported as mean $\pm$ standard deviation.

4.4 Results

Baculovirus Sf9 infected cells are an excellent system for expressing eukaryotic proteins in quantities typically required for structural biology experiments. In the case of connexins, the protein subunits oligomerize to form hexamers or dodecamers in situ that have been shown to be structurally and functionally the same as proteins expressed exogenously in other cells or in native systems [117]. The resulting hemichannels were either (1) recovered in the membrane fragment fraction of the expressing cells or (2) solubilized from cell membranes and purified

as detergent stabilized hemichannels.

4.4.1 EM and Biochemical Validation of Purified Membranes Containing Hemichannels

Protocols for purifying GJs depend on the fact that the intrinsic protein to lipid ratio is high in these membrane specializations and increased after detergents extractions, making density gradient separation methods effective for isolating highly enriched fractions containing GJs. Hemichannel-containing membranes also had a high protein to lipid ratio, and thus, these same methods yield good results for our hemichannel membranes as well [131]. To purify membranes containing Cx26 hemichannels, partially disrupted membranes were collected utilizing a membrane selective sucrose gradient followed by washing with detergents. Because density gradient fractionation is selective for overall density but not for protein composition, we concentrated and further enriched membrane fragment fractions containing high density expressions of Cx26 by taking advantage of the genetically appended His6 tag binding to Ni-NTA beads for affinity separation.

Following successful purification of membrane fragments containing hemichannels, the membrane fragments were imaged with EM (Figure 4.1). Electron micrographs of uranyl acetate stained purified membrane fragments show the presence of hemichannel structures (Figure 4.1 B) whose appearance in these projection images we previously referred to as "doughnut-like". Gel staining and Western blotting of these membranes confirmed the presence of Cx26 proteins in the purified membrane fraction (Figure 4.1 C,D).

Membranes from uninfected Sf9 cells were imaged as a negative control. In this case, we did not use a Ni-NTA affinity purification step because there was no His6 tag expressed in this sample. No doughnut-like structures were seen in these uranyl-acetate stained membranes. Furthermore, only trace amounts of proteins were found within these membranes (Figure 4.1 C) and none of these very faint bands were identified as Cx26 in matched Western blots (Figure 4.1 D).

4.4.2 AFM of Purified Membrane Fragments with Cx26 Hemichannels

Purified membranes of Sf9 cells expressing Cx26 were deposited onto freshly cleaved mica and imaged in aqueous buffer (Figure 4.2). Membrane fragments greater than 500 nm in diameter were further imaged at high resolution to examine the Cx26 structure. Smaller bilayers were more susceptible to membrane disruption when imaged and thus, high resolution images of these proved difficult to record. Since the AFM z-resolution is very accurate, it was easy to identify single layers from double layers or folded membranes; heights greater than 12 nm were most likely either due to the presence of GJs (double membranes containing two docked hemichannels) or due to the superposition of hemichannel layers that occurred during sample deposition, respectively. Some of the bilayer fragments displayed inhomogeneity throughout the surface as cross section showed distinct clusters with two populations of bilayer thickness (Figure 4.2 A–D), while other fragments showed more homogeneous height profiles (Figure 4.2 E). The membrane in Figure 4.2 E contained small protein-rich islands in a lipidic membrane. The height difference between the two populations in the membranes exhibiting multiple heights was measured by first finding the pixel height in localized regions (outlined in Figure 4.3) and then plotting the heights as a histogram (Figure 4.3). Gaussian distributions fit to each histogram better quantified the height of the two bilayer populations. The height of the bilayers in the lower population was 5.9 ± 1.6 nm, which were not statistically different from the heights measured for the homogeneous membrane population 5.2 ± 0.6 nm (t test, $p > 0.05$). The step height difference between the lipidic and protein rich regions in the membranes was determined to be 1.8 ± 0.4 nm ($n = 6$ measurements). The regions of the bilayer displaying an increased thickness, we believe, contain greater concentrations of hemichannels. Magnified images of the membrane patches showed the presence of hemichannels dispersed throughout the membranes (Figure 4.4). The protrusion height of these hemichannels above the surrounding protein and lipid was limited to 0.4 ± 0.2 nm ($n = 18$). The dense packing and overall increased height in the step regions most likely contributed to this lower protrusion height

of the hemichannels.

4.4.3 EM and Biochemical Validation of Purified Detergent Stabilized Hemichannels

In our comparison of two ways of making hemichannel-containing membranes, we used purified hemichannels collected from baculovirus membranes via full membrane disruption and detergent solubilization. The DoDM detergent stabilizes membrane proteins to allow them to retain their structure and prevent aggregation. Detergent stabilized hemichannels were imaged with EM with uranyl acetate as the contrast agent (Figure 4.5). These channels were present in "doughnut-like" structures typical of hemichannels. Protein staining and Western blotting of SDS-PAGE confirmed the presence of Cx26 hemichannels as the primary constituent of the purified lysate. This evidence confirmed the successful purification of hexamer hemichannels for eventual reconstitution and imaging with AFM (Figure 4.4).

4.4.4 AFM Of Cx26 Hemichannels Reconstituted into Lipid Membranes

As we did for the isolated membrane preparations, we compared hemichannel containing reconstituted membranes to ones prepared without hemichannels. Prior to imaging bilayers formed by the proteoliposomes, bilayers formed from liposomes containing only DOPC were imaged to measure their size, heights, and surface structure. We used DOPC for hemichannel reconstitution because these lipids have a very low phase transition temperature (–17 °C), which facilitates the facile formation of bilayers, as has been previously documented [78, 21, 68, 130]. These lipid bilayers showed a step height of ∼5.5 nm (data not shown), consistent with dimensions from the literature on DOPC bilayer thickness [132]

Next, we imaged Cx26 hemichannels reconstituted into DOPC lipid bilayers. Purified Cx26 hemichannels were reconstituted in mixed DOPC/OG liposomes. The DoDM and OG were subsequently removed with polystyrene beads.

The DOPC proteoliposomes were deposited on mica and imaged with AFM in the presence of calcium free buffers to ensure open configurations of the hemichannels (Figure 4.6). The presence of hemichannel proteins in the liposomes was confirmed by Western blots of the deposited liposomes (Figure 4.6 D). These hemichannels were solely from the lipidic membranes on the mica since extensive washing of the sample in the AFM chamber was performed, thus removing any hemichannels in solution prior to this analysis.

Not all of the liposomes appeared to contain hemichannels. Some samples showed flat areas where no obvious protrusions were present (Figure 4.6 E). This indicates that the liposomes were not completely saturated with protein. The hemichannels reconstituted into DOPC bilayers displayed two distinct populations of hemichannels based on the protrusion heights (Figure 4.6 F–H). The measured hemichannel heights were fit to multiple Gaussians (Figure 4.7). The heights of the populations based on these fits were measured to be in two groups of 0.9 ± 0.3 nm and 2.3 ± 0.3 nm ($n = 58$), respectively. Small variations between the heights are most likely due to the influence of the imaging force. The protrusion height of the hemichannels imaged with AFM was statistically significantly greater for the reconstituted hemichannels compared to those imaged in the membranes ($p < 0.01$) (Figure 4.7).

4.5 Discussion

We report for the first time AFM imaging of noncrystalline Cx26 hemichannels in purified membranes expressed through baculovirus infection of insect cells. Preparations of native single (undocked) hemichannel layers isolated from mammalian cells have not been documented, most likely because they are too dispersed in the plasma membrane and do not survive the detergent enrichment. Most reports of single hemichannel layers were from mechanically or chemically split GJs. In addition, the trafficking of GJ channels in native mammalian systems is highly regulated [133] with the caveat that cells maintain only a small number of open hemichannels and subsets of open GJ channels [55]

Our Sf9 membrane preparations have the advantage of cellular trafficking of hemichannels to the membrane along with guided insertion of hemichannels into the membrane. Consequently, the hemichannels in a single membrane fragment face the same direction in the membrane bilayer (cytoplasmic or extracellular) compared to a random orientation when hemichannels are reconstituted into liposomes. AFM images of purified membrane fragments containing Cx26 hemichannels have patches where the lipid bilayers were thicker. This is likely due to the clustering of hemichannels in the membranes into protein-rich regions. GJ channels are well characterized to form clusters that favor improved interaction energy between cell membranes [53]. In the Owicki model of GJ channel clustering, long-range protein aggregation into GJ plaques arises from interparticle interactions as well as lateral pressures between the junction and the surrounding glycocalyx [134, 135]. Whether dense hemichannel packing occurs in internal membrane compartments (ER, Golgi apparatus, trafficking vesicles) has yet to be determined. Normal trafficking of hemichannels occurs through anterograde pathways after which they are fused into the plasma membrane and then coalesce on the edges of GJ plaques where they dock and form GJ plaques [136, 137]. Cx26 hemichannels in our present work appear to display aggregating behavior in some of the membranes as the proteins did not appear to be spread homogeneously throughout the membrane. Clustering of ion channels and receptors in single cell plasma membrane is not unusual, and they serve as important communication links between the cells and their surroundings [138]. Large lipidic patches of membrane could be observed (Figure 4.2, 4.1) next to the protein-rich regions. The step height between the protein-rich and lipidic membrane regions was 1.8 $\pm$ 0.4 nm. This step height is similar to protrusion heights for Cx26 GJ channels measured with EM, X-ray diffraction, and X-ray crystallography. Measurements of protrusion heights obtained from the X-ray crystallographic atomic model were 1.9 nm for the cytoplasmic domains and 2.3 nm for the extracellular domain [79]. It is important to note that this is probably an estimate since these GJ channels were not membrane embedded as well as the protrusion height measurement represented one-half the distance measured for the docked dodecameric GJ channel.

High resolution images of the cytoplasmic domains of the hemichannel were likely to be reduced slightly by the presence of the His6 and V5 tags on the Cx26 connexins. The presence of terminal tags would increase the floppiness of cytoplasmic side of the hemichannels and could possibly inhibit imaging slightly. The protrusion heights of the hemichannels measured in purified membrane fragments were lower than those previously reported for crystal and quasi-crystalline structures. The heights were likely reduced due to the high density and disorder of the surrounding proteins reducing the true height of the channel compared to its surrounding. The protrusion height of hemichannels in DOPC bilayers was observed to be greater than those found in the membranes with 0.4 ± 0.2 nm for the hemichannels in purified membrane fragments and 0.9 ± 0.3 nm and 2.3 ± 0.3 nm for the two populations of channels observed in reconstituted DOPC membranes. The greater protrusion height observed for the reconstituted proteins is likely a result of the AFM probe being able to access the membrane more easily due to lower hemichannel densities.

The protrusion height of the reconstituted hemichannels showed distinct populations likely due to differences in the cytoplasmic and extracellular structures. The measured protrusion height above the bilayer for the reconstituted channels measured by AFM was 0.9 ± 0.3 nm and 2.3 ± 0.3 nm. Fiber diffraction analysis of pellets containing partially oriented GJs revealed that the extracellular gap between two membranes with GJ channels was $\sim$3.5 nm thick, which would estimate extracellular protrusions of $\sim$1.8 nm [48]. Similar sizes were observed in density maps of Cx26 GJ channels reconstituted into DOPC membranes with extracellular gaps of $\sim$4 nm for reconstituted Cx26 in a DOPC membrane ($\sim$2 nm per an extracellular protrusion) [130, 139]. Measurements of the cytoplasmic tails have been more elusive due to the flexibility of the cytoplasmic tails. In the best structurally preserved part of the three layer structure, the cytoplasmic protrusion heights measured in these EM density maps were $\sim$2–2.5 nm for Cx26 containing a His_6 tag and a thrombin cleavage site of 6 amino acids, but without a 14 amino acid V5 epitope tag [130]. In addition, this structure was determined at 4 °C temperature, so the assumption is that it would be more rigid under these

conditions than in our room temperature AFM imaging chamber. It should also be noted that the X-ray crystallographic data were recorded from crystals flash frozen in liquid nitrogen. We found that, as measured with AFM, the cytoplasmic face of Cx26 hemichannels is highly sensitive to the applied force with decreases in the observed protrusion height from 1.7 nm at 50 pN of force to 0.2 nm at 70 pN in quasi-crystalline packing[69]. Dispersed hemichannel proteins should have increased flexibility allowing the proteins to flatten more easily due to the lack of a lattice structure. The intrinsically high flexibility of the cytoplasmic surfaces and hemichannel dispersion likely accounts for the population height observed for reconstituted hemichannel proteins. The hemichannels with lower protrusions of 0.9 ± 0.3 nm are most likely cytoplasmic while the larger protrusion heights (2.3 ± 0.3 nm) are the extracellular domains, which are more rigid.

We report high resolution AFM imaging of noncrystalline disordered Cx26 hemichannels expressed in membranes for the first time. Previous studies on the structure of hemichannels with AFM have revealed high resolution structures of hemichannels. Images of hemichannels that had been force dissected with AFM have revealed in great detail the structure of extracellular and cytoplasmic domains of hemichannels in quasi-crystalline structures [69]. However, these docked hemichannel systems vary from native hemichannel presentations, which involve formation of disordered hemichannel arrays in the plasma membrane and subsequently aggregate into GJ edges in order to dock [140]. Structures of disordered noncrystalline hemichannels have also been studied in reductionist systems involving reconstituted proteins in lipid bilayers [21, 68]. These systems fail to represent the complex environments seen in cellular systems where the proteins are trafficked to a plasma membrane, which contains diverse lipid compositions and other membrane proteins, before the hemichannels freely diffuse to the edge of a GJ [136, 137]. The system presented in this paper for AFM imaging allows study of connexin hemichannels in a more complex membrane environment that includes mixed lipid composition and other membrane proteins, which more closely mimics the environment of native cells. The behavior of the Cx26 hemichannels in the purified membrane environment differs from proteoliposomal systems through in-

creased density of channels and apparent aggregation of proteins in the membranes. In addition to showing clustering of properly trafficked connexin hemichannels, this system presents unique opportunities to study the structure of hemichannel proteins and their cooperative behavior using electrophysiological and high resolution imaging with AFM.

Chapter 4, in full, is a reprint of the material *Meckes B, Ambrosi C, Barnard H, Arce F T, Sosinsky G E, Lal R. Atomic Force Microscopy Shows Connexin26 Hemichannel Clustering in Purified Membrane Fragments. Biochemistry. 2014; 53(47):7407-14* The dissertation author was the primary author.

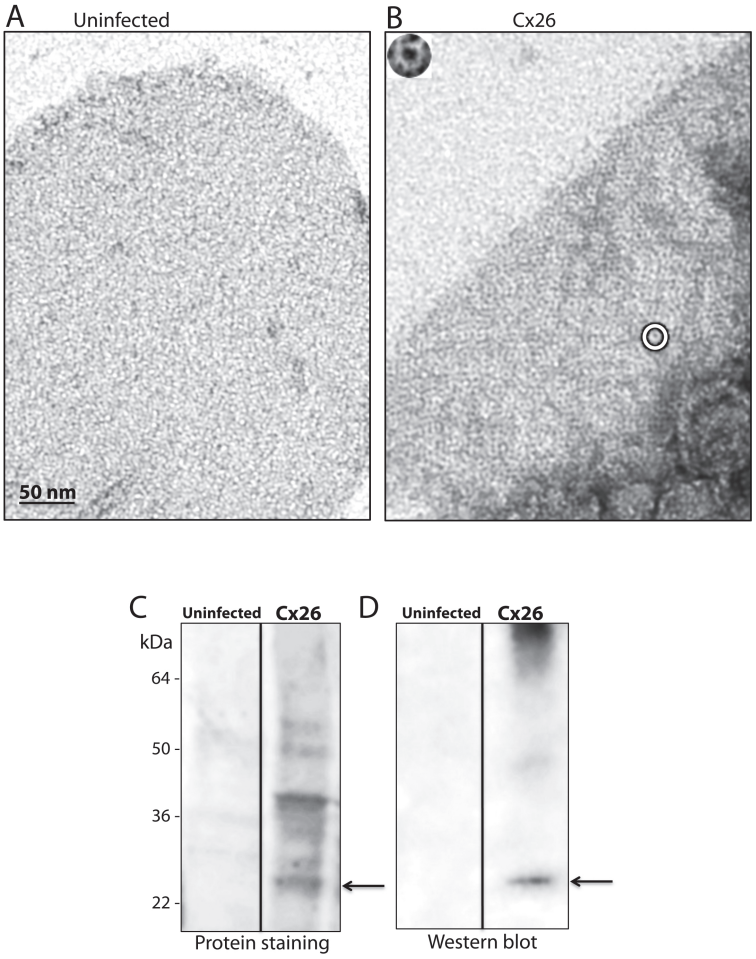

Figure 4.1: **EM and biochemical characterization of purified membranes from Cx26 expressing Sf9 cells. (A–B)** Representative electron micrographs of uranyl acetate stained purified membranes without Cx26 expression (uninfected) **(A)** and with Cx26 expression **(B)**. The inset in **(B)** shows a "doughnut-like" hemichannel structure present in the membrane (circled in white). **(C–D)** Protein staining **(C)** and Western blots **(D)** confirmed the presence of Cx26 in these preparations, while a similar analysis of uninfected cells did not contain any Cx26 bands. Oligomeric forms of Cx26 in the sample are due to protein aggregation when running the gel and are overemphasized in the Western blot

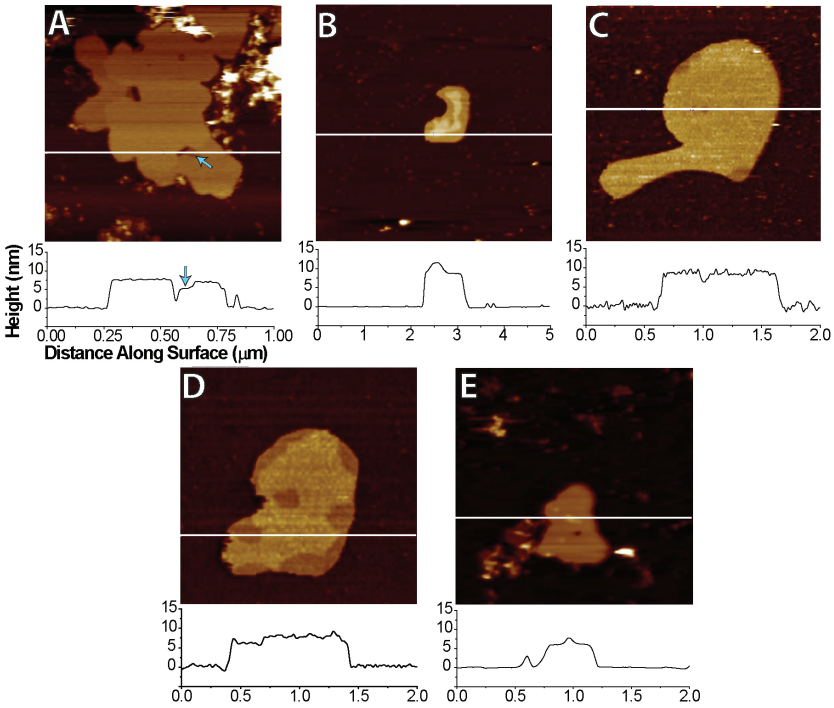

Figure 4.2: **AFM images of purified membrane fragments containing Cx26 hemichannels. (A–E)** Purified Cx26 hemichannel containing fragments were deposited on the mica substrate and imaged. Shown here are several AFM images of large (>500 nm) purified membrane fragments containing Cx26 hemichannels. The height profile section of the membrane (white line) is shown below its corresponding image. Note the difference in thickness between the purely lipidic domains and hemichannel containing regions. In **(A)**, the membrane shows three heights possibly due to proteins with different orientations and lipidic regions (arrow).

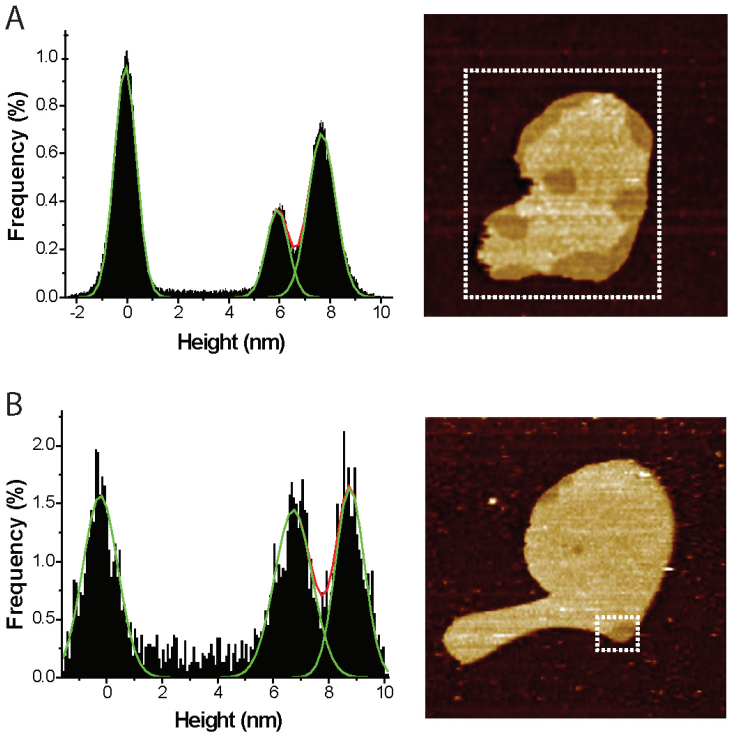

Figure 4.3: **Height histograms for two representative purified membrane fragments containing hemichannels.** **(A)** Histogram of the distribution of heights shows two populations of membrane height for a membrane fragment (boxed on right). **(B)** Height histogram of a small portion of a membrane (boxed on right) also displays two membrane heights. Gaussian curves were fit to the histogram data.

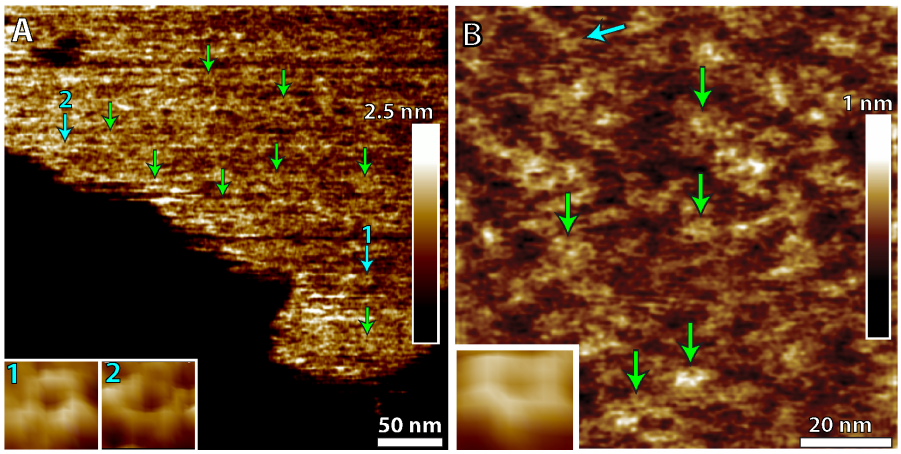

Figure 4.4: **AFM images of purified membrane fragments containing Cx26 hemichannels. (A)** Height image of a membrane fragment with disordered hemichannels (green arrows). Insets contain selected hemichannels that have been enlarged (cyan arrows numbered on figure). **(B)** High resolution height image of a membrane fragment containing many Cx26 hemichannels (green arrows). Inset shows an enlarged 3D image of a hemichannel present in the membranes (indicated by cyan arrow).

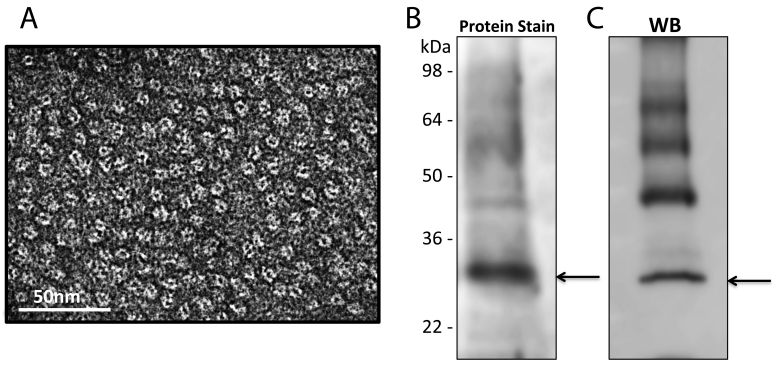

Figure 4.5: **EM and biochemical characterization of purified hemichannels from Cx26 expressing Sf9 cells.** **(A)** Electron micrograph of a uranyl-acetate stained Cx26 hemichannel preparation typically used for reconstitution into DOPC vesicles. **(B)** Staining an SDS PAGE with Sypro Ruby for protein content confirmed the presence of a strong Cx26 band in this sample that is further verified by Western blotting **(C)**. Oligomeric forms of Cx26 in the sample are due to protein aggregation when running the gel and are overemphasized in the Western blot.

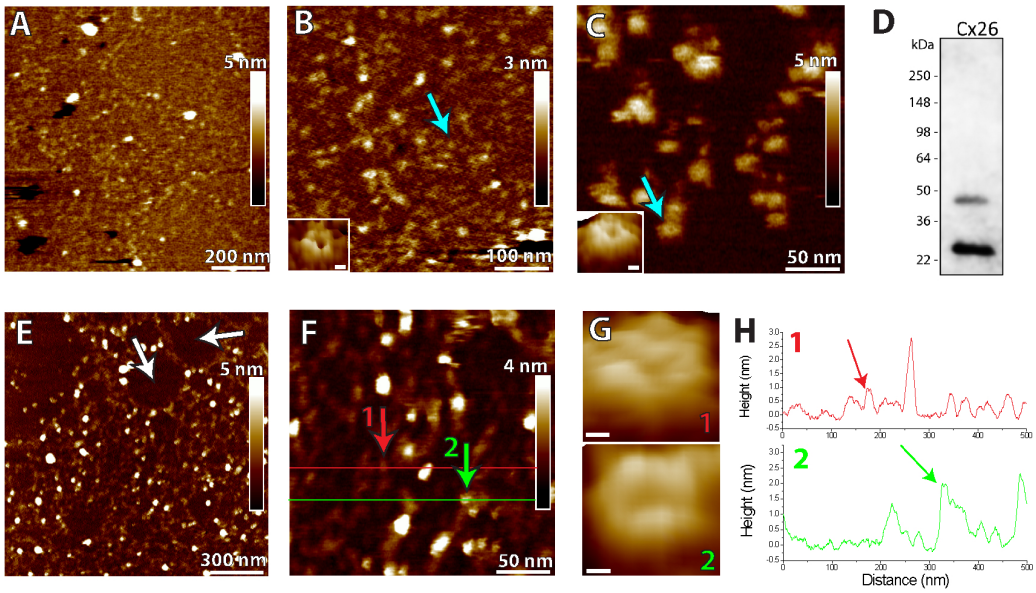

Figure 4.6: **Cx26 hemichannels reconstituted in DOPC liposomes and deposited on mica to form flat membranes.** **(A–C)** Hemichannels were observed in DOPC bilayers with insets showing zoomed images of the hemichannels (location indicated by cyan arrow, scale bar is 2 nm). **(D)** The presence of Cx26 in the liposomes was confirmed with a Western blot of liposomes deposited on the mica substrate. **(E)** Membrane patches with no hemichannels present (white arrows) were also observed indicating that some liposomes do not contain hemichannels. **(F)** Image showing the presence of hemichannels of different heights in the same bilayer. **(G)** Enlarged images of the channels highlighted in F (scale bar is 2 nm). **(H)** Cross-sections of the membrane showing the height of the membrane along the lines in F.

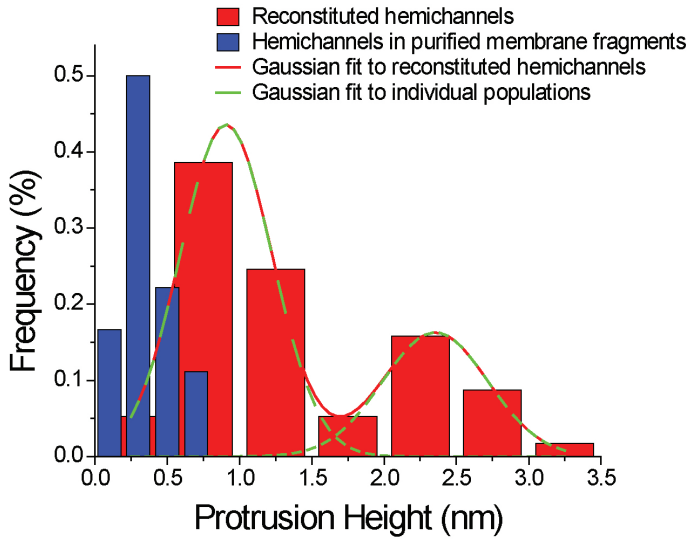

Figure 4.7: **Histograms of protrusion heights of Cx26 hemichannels in purified membrane fragments compared to populations of reconstituted hemichannels.** The mean protrusion height of hemichannels in the purified membranes (blue) was lower than for hemichannels reconstituted in DOPC liposomes (red). A Gaussian fit was applied to the two populations of heights observed for reconstituted hemi- channels (green line). The protrusion heights were measured as 0.9 $\pm$ 0.3 nm and 2.3 $\pm$ 0.3 nm reconstituted hemichannels and 0.4 $\pm$ 0.2 nm for hemichannels in purified membrane fragments.

Chapter 5

Graphene Nanopore Support System for Simultaneous High-Resolution AFM Imaging and Conductance Measurements

5.1 Abstract

Accurately defining the nanoporous structure and sensing the ionic flow across nanoscale pores in thin films and membranes has a wide range of applications, including characterization of biological ion channels and receptors, DNA sequencing, molecule separation by nanoparticle films, sensing by block co-polymers films, and catalysis through metal–organic frameworks. Ionic conductance through nanopores is often regulated by their 3D structures, a relationship that can be accurately determined only by their simultaneous measurements. However, defining their structure–function relationships directly by any existing techniques is still not possible. Atomic force microscopy (AFM) can image the structures of these pores at high resolution in an aqueous environment, and electrophysiological techniques can measure ion flow through individual nanoscale pores. Combining these techniques is limited by the lack of nanoscale interfaces. We have designed a

graphene-based single-nanopore support (∼5 nm thick with ∼20 nm pore diameter) and have integrated AFM imaging and ionic conductance recording using our newly designed double-chamber recording system to study an overlaid thin film. The functionality of this integrated system is demonstrated by electrical recording (<10 pS conductance) of suspended lipid bilayers spanning a nanopore and simultaneous AFM imaging of the bilayer.

5.2 Introduction

In recent years, advancement in fabrication techniques has led to novel nanoporous structures with an array of applications in biotechnology [141, 142, 143, 144, 145], polymer science [146], and energy [147, 148]. Small changes in the nanoscale features of these pores determine the specific conducting properties of ions through and around the pores [149, 150, 151]. Ion-conducting nanopores, including biological channels and receptors, may also interact with the surrounding environment and change over time. For example, living systems rely on the coordinated activity of membrane ion channels and receptors that control ionic and metabolic homeostasis and cell–cell/extracellular communications through regulation of ions, metabolites, and RNA transport. Dysfunction of ion channels is associated with pathophysiology and diseases such as Alzheimer's disease and Parkinson's disease, addiction, and some genetic disorders [152, 29, 153]. Improved therapeutic development, diagnosis, and/or prevention is therefore dependent on an accurate understanding of these channels' structure–activity relationship.

To fully understand the structure–function relationship of nanopore-containing thin films and membranes, structure and function must be correlated directly through simultaneous measurements. However, current techniques cannot provide real-time, direct, and simultaneous observation of the 3D structure and activity of these pores.

Atomic force microscopy (AFM) allows dynamic high-resolution imaging of biological samples in physiological environments [154, 31, 155, 138, 156, 157, 99], including 3D structures of individual ion channels in native hydrated environ-

ments [152, 29, 154, 158, 159, 160, 161, 162, 163, 164, 165]. The open interface of the AFM allows its integration with other techniques, including bilayer electrical recording and light/fluorescence microscopy. The missing link for integrating AFM imaging and electrical recording is a lack of an appropriate nanoscale support system. Nanopore samples have emerged as an exciting class of nanosensors that have gained attention for their sensitivity to conductance changes, especially in relation to the translocation of biomolecules, and numerous nanoporous devices have been made from natural, artificial, and hybrid materials [141, 143, 145, 166, 91, 167, 168, 169, 170, 171, 172]. Graphene is a promising and reliable material because of its unique mechanical, electronic, thermal, and optical properties [166, 168, 169, 22, 173, 174]. Graphene is thin enough to be precisely drilled using a transmission electron microscope (TEM) and is strong enough to be freely suspended over microscale pores [150, 166, 169, 175, 176]. Although much of the recent research on single-nanopore conductance has been directed toward the application of DNA sequencing or biomolecule translocation, micro- and nanopore devices have also been used to study the activity of ion channels [177, 178].

Here, we describe a novel graphene nanopore support system (Figure 5.1) for simultaneous localized high-resolution AFM and ionic conductance recording of nanoporous thin films. Solid-state single-nanopore support substrates were fabricated to fit into the open interface of the multimode AFM with our recently developed two–chamber system (Figure 5.1). We demonstrate the applicability of the integrated nanopore support system combining AFM imaging and electrical recording using suspended lipid bilayers. We show that a lipid bilayer deposited over the graphene nanopore seals the pore. These bilayers can be imaged repeatedly with AFM and retain their electrical properties. Electrical conductance measurements reveal a dramatic reduction in the conductance, >1 μS for the open pore to <10 pS, for the bilayer-covered pores, indicating complete coverage and sealing of the nanopore. The device and setup that we present here demonstrates the imaging resolution, nanopore size, and conductance sensitivity on scales compatible with what is needed for the structure–activity study of ion channels. The use of this technology would have major implications for, but not limited to, the

study of neurological disorders, pathological studies, therapeutic screening, and drug addiction.

5.3 Methods

5.3.1 Materials

Silicon oxide membranes (SiO_2) were purchased from AppNano (Mountain View, CA). Silicon oxide membranes are 200 nm thick and 20 $\times$ 20 μm^2 wide freestanding windows supported by a 300 μm thick silicon substrate. The windows were formed by KOH anisotropic etching of a 450 $\times$ 450 μm^2 opening on the backside of the silicon support (Figures 5.2 A and 5.3 A). Single-layer CVD graphene deposited on 20 μm thick Cu foil (2 $\times$ 2") was obtained from Graphene Supermarket (Calverton, NY). A Quanta 3D FEG focused ion beam (FIB) was used to drill through the SiO_2 suspended membrane. Either an iron(III) chloride hexahydrate ($FeCl_3 \cdot 6H_2O$; $\geq$98%) solution (Sigma Aldrich) or Copper Etch APS-100 (Transene Co.) was used to dissolve the Cu substrate of the graphene. Atomic layer deposition (ALD) of 5 nm of Al_2O_3 was performed using a GEMSTAR benchtop atomic layer deposition (ALD) process system or the Beneq TFS200 atomic layer deposition system. A transmission electron microscope (TEM) (JEOL 2010FEG, Japan) operating in bright-field imaging mode was used for drilling through the graphene/Al_2O_3 membrane layer. AFM imaging was completed using a multimode Nanoscope IV system and liquid cell (both from Bruker, Santa Barbara, CA) with silicon nitride cantilevers (k = 0.08 N/m, Asylum Research, Santa Barbara, CA). Conductance measurements were completed using a custom-designed Lexan polycarbonate double-chamber cup (Figure 5.1 C) and Ag/AgCl wire electrodes. Ecoflex Supersoft 5 silicone-cured rubber was used as an insulating sealant of the nanopore sample in the double-chamber cup. A patch-clamp amplifier (Dagan, Minneapolis, MN) was used for amplifying currents. Electrolyte solutions at pH 8.5 containing 1 M KCl buffered with 10 mM Tris, similar to Venkatesan et al., was used for AFM imaging in liquid and conductance measurements [179]. The phospholipid 1,2-diphytanoyl-sn-glycero-3-phosphocholine (DiPhyPC)

was purchased from Avanti Polar Lipids (Alabaster, AL).

5.3.2 Nanopore Fabrication Process

To fabricate a single nanopore support, the Si/SiO_2 substrates were used as a base for the processing (Figure 5.2 A). A single hole with a diameter of 1 μm was drilled by FIB through the center of the SiO_2 20 $\times$ 20 μm^2 suspended membrane area (Figures 5.2 B and 5.3 A). A sample of graphene on Cu was spin-coated with PMMA for 50 s and baked at 180 °C for 10 min. The Cu foil was completely dissolved in a $FeCl_3 \cdot 6H_2O$ solution or copper etchant APS-100 ($\sim$24 h). The remaining PMMA/graphene flake was deposited over the center of the cleaned SiO_2 membranes to ensure coverage of the entire 1 μm FIB hole area and was allowed to dry (Figure 5.2 C). Dried samples were soaked in acetone to dissolve the top layer of PMMA (Figure 5.2 D). Five nanometers of Al_2O_3 was deposited on the sample by ALD (Figures 5.2 E and 5.3 B). A nanopore was then drilled through the center of the graphene/Al_2O_3-suspended membrane by TEM (Figures 5.2 F and 5.3 C) [141, 180]. The nanopore sample was cleaned with acetone, isopropanol, and UV/ozone cleaner for 15 min before use in conductance measurements.

5.3.3 Experimental Setup for Imaging and Conductance

The double-chamber cup was used to hold the nanopore support as previously described in Chapter 3. The nanopore sample (Figure 5.1 B) sits on the square inset of the top chamber piece and is sealed into the top chamber using a continuous layer of fast curing Ecoflex Supersoft 5 (Figure 5.1 C).

AFM imaging in liquid was performed with deflection feedback on the nanopore sample in the double-chamber cup. An Ag/AgCl electrode was placed through a port of the liquid cell, and another similar electrode was embedded in the opposite chamber of the double-chamber cup (Figure 5.1 A). The entire AFM base was placed in a Faraday cage on in-house bungee cord-suspended platform for noise isolation. A complete schematic of the experimental setup is shown in Figure 5.1 A.

5.3.4 Lipid Bilayer Preparation

DiPhyPC liposomes were formed by drying lipids dissolved in chloroform in a rotovap. The dried lipids were hydrated with molecular grade H_2O and vortexed. The solutions were then sonicated for 10 min.

Nanopore surfaces were pretreated with a droplet of lipid–hexane solution containing 70 μL of lipid (5 mg/mL) mixed with 100 μL of hexane. Liposomes were deposited over the nanopore and incubated for 2 h at room temperature. Several drops of 1 M KCl, 10 mM Tris, 5 mM $CaCl_2$, pH 8.0, buffer were added to the incubated liposome droplet and incubated for an additional 10 min to transition single-vesicle layers to suspended single planar bilayers across the nanopore [150]. Excess Ca^{2+} and liposomes were rinsed with 1 M KCl electrolyte solution buffered with 10 mM Tris to pH 8.5. The double-chamber cup was set on the scanner head of the AFM. The area containing the nanopore, a 20 $\times$ 20 μm^2 area of 200 nm thick SiO_2, was aligned under the cantilever tip in an optical system.

5.3.5 Simultaneous AFM Imaging of Bilayer and Electrical Recording

Conductance levels and capacitance of the bilayers were recorded using a National Instruments DAC with a custom LabView 8.0 program and the patch-clamp amplifier under applied voltages of $\pm$100 mV. When sufficient sealing of the nanopore was established, the AFM was engaged and, in contact mode, the area of the nanopore covered with bilayers was imaged while simultaneously recording conductance levels. Capacitance measurements were performed by feeding ramp function signals (10 mV amplitude, 10 Hz) across the bilayer. The capacitance of the membrane is proportional to the amplitude of the resulting square wave. All electrical measurements were analyzed with Clampfit 10.2. A digital lowpass Gaussian filter with a 50 Hz cutoff was applied to all data represented. Extraneous 60 Hz noise was eliminated with a digital notch filter centered at 60 Hz with a 9 Hz bandwidth.

5.4 Results

5.4.1 AFM Analysis and Conductance Characterization of Nanopore

Images of the nanopore support were taken periodically throughout the fabrication process by electron microscopy (EM) and AFM. A 20 × 20 μm^2 suspended SiO_2 area was visible in SEM (Figure 5.3 A inset) and in AFM (Figure 5.4 A), enabling for the eventual centered drilling of the nanopore. The AFM height images show a large deformation pattern of the suspended SiO_2 square that is not seen in SEM (Figure 5.4 A). This deformation is due to stress relief following the etching of the underlying Si layer. The center area of this square where the graphene membrane resides appears to have very little deformation in comparison to the edges, sufficient for imaging bilayers. The focused ion beam (FIB)-drilled hole placed in the center of this square is also visible in SEM (Figure 5.3 A), TEM (Figure 5.3 B), and AFM even after deposition of the graphene/Al_2O_3 layer (Figure 5.4 A–B). Complete coverage of the FIB hole with graphene was confirmed in the TEM (Figure 5.3 B) before nanopore drilling (Figure 5.3 C). AFM imaging reveals the nanopore (Figure 5.4 C), which is found by sequentially zooming in on the center of the FIB hole, such as that seen in Figure Ch4F4. With a very sharp AFM tip, the nanopore size can be approximated from the AFM image and compared to the size observed in TEM (Figures 5.3 D, 5.4 C–D, and 5.6). The square shape of the nanopore shown in Figure 5.4 C is likely due to geometry effects of the AFM tip (radius ∼30 nm) and the depth of the pore.

Ion conductance measurements are a good way to probe the pore geometry [150, 151, 166, 171, 173]. Neglecting access resistance for our large pores, pore conductance relates to geometry via the following equation [151, 171]:

$$G = \frac{\pi d_{pore}^2}{4L_{pore}} \left[\left(\mu_K + \mu_{Cl} \right) n_{KCl} e + \mu_K \frac{4\sigma}{d_{pore}} \right]$$

Where G is conductance, dpore is the pore diameter, L_{pore} is the pore cylindrical length, n_{KCl} is the concentration of the buffer, e is elementary charge, σ is the surface charge density in the nanopore, and μ_K and μ_{Cl} are the electrophoretic

mobilities of the two solution ions potassium and chloride. A 1 M KCl buffer was used in the work reported here. The electrophoretic mobilities of potassium and chloride are $\mu_K = 7.616 \times 10^{-8}$ m^2/(V s) and $\mu_{Cl} = 7.909 \times 10^{-8}$ m^2/(V s) at room temperature.(10, 37)

The predicted conductance from the given equation is dependent on pore morphology and surface charge density of the sample. High surface charge density for graphene/Al2O3 layers is considered 200 mC/m^2, and minimum surface charge is 0 mC/m^2 [150, 171]. A range of solid-state nanopores was fabricated with dpore values of 20–50 nm and L_{pore} ∼5 nm. The expected conductance values in this nanopore size range for high and low surface charge density samples would be approximately 1100–6100 and 940–5900 nS, respectively. Open conductance values of individual solid-state nanopores were measured by ramping at 0.4 mV/s over ±10 mV. The conductance of the ∼25 nm diameter nanopore sample, free of bilayer (Figures 5.5 A and 5.6), was measured to be 2765 nS, which falls in the reasonable range of conductance values for 20–50 nm nanopores.

5.4.2 Simultaneous AFM and Electrical Recording of a Suspended Lipid Bilayer

Following the deposition of 1,2-diphytanoyl-sn-glycero-3-phosphocholine (DiPhyPC) bilayers on the nanopore support mounted in the double-chamber cup system, the pore conductance decreased to <10 pS, as measured in the range ±100 mV (Figure 5.5 C, red). The capacitance of the device with the bilayer was measured to be ∼375 pF. Contributing factors to this value may include current passing through the Al_2O_3 layer to the graphene sheet, which increases the capacitive area and the geometry of a thin membrane [141, 173, 181]. However, capacitances in these ranges are frequently utilized for planar lipid bilayer (PLB) recording of ion channels [182]. In other experiments, partial sealing of the same nanopore was observed by conductance value to drop only to ∼0.83 nS (data not shown), indicating an incomplete seal.

The integrity of the fully sealed suspended lipid bilayer, as determined by capacitance and electrical recording, remained stable while engaging the AFM

(Figure 5.7). The interaction force of the AFM was minimized such that it did not interfere with the activity or structure of membrane. The AFM images in Figure 5.7 A–B of the suspended bilayer over the nanopore shows complete coverage. The electrical recording and simultaneously obtained AFM images of the bilayer over the nanopore are shown in Figure 5.7. Increases in noise were observed during the adjustment of the Faraday cage during the electrical recording. Throughout the AFM imaging (>1 h), switching of the voltage bias did not impact the conductance value of the bilayer.

5.5 Discussion

We have developed a nanoscale thin-film support integrated with our newly developed double chamber capable of simultaneous electrical recording and AFM imaging of biological membranes and membrane proteins. The practicality and benefit of this system was demonstrated by structural imaging while measuring the ion-insulating properties of suspended lipid bilayer membranes.

Each step in the fabrication of the nanopore support was chosen with consideration for the ease of fabrication as well as function. A silicon dioxide film on silicon is an ideal material combination to use for the base structure of the nanopore support because of its well-characterized electrical properties, reproducibility, and commercial availability [91, 175, 183]. Silicon dioxide provides an insulating coating to the large area of the substrate, an essential property to isolate the two compartments of the electrical recording setup. FIB offers a fast and easily controlled approach for opening the 1 μm hole in the sample to allow for diffusion of electrolytes through the nanopore. Graphene binds tightly to the SiO_2 upon drying, which secures it as a suspended insulating membrane over the FIB gaping hole. In contrast to the multilayer graphene-based structure described [150], using a single graphene-deposition step allows us to achieve a suspended membrane thickness that is more commensurate with that of a lipid bilayer while still providing good mechanical support. Electrical insulation and structural reinforcement was provided by deposition of 5 nm Al_2O_3 using ALD, which creates a uniform

coating with a minimal increase in membrane thickness [150, 166, 183]. The final graphene/Al_2O_3 membrane surrounding the nanopore is <10 nm. TEM drilling allows positioning the bilayer support on the nanometer scale [142, 175].

Nanopore supports that show a smooth surface in AFM revealed the location and size of the nanopore itself (Figures 5.4 C and 5.6), and, to our knowledge, AFM images of such small nanopores in graphene/Al_2O_3 membranes have not been previously shown. Characterizing the local environment of a solid-state nanopore by AFM could potentially be used in single-molecule studies by functionalizing the AFM tip. Additionally, the high-resolution AFM imaging of a 20 nm nanopore, as in Figure 5.4 C, suggests membrane proteins in a similar size range may be individually probed in future simultaneous structure–conductance studies [152, 29, 158, 159]. Individual ion channels in supported membranes have often been resolved at larger scan sizes [152, 29, 158, 159, 184, 85, 185, 186]. These solid-state nanopores are therefore suitable for the intended application of ion channel studies. With this technology, the structure of suspended bilayers or membrane proteins in suspended bilayers may be explored to achieve a better understanding of their function.

Future work with lipid bilayers and the nanopore substrates will investigate the conductance of membrane proteins. The aim of these efforts will be to resolve individual open and closed channel structures localized in the suspended bilayer and to correlate characteristic channel conductances.

5.6 Conclusion

The use of a defined solid-state single-nanopore support in AFM allows for localized characterization in and around the nanopore. We have used this nanopore support to combine both imaging with AFM and functional mapping with bilayer electrical recording. We show that single solid-state nanopores can be fabricated in graphene reinforced with Al_2O_3. The hierarchy of the sample structure allows for quick and easy location of the single nanopore in AFM. This enables accurate identification of a nanoporous thin film, such as lipid bilayers with embedded ion

channels, when suspended over this nanopore. The presence of suspended bilayers across the electrical recording path was confirmed and characterized through conductance and capacitance measurements (Figure 5.5). Small scan sizes, <1 μm, and repeated stable imaging of the suspended bilayers (Figure 5.7) suggest high-resolution imaging of thin lipid membranes and membrane proteins is possible. Correlated structure and activity information on ion channels obtained using this integrated system will open the door for the study of basic physiological and biological systems as well as for defining the underlying mechanisms of pathophysiology and diseases, including neurodegenerative diseases, drug addiction, biological pathways, and protein structures. The system described here can be applied more broadly to other thin-film-based techniques, including molecular separation, DNA sequencing, and catalysis.

Chapter 5, in full, is a reprint of the material *Connelly L S*, Meckes B*, Larkin J, Gillman A L, Wanunu M, Lal R. Graphene nanopore support system for simultaneous high–resolution AFM imaging and conductance measurements. ACS Applied Materials & Interfaces. 6(7):5290–6.* The dissertation author was the primary author.

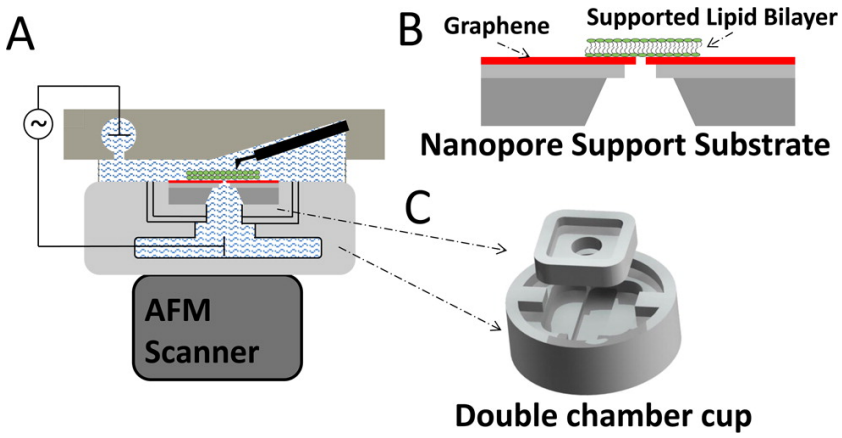

Figure 5.1: **Schematic of the integrated AFM system for imaging and conductance measurements.** **(A)** The nanopore support is glued into the top chamber of the double-chamber cup such that the only liquid path connecting the chambers is through the deposited lipid bilayer (green) over the nanopore. The double-chamber cup is placed on the scanner head, and the liquid cell with mounted cantilever is placed on top of the sample to allow for AFM imaging. Electrodes are connected to the bottom chamber though the double-chamber cup and to the top solution through an open port in the liquid cell for measuring conductance activity. The electrodes are fed to an amplifier and computer for analysis. **(B)** Schematic of the nanopore support (black) with a deposited lipid bilayer (green) suspended over the pore to seal the ionic conductance. **(C)** Schematic image of the double-chamber cup design. The nanopore support from panel B fits into the top removable piece and is set into the bottom piece.

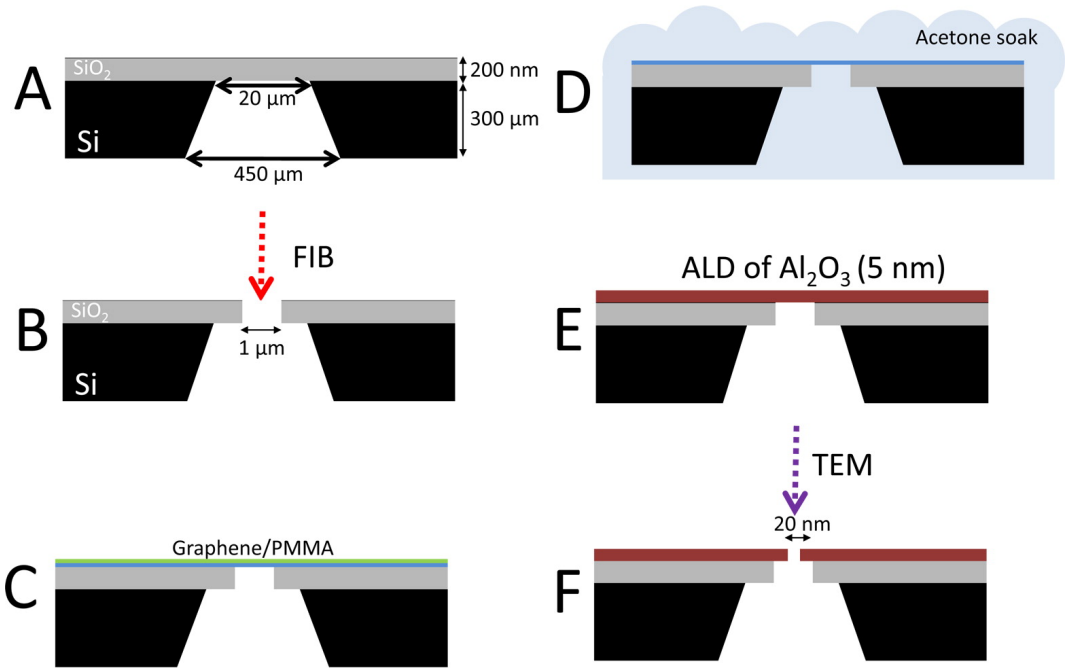

Figure 5.2: **Cross-sectional schematic sequencing of the processing of a solid-state substrate containing a single nanopore.** **(A)** The starting substrate is a 6 mm × 6 mm × 300 μm silicon substrate (black) with a 200 nm SiO_2 layer (gray). A 20 × 20 μm^2 window of suspended SiO_2 is in the center of the substrate. **(B)** A focused ion beam (red) is used to find the center of the 20 × 20 μm^2 SiO_2 window and to drill a 1 μm hole. **(C)** A graphene flake (blue) coated with PMMA (green) floating on the surface of H_2O is placed over the 1 μm FIB hole and allowed to dry. **(D)** Acetone is used to dissolve the PMMA, leaving a graphene sheet suspended over the 1 μm hole. **(E)** Five nanometers of Al_2O_3 (red) is deposited by atomic layer deposition (ALD) over the graphene. **(F)** TEM (purple) is used to drill a single nanopore in the center of the 1 μm hole.

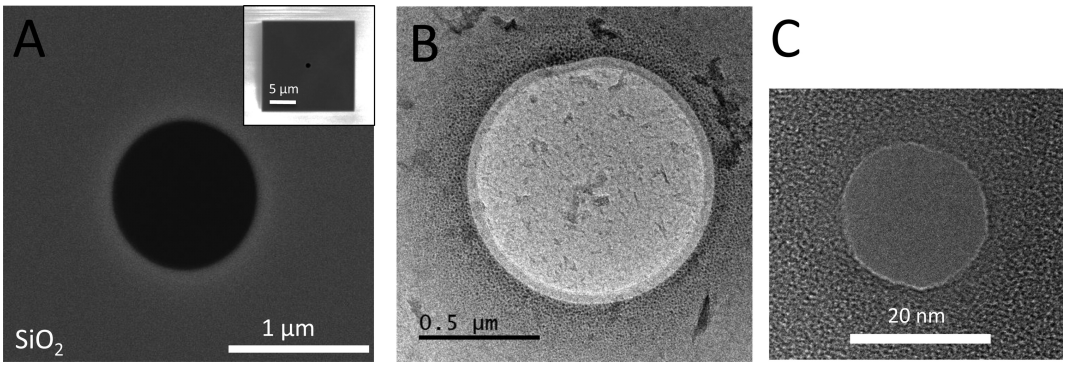

Figure 5.3: **Images of graphene nanopore substrate during processing.** **(A)** Top-view SEM image of the drilled FIB 1 μm hole. Inset is a zoomed-out SEM image of the same hole. The 20×20 μm^2 SiO_2 window is visible in the SEM image. Scale bar = 1 μm. **(B)** TEM image of the drilled FIB 1 μm hole covered with a layer of graphene showing no defects. Thicker regions appear darker. Scale bar = 500 nm. **(C)** TEM image of a single drilled 20 nm pore in the graphene/Al_2O_3 membrane. Scale bar = 20 nm.

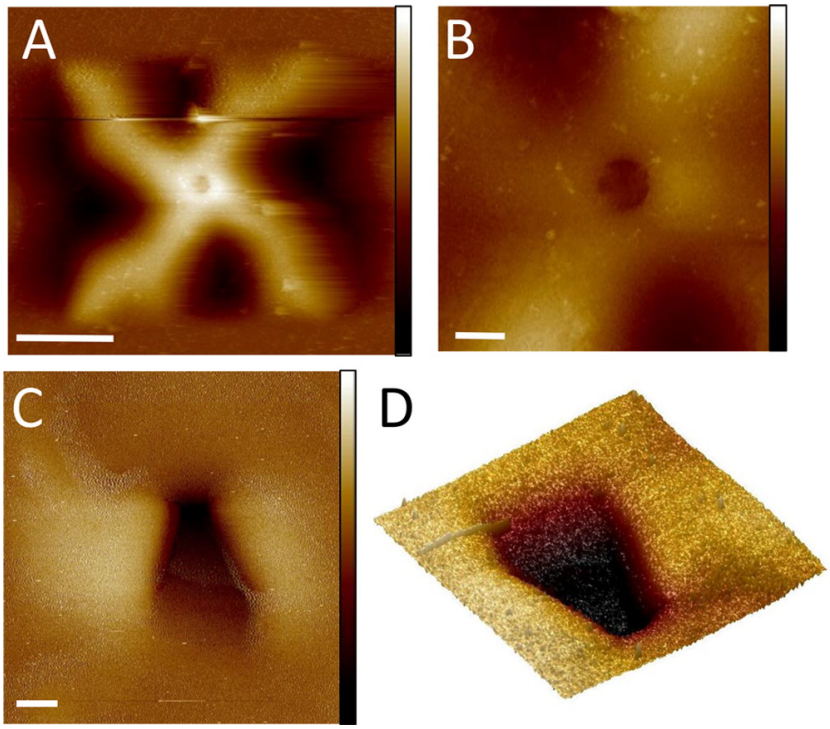

Figure 5.4: **Progressive AFM height images in tapping mode of a complete nanopore support.** **(A)** Image showing the complete 20 × 20 μm^2 SiO_2 area with an X-shaped deformation resulting from stress relief following the etching of the underlying Si layer. The center of the X, where the graphene membrane resides and AFM imaging will occur, shows very little localized deformation. Scale bar = 5 μm, height color scale = 294 nm. **(B)** Image of the FIB hole showing uniform coverage by graphene/Al_2O_3. Scale bar = 1 μm, height color scale = 208 nm. **(C)** Image of a single nanopore drilled in graphene/Al_2O_3. The rectangular shape of the nanopore is an effect of the shape of the tip and imaging into the pore area. Scale bar = 20 nm, height color scale = 17.8 nm. **(D)** Three-dimensional view of the nanopore shown in panel C. Image size is 125 × 122 nm^2.

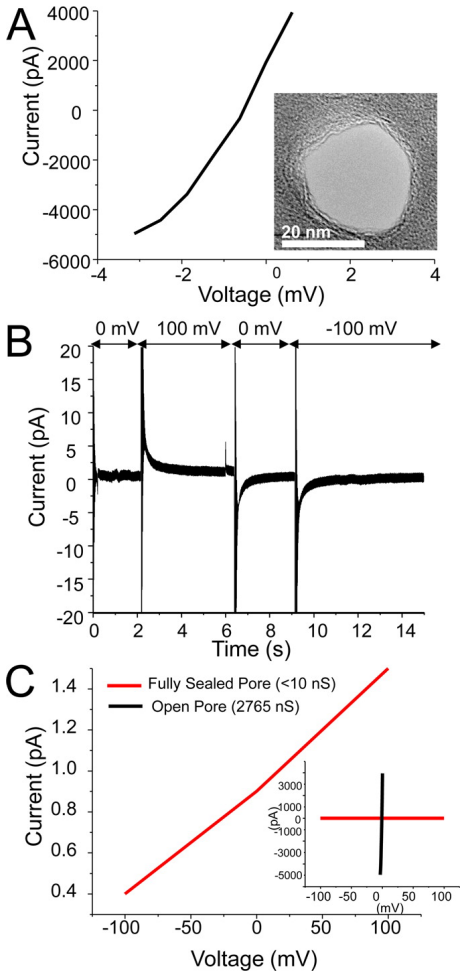

Figure 5.5: **Conductances of graphene nonporous when open and sealed with lipid bilayer. (A)** I–V curve of an open nanopore shown in the inset image measuring ∼25 nm with a conductance of 2765 nS. This nanopore was used in the simultaneous AFM imaging and electrophysiology measurements in panels B and C and Figures 5.6 and 5.7. Scale bar = 20 nm. **(B)** Ionic current recording of DiPhyPC lipid bilayer deposited over the nanopore in 1 M KCl electrolyte solution. The observed conductance was <10 pS. **(C)** I–V curve of the nanopore from panel A after deposition of a DiPhyPC lipid bilayer. The observed conductance was reduced to <10 pS, indicating a full seal of the nanopore by the bilayer. The inset compares the I–V curves of the open nanopore (black) and DiPhyPC bilayer-sealed conductance (red).

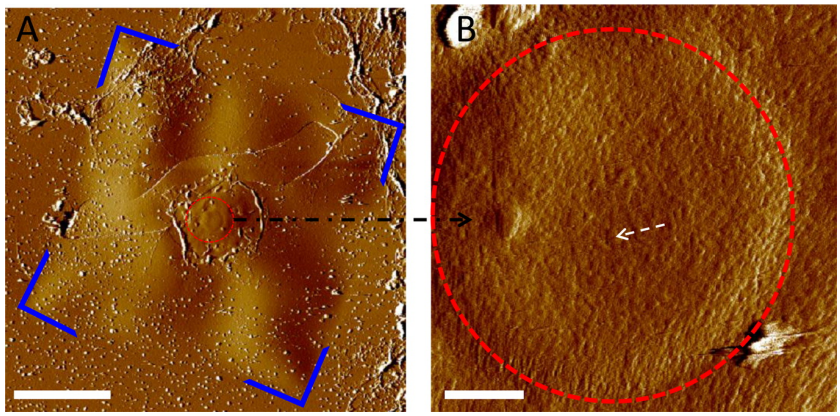

Figure 5.6: **AFM Images of a graphene nanopore covered with lipid bilayer. (A)** AFM deflection image of 20 × 20 μm^2 area containing the nanopore without a deposited bilayer (outlined in blue). The 1 μm area containing the graphene/Al_2O_3 membrane and a single nanopore are observed in the center of the square. The black arrow shows the zoomed view of this area in panel B. Scale bar = 5 μm. **(B)** High-resolution AFM image of the 1 μm area containing the graphene/Al_2O_3 membrane and a single nanopore (outlined in red) with no bilayer present. The white arrow indicates the location of the nanopore. Scale bar = 250 nm.

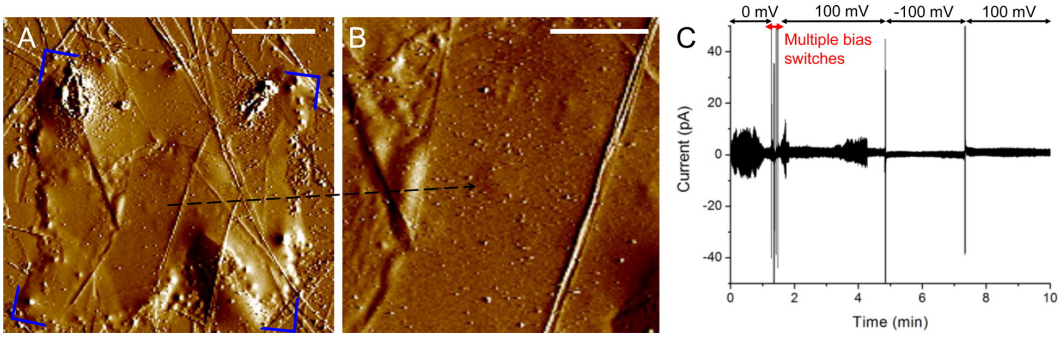

Figure 5.7: **Simultaneous AFM imaging and electrical recording of a nanopore covered with a lipid bilayer. (A)** AFM deflection image of square area containing the nanopore after the deposition of the DiPhyPC bilayer (corners highlighted blue) obtained while simultaneously recording ionic conductance. AFM image corresponds to the same area shown in Figure 5.6 A. The 1 μm area containing the graphene/Al_2O_3 membrane and a single nanopore is observed in the center of the square. The black arrow points to the zoomed view of this area in panel B. Scale bar = 5 μm. **(B)** High-resolution AFM image of the 1 μm area containing the graphene/Al_2O_3 membrane and a single nanopore. Scale bar = 2 μm. **(C)** Ionic current recording trace obtained while AFM imaging. The initial noise increases at the beginning of the recording and during the 2–4 min time of recording correlate to physical interactions with the system (AFM base and Faraday cage door) and subside upon establishment of physical isolation of the entire system. Applied voltages of $\pm$100 mV were applied to confirm pore sealing.

Chapter 6

Electrical Recording of Ion Channels in Lipid Bilayers Suspended over Nanopores in Graphene Membranes

6.1 Abstract

Understanding the behavior of individual macromolecules through their structure and corresponding activity is important for improving developments in health care, energy sources, and chemical synthesis. The structure–activity relationship of ion channels, a class of biomacromolecules, defines a wide array of biological functions that include cell communication and signaling, nutrient and energy recycling, and ionic homeostasis. For example, the opening and closing conformations of ion channels regulate ionic flow in and out of cells, which in turn mediates important physiological processes that include cellular homeostasis and signal propagation at the cellular, tissue and organ level. Connexin hemichannels, a type of ion channel, are known to facilitate cell–surround responses, but their physiological role is poorly defined. Thus, enabling technologies for simultaneous recording of electrical activity and high resolution imaging of protein structures are necessary for deeper understanding of protein structure–activity relationships in health and disease. Here, the two–chamber/nanopore support system for simulta-

neous imaging and electrical recording of macromolecules is applied to the study of connexin26 hemichannels in purified membrane fragments and reconstituted into liposomes. Purified Sf9 membrane fragments were deposited over a 1 μm pore and the conductance was modulated via Zn^{2+} before being successfully removed via force dissection. Single–channel activity was recorded for Cx26 with an observed conductance of 244 $\pm$ 24 pS when suspended over a nanopore.

6.2 Introduction

Understanding the relationship between the structure and activity of biological macromolecules is critical to developing therapeutic agents and creating bio-electronic sensors and devices. The structure of biomacromolecules, such as ion channels and receptors, have been realized with various high-resolution imaging techniques, including x-ray crystallography, electron microscopy, and atomic force microscopy (AFM). Among these techniques, AFM provides the most versatile platform for imaging of protein structures in real-time as well as their conformational changes that can be induced by agonists [187, 188, 21, 69, 23, 189, 190]. AFM has been successfully used to image the surface structures of ion channels and receptors embedded in lipid membranes as well as changes in their conformations, such as the opening and closing of ion channels [68, 21, 23].

The electrical activity of ion channels is traditionally recorded using electrophysiological techniques, such as patch-clamp and bilayer lipid membranes recording. However, electrophysiology does not have the capacity for imaging. Thus, structural imaging and activity recording are obtained independently, and the data must be correlated thereafter, not in real-time. Therefore, simultaneously imaging the dynamic high-resolution structures, while recording the electrical activity will enhance understanding of the structure–activity relationship of ion channels and receptors that determine overall health and well being. Chapters 2 and 5 describe the development of a two–chamber system and graphene nanopore support that enable simultaneous imaging of structure and function with AFM. Here, we describe the application of these two systems for the imaging and electrical recording

of connexin26 hemichannels, an ion channel protein, that have been purified in membrane fragments as well as in detergent stabilized confirmations that are later reconstituted into liposomes.

Gap junctions (GJs) are an important class of ion channel proteins that couple two cells together for cell–cell communication and signaling. GJs are composed of two hexameric connexin hemichannels that dock together on apposing cells to form a channel between the cells. The behavior of GJs have been well documented with regards to their response to various stimuli [191, 192, 193] . However, undocked connexin hexameric channels, termed hemichannels, have limited imaging and physiological characterization as they are difficult to identify in cellular structures due to the lack of identifiable assemblies, though there is evidence suggesting they play a functional role in cell behavior [65, 56, 63, 64]. Hemichannels have been demonstrated to respond to a variety of stimuli, including pH and ionic concentration [21, 69, 68].

Connexin26 (Cx26), the smallest of the connexin proteins, plays an important physiological role in cochlear cell coupling thus mutations in the protein can result in deafness while other mutations lead to a thickening of skin in the hands and feet [127, 83, 194, 195]. Reduced function of the Cx26 gap junction channels has been demonstrated to be a result of the mutations leading to these syndromes [86, 85, 117]. Increased activity with some mutations leading to deafness has also been reported for Cx26 hemichannels [87]. Activity of Cx26 hemichannels has been observed when reconstituted into liposomes or expressed in oocytes membranes presenting a model system for study of the structure and activity [66, 117]. However, the electrical properties and functional activity of these channels are poorly understood with multiple and widely varying conducting states reported [81, 82]

Here, the structure and electrical activity of connexin hemichannels were studied using AFM. Connexin hemichannels were deposited over a micro– and nano–pore substrate and the surface structures were imaged using AFM. The electrical activity of a purified membrane fragment was explored with observed blocking of conductance with Zn^{2+} addition. Force dissection with AFM of the

membrane resulted in successful removal of the membrane and increased observed conductance. The surfaces of the nanopore support membranes were also modified to improve liposomal fusion resulting in bilayer formation. This was accomplished by introducing a SiO_2 layer over Al_2O_3, which has higher surface interaction energy, which allows the liposomes to open and fuse to the surface. The activity of a single Cx26 hemichannel reconstituted in a lipid bilayer deposited over the nanopore was successfully recorded using the nanopore membrane with an observed conductance of 245 $\pm$ 24 pS.

6.3 Materials and Methods

6.3.1 Micropore Membrane Fabrication

A detailed protocol for micropore membrane fabrication was previously described in chapter 4. Briefly, silicon dioxide membranes (SiO_2) were purchased from AppNano (Mountain View, CA). These membranes contain a membrane window consisting of a thin (200 nm) SiO_2 membrane window (20 μm $\times$ 20 μm) suspended over a 300 μm thick piece of silicon. A 1 μm hole was drilled into the center of the membrane window with a focused ion beam (FEI Dualbeam) using a current of 30 nA.

6.3.2 Nanopore membrane fabrication

Following the fabrication of a micropore, a monolayer piece of CVD grown graphene on copper foil (Graphene Supermarket, Caverton, NY) was coated with polymethyl methacrylate (PMMA A9, AZ). The monolayer of graphene on the backside was removed with oxygen plasma (200 mT, 200 W for 30 s) and the copper backing was removed in copper etchant diluted 1:10 in water overnight. The graphene–PMMA substrate was deposited over the membrane including the1 μm hole and allowed to dry on a sloped surface for the graphene to attach to the SiO_2 surface. The PMMA was removed from the graphene in acetone overnight. Atomic layer deposition (ALD) of $\sim$3 nm of Al_2O_3 was deposited by a Beneq

TFS200 atomic layer deposition system utilizing a low temperature deposition (110 °C) with TMA and H_2O precursors in nitrogen gas. SiO_2 (∼2 nm) was then deposited with ALD over the Al_2O_3 layer with SAM24 and ozone precursors at 250 °C. A transmission electron microscope (TEM) (JEOL 2010FEG, Japan) operating in bright-field imaging mode was used for drilling through the graphene-Al_2O_3-SiO_2 membrane layer.

6.3.3 Protein Expression and Purification

The methods for protein expression via a baculovirus expression system in *Spodoptera frugiperda* (Sf9) cells and purification were previously described in chapter 4. Details on the expression system and techniques for connexin expression can be found in detail in [126, 128, 85, 129]. The affinity purification scheme utilizing hexahistidine tags can be found reported in [78, 126, 128, 85, 130].

6.3.4 Hemichannel Reconstitution

1,2-Dioleoyl-sn-glycero-3-phosphatidylcholine (DOPC) lipids (Avanti Polar Lipids, Alabaster, AL) (5 mg/mL) dissolved in chloroform were dried in a rotovap. The dried lipids were hydrated in an imaging buffer (10 mM HEPES, 150 mM KCl, 2 mM $MgCl_2$, pH 7.4)(final DOPC concentration of 0.8 mg/mL) with n-octyl-β-d-glucoside (OG) (5 mg/mL) and briefly mixed with a vortex. The solution was bath sonicated for 10-20 min. Purified Cx26-V5-His6 hemichannels (NCBI Reference Sequence: NM_001004099.1) in elution buffer were added at 1:200 to the liposomes. The mixture was sonicated for 2 min and then gently mixed for 1 h at 4 °C. The detergent was removed to create proteoliposomes by treatment with Biobeads (Bio-Rad Laboratories, Hercules, CA) (0.1 g/mL) twice for 2 h or overnight at 4 °C.

6.3.5 Deposition of Ion Channels on Support Membranes

The graphene–based nanopore membrane was UV/ozone plasma treated for 20-60 min prior to deposition of Cx26 containing proteoliposomes. Following

plasma treatment, the membrane was attached to the two–chamber system with a silicone rubber. The backside of the membrane was hydrated with isopropanol and rinsed 3× with imaging buffer. The proteoliposomes were deposited on the surface and incubated for 30-60 min. The membrane is then rinsed with imaging buffer to remove unattached liposomes.

6.3.6 Experimental Setup for Imaging and Conductance

The double–chamber system described in chapters 2 and 5 was used to hold the nanopore membrane support by mounting it with silicone rubber. The conductance was recording using two Ag/AgCl electrodes with a patch clamp amplifier. The two–chamber system was placed on a multimode IV AFM (Bruker, Santa Barbara, CA) for imaging. The entire AFM system was placed in a homemade Faraday cage for electrical shielding and suspended from a bungee chord–suspended platform to dampen any vibrational noise. The conductance was recorded with a custom LabView 8.0 program and a National Instruments digital-to-analog converter (Austin, TX). Electrical analysis was performed with Clampfit 10.2.

6.3.7 Data Analysis of Single–Channel Activity

Leakage current in single–channel recording was corrected using a cubic spline baseline subtraction (OriginPro 2015, Northhampton, MA). A histogram with a bin size of 0.2 pA was used to generate histograms, which were subsequently fit to Gaussian distributions to determine the populating mean and standard deviation. All values are reported as mean ± standard deviation.

6.4 Results

6.4.1 Imaging and electrical recording of Sf9 membrane patch

Cx26 hemichannels embedded in a purified Sf9 membrane were deposited over a microporous membrane. The electrical activity of the deposited membrane

was recorded while simultaneously imaging the structure of the lipid bilayers. Large currents were observed in the deposited membrane, which were likely due to the large pore size utilized for recording. AFM imaging of purified Sf9 hemiplaques showed high densities of Cx26 hemichannels in chapter 5, which likely accounted for the increased currents due to a large number of channels present over a micropore. The apparent conductivity of the channels was reduced and nearly eliminated with injection of Zn^{2+}, a non–specific inhibitor of connexin activity, containing buffer into the system (Figure 6.1 C). This suggests that there was a purified membrane patch containing Cx26 channels present over the pore.

AFM imaging and force dissection further confirmed the presence of a bilayer over the pore. AFM imaging of the pore area showed that the pore was completely covered by bilayer structures (Figure 6.1 A,B). These structures were mechanically flexible in the pore area as can be seen by the instability of AFM imaging over the pore. Increasing the applied force allowed for removal of the lipid bilayer membrane by selectively scraping away the lipid membrane from the surface (Figure 6.2 A,B). The bilayer was subsequently disrupted resulting in a drastic and rapid increase in conductance in the electrical recording (Figure 6.2 C). This provides further confirmation that the conductance was indeed due to the presence of a bilayer. The height of some of the bilayer structures was measured following force dissection of the membrane. The step height was found to be $\sim$6 nm, which is consistent with the bilayer heights reported in chapter 4 (Figure 6.2 D).

6.4.2 Electrical Recording of a single Connexin26 Hemichannels

Detergent stabilized Cx26 hemichannels purified from Sf9 cells were reconstituted in DOPC liposomes, and then deposited on SiO_2 coated graphene membranes, which had been surface activated with UV/ozone treatment (Figure 6.3). Liposomes spontaneously formed bilayers on the surface due to a favorable energetic interaction between the lipids and surface. Following deposition of the lipids, the electrical activity of Cx26 HCs was recorded with the two–chamber system. A repeated single step conductance of the same intensity was observed, which are

typically interpreted as a single ion channel opening and closing (Figure 6.4). A leakage current was also detected in this recording, which could be due to a crack in the graphene membrane or incomplete sealing of the pore (Figure 6.4).

The current was baseline corrected for the region with a bias of -85 mV to allow for a better measurements of the conductance using a spline interpolation method (Figure 6.5 A). A histogram was generated for the conductances in the baseline corrected data. A gaussian distribution was fit to the two gaussian peaks observed in the histogram and the average current was determined to be -20.9 pA $\pm$ 2.0 for the open conformation and 0.1 $\pm$ 2.3 pA for the closed. This is equivalent to a conductance of 244 $\pm$ 24 pS for an open channel (Figure 6.5 B), which is consistent with literature values that have been reported [82].

6.5 Discussion

Nanopore fabrication steps were modified to improve the formation of bilayers over the nanopore surface. The previous design utilized Al_2O_3 as the insulation for the graphene nanopore, which is not conducive for the spontaneous opening of liposomes to form lipid bilayers [196, 197]. Previous work has shown that bilayer formation is indeed possible, but requires special treatment of the liposomes to induce bursting through high osmotic pressures and adhesion to the surface [179]. This includes plasma treatment of the surface to activate it by inducing the formation of hydroxyl groups on the surface making the surface hydrophilic as opposed to hydrophobic. Liposomes are more conducive to spontaneous opening when formed in a pure water environment and can be induced to form bilayers by adding $CaCl_2$ to increase salinity [179]. However, this is not ideal for proteoliposomes, which contain proteins that can be affected by high salt concentrations and cannot be reconstituted in a pure water environment. Al_2O_3 is typically used with graphene as its growth has been shown to occur spontaneously and uniformly with low temperature ($<$130 °C) ALD, which makes it an attractive for coating graphene [198]. In our modified approach, a SiO_2 layer was deposited via ALD over the Al_2O_3 to promote improved bilayer formation [199].

Blocking of hemichannels has been observed through Ca^{2+}, pH, Zn^{2+}, and several non-specific blockers, such as octanol [68, 21, 69, 200, 84]. In this work, Zn^{2+} was utilized, which is a non-specific blocker of hemichannels, but has been shown to have a significant effect when utilized in concentrations of 10 mM [84]. Zn^{2+} is known to be a membrane stabilizer and blocker of a multitude of other channels, which could account for some of the decrease in observed current [201, 202]. Future work should explore the affect that Ca^{2+} has on the activity of the channels as it is known to affect the structure of hemichannels when present at physiological levels (<2 mM) [21].

Though we have observed the activity of a single Cx26 hemichannel, we have yet to successfully image a single-channel structure over a nanopore. This has been prohibited by instability in the system. However, future improvements to the membrane should reduce the surface roughness that affects the image quality. Also, the hexahistadine tags used in protein purification could be used to enhance imaging through the use of nickel nanoparticles that recognize this sequence, which would effectively increase the size of the subunits during imaging. The conductances reported here for a single hemichannels are similar to reported values for a higher conductance state (200-400 pS). However, lower conductance states has been reported [117]. This could be due the clustering behavior of the proteins, which can modulate the activity of the channels, or due to the presence of different confirmations/modulators that result in different conductances [55]. Future work should explore the change in hemichannel assembly architecture and/or conformation that result in different conductance states. Despite this challenge, the use of a nanopore for imaging and electrical activity recording presents a promising pathway to structure–function imaging.

Chapter 6 is in part a publication in preparation with *Meckes B, Connelly L C, Ambrosi C, Waduge P, Wanunu M, Sosinsky G S, Lal R.* The dissertation author is the primary author.

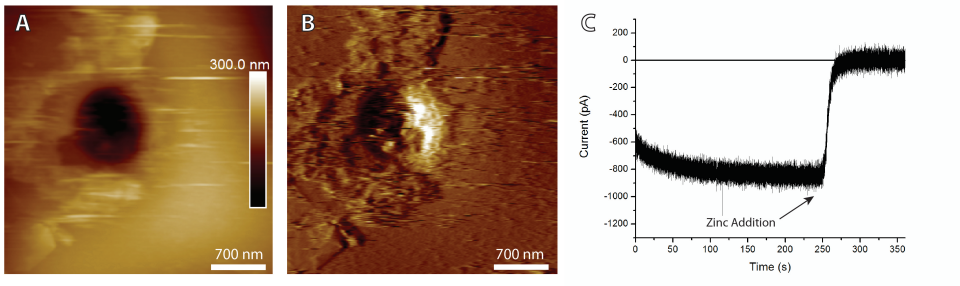

Figure 6.1: **AFM imaging and electrical recording of a purified membrane patch containing Cx26.** **(A–B)** A height mode **(A)** and deflection **(B)** image of a micropore coated with purified Sf9 membrane fragments containing Cx26. **(C)** Electrical recording of the membranes taken simultaneously during imaging. Zn^{2+} blocking is utilized to prevent activity of ion channels in the membrane.

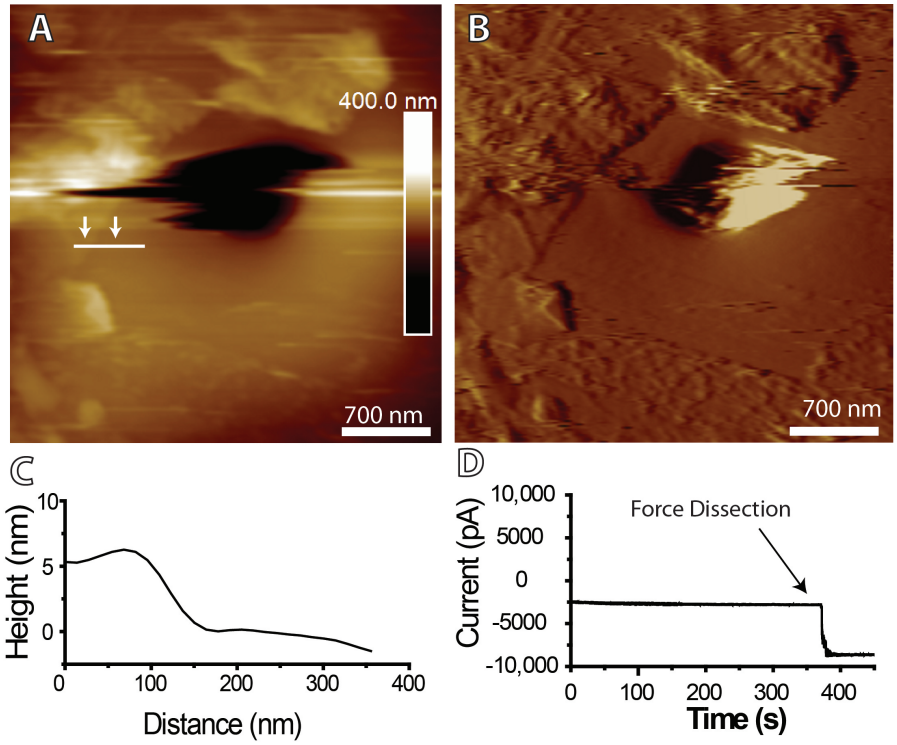

Figure 6.2: **Force removal of a membrane patch suspended over a micropore. (A–B)**A Height mode **(A)** and deflection **(B)** image of a micropore after the lipid bilayer membrane has been removed. bf (C) The step height of the force dissected membrane (Denoted by the white line in **(A)**) is shown and measures 6 nm. **(D)** The conductance jumps drastically as the membrane is force dissected off the surface.

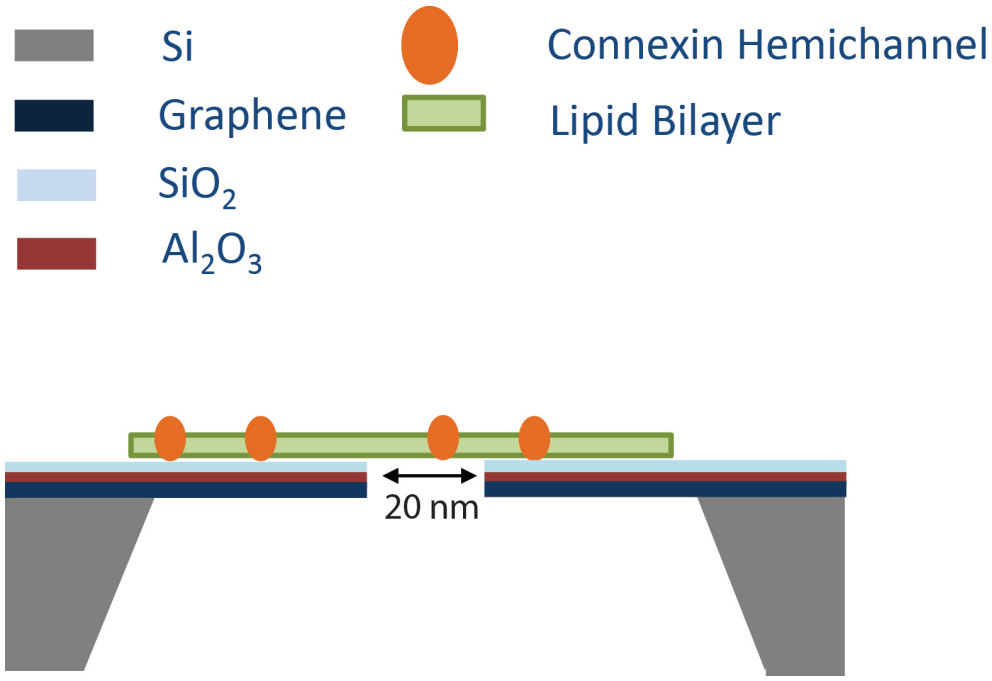

Figure 6.3: **Schematic of the experimental setup for Cx26 recording.**

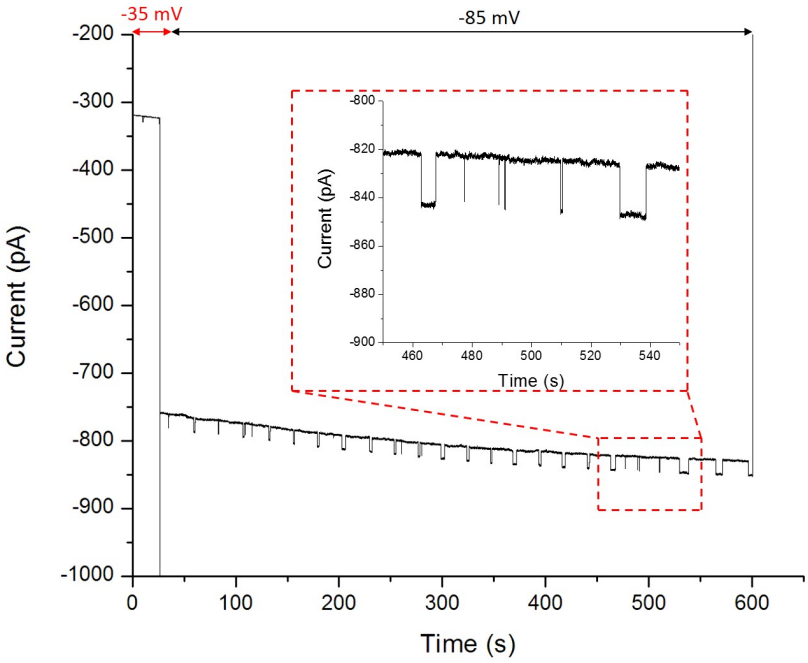

Figure 6.4: **Electrical recording of reconstituted Cx26 deposited over a nanopore in graphene.**

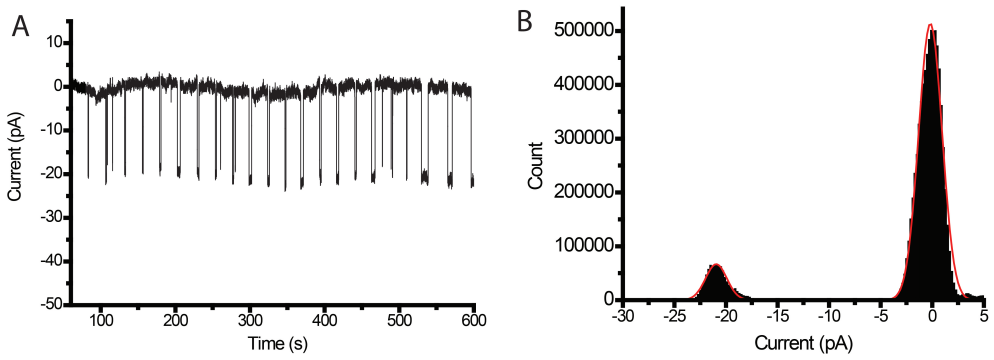

Figure 6.5: **Baseline corrected conductance for a Cx26 hemichannel. (A)** The baseline corrected current trace for a single channel is shown. **(B)** A histogram of the current recorded for a Cx26 hemichannel recorded over a nanopore. A gaussian fit of the two populations of currents (open/closed) was applied (red line). An open state conductance of 245 $\pm$ 24 pS was calculated.

Chapter 7

Design and Fabrication of Scanning Ion Conductance Microscopy Array

7.1 Abstract

The hierarchical relationship between proteins, cells, and tissues in biological systems is defined by cooperative and coordinated interactions that span across the nano-to-macroscale. In particular, the nanoscale activity of ion channels and receptors is defined by cooperative behavior that results in coordinated signal transduction and stimuli responses that extend across cells and tissues. Understanding this complex relationship requires development of technology capable of measuring multiple events simultaneously at the nanoscale. AFM and SICM are capable of imaging nanoscale behavior in real-time, but are limited to imaging of a single area. Here, scanning probe microscopy-based technology is developed for high–resolution and –throughput imaging through the development of a cantilever array for multipoint imaging of structures. Silicon nitride cantilevers with conducting platinum tips were fabricated with a designed stiffness of 0.5 N/m. To create an independent cantilever array, the design implements the capacity for self–actuation and –sensing via ZnO piezoelectric films to allow each cantilever to have independent feedback control and imaging.

7.2 Introduction

The development of novel high–speed and –throughput nanotechnology for lithography, computational memory storage, and biological imaging techniques requires tools that enable nanometer resolution structural imaging and manipulation. Atomic force microscopy (AFM) and scanning ion conductance microscopy (SICM) have the potential to improve these areas through parallelization of the cantilever probes. This requires the implementation of independent actuation and sensing of individual cantilevers within the array. The development of cantilever-based scanning probe microscopy arrays for AFM have been pursued utilizing a variety of methods for actuating the cantilevers through thermal and piezoelectric methods along with unique sensing configurations [203, 204, 205, 206, 207]. Many of these approaches focused on developing novel lithographies or creating techniques for high throughput imaging of solid state devices, but less for biological applications [208, 209, 210, 211, 212].

Imaging of biological systems with integrated cantilevers presents several unique challenges, such as shielding of the electrical components from saline fluids while also maintaining soft forces to prevent disruption of membranes and extracellular matrix proteins. One way to overcome this issue is to use SICM, which, unlike AFM, does not rely upon a physical interaction between the cantilever tip and the surface, providing a non-destructive imaging mode [3]. Instead, it utilizes the localized ionic current measurements, which are dependent on the distance from the probe surface to recording tip. Past SICM arrays that have been developed do not possess self-actuation capabilities for addressing each cantilever independently [213]. This limits the imaging capabilities to only surfaces that are nearly atomically flat.

The implementation of self–sensing and actuation on the cantilever can improve the performance during imaging, particularly when operating in tapping mode. Integration of self–actuation on the cantilever tip can remove many of the erroneous resonant peaks present from mechanical stimulation in fluid, which also vibrates the entire cantilever holding apparatus [214, 215, 206]. Improved imaging speeds and stability have been achieved with self–actuating cantilever [26]. Among

the two most common approaches to multicantilever actuation, piezoelectric provides the most accurate means to control the z position. The other most commonly used method, thermal actuation, relies on passive cooling processes, which can slow down imaging. However, piezoelectric actuation is a fully active process, which can overcome this limitation. However, in fluid systems, it has proven difficult to prevent disruption of the piezoactuator from liquid perturbation.

Here, we report the design and fabrication of a multi-cantilever array for SICM imaging with self-sensing and actuation capabilities. Silicon nitride cantilevers with conducting lines were fabricated with piezoelectric ZnO films for independent actuation of the probe. The sputter pressure for the ZnO film growth was examined to determine the best growth condition for the actuator, which was 7 mT. Conducting tips were integrated into the cantilevers for detecting the distance between the sample and probe in a saline environment.

7.3 Materials and Methods

7.3.1 Fabrication of Cantilever Array

Figure 7.1 shows the fabrication scheme for the cantilevers. An intrinsic <100> silicon wafer (7.1 A) (Virginia Semiconductor, Manassas VA) was coated with silicon nitride (SiN_x) ($\sim$1 μm) using low stress, low pressure chemical vapor deposition. The wafer was subsequently patterned with photolithography and dry etched (Oxford P80, Oxford Instruments, Oxfordshire, UK) to shape the cantilever on the frontside of the wafer. The dimensions of the cantilever structure was 350 μm in length and 100 μm in width (Figure 7.1 B). The backside of the wafer was also dry etched to produce release windows for etching of the silicon in the final step. Next, SiO_2 was deposited on the frontside at 4.5 μm thickness with plasma enhanced chemical vapor deposition (PECVD) (Oxford Instruments, Oxfordshire, UK). The cantilever tip was patterned with photoresist in conjunction with an adhesion promoter, hexamethyldisilazane (HDMS), shape the tip during etching (Figure 7.1 C). The wafer was etched in 6:1 buffered oxide etch (NH_4F:HF) for 15 min (Figure 7.1 D). Next, a thin layer of platinum (150 nm) with a titanium adhe-

sion layer (∼5 nm) was deposited on the cantilever via direct current (DC) plasma sputtering at 2.5 mT Ar (Denton Discovery 18, Denton Vacuum, Moorestown, NJ) and patterned through lift–off. This layer serves as a conducting line for electrical recording and SICM imaging (Figure 7.1 E). To prevent fluid from accessing the electrical recording line in undesirable locations, a layer of SiN_x was deposited with PECVD and subsequently patterned through dry etching (Figure 7.1 F).

7.3.2 Actuator Fabrication

The actuator was implemented on the cantilever by first depositing 5 nm of chrome and then gold (250 nm) as the base electrode with a DC sputtering system (AJA, Scituate, MA) and then patterned via lift–off. Next, a layer of zinc oxide (ZnO) was deposited via radio frequency (RF) sputter deposition (AJA, Scituate, MA) using a ZnO target. The conditions where 95% argon with 5% oxygen gas at 10 sccm flow at 100 W and 7 mT (Figure 7.1 G). Following deposition, the films were annealed in nitrogen gas for 10 min at 350 °C followed by 5 mins at 400 °C to promote the growth of ZnO crystals in the preferred (002) orientation for piezoelectricity. The ZnO film was etched in 1:1:50 phosphoric acid:acetic acid:water for ∼10 s. The top electrode was deposited in the same fashion as the bottom with a titanium adhesion layer in place of chrome. The actuators were then insulated from fluid with PECVD SiN_x (150 nm), which was then patterned with dry etching (Figure 7.1 H).

7.3.3 Cantilever Release

The frontside of the cantilever was coated using an Apiezon wax (Manchester, UK). The backside was etched with 20% KOH at 75 °C until only a thin section of silicon remained (Figure 7.2). The polymer protective coating was removed and the final release was performed with xenon difluoride (XeF_2) dry etching (Xactix, Pittsburgh, PA) (Figure 7.1 I).

7.3.4 Integration with AFM

A custom printed circuit board was designed with Altium (La Jolla, CA) for intergration with the AFM (Figure 7.3). This was integrated with a custom AFM cantilever holder to be utilized with a Multimode IV or V system (Bruker, Santa Barbara, CA).

7.3.5 Characterization of ZnO FIlms

ZnO films were grown using RF sputter deposition (AJA, Scituate, MA) with a ZnO target. The films were grown under 95% Ar and 5% O_2 atomosphere with a flow rate of 10 sccm. The pressures used were 2, 5, 7, and 10 mT on a silicon nitride substrate with an annealing temperature of 500 °C for 15 min. AFM images of films were captured with a Multimode V with a scan rate of 1 Hz in peak force tapping mode. X-ray diffraction was performed on samples sputtered at 7 mT and 10 mT on gold and silicon nitride substrates. These samples were annealed for 10 min at 350 °C and 5 min at 400 °C. X-ray diffraction was performed with Bruker D8 Discover (Madison, WI) with 2θ values from 13 to 95 degrees.

7.4 Results

7.4.1 Probe Fabrication

Images of the fabricated structures were captured with light microscopy. The structures that form the bulk of the cantilever design are shown (Figure 7.4). The dimensions of the cantilever are 100 μm wide, 1.4 μm thick, and 350 μm long. The stiffness (k) of the cantilever can be estimated based on these parameters using Eulerian beam theory.

$$k = \frac{Ewt^3}{4l^3}$$

E is the Young's modulus of the material. w, t, and l are the width, thickness, and length of the cantilever respectively. The estimated stiffness was ∼0.5 N/m based on the Young's modulus of silicon nitride, the main material utilized in the design.

However, this may be an underestimate of the actual stiffness as the cantilever is made up of a complex multilayer system which includes metallic and other ceramic materials.

7.4.2 ZnO Film Growth

RF sputtering of ZnO films was performed at multiple conditions to examine the crystal growth of the ZnO films. ZnO crystals with piezoelectric activity were preferentially grown in the Wurtzite (002) crystal plane. This plane is also the most energetically preferred orientation for sputter deposition growth of ZnO. However, the crystal growth quality is affected by a multitude of factors including the temperature, distance to the sputtering target, rotation, pressure, flow rate, gas composition, annealing temperature, machine, and deposition time [216, 217, 218, 219, 220, 71]. Different sputter pressures were examined including: 2 mT, 5 mT, 7 mT, and 10 mT. Higher pressures showed a positive correlation with increasing grain size at room temperature. AFM images were taken of the samples sputtered under these conditions (Figure 7.5). A sample sputtered at lower pressures, 2 mT, showed formation of amorphous structures (Figure 7.5 A). Poor crystal formation was also observed in the sample sputtered at 5 mT (Figure 7.5 B). Higher pressures, 7 mT and 10 mT, showed improved crystal formation with hexagonal geometry typical of (002) crystal formation (Figure 7.5 C–D). Larger crystals were observed at 7 mT sputter pressure compared to 10 mT.

Films deposited at 7 mT and 10 mT were further characterized with x-ray diffraction. Films grown on gold substrates showed stronger diffraction intensities at the characteristic 2θ angles for ZnO (Figure 7.6), which indicates preferred crystal growth compared to amorphous silicon nitride. Highly oriented piezoelectrically active ZnO crystals favor the (002) Wurtzite orientation, which is when the hexagonal face is perpindicular to the surface and is observed 34.5 degree 2θ angle. The strongest peak is observed under 7 mT, further confirming this as the best condition. Weaker peaks are detected for some of the other crystal orientations indicating that some crystals are not oriented ideally (Figure 7.6).

7.5 Discussion

The design of this scanning probe microscopy array allows for high-resolution multipoint imaging of structure and function. The fabrication of this array has been described in detail though more developing and troubleshooting is needed to realize a fully functional system. The success of this system will be dependent on the implementation of self-actuation, which ideally should occur with highly oriented ZnO films resulting in high restivities ($> 10^6$ Ω·cm) [221]. Improvements can be made by attempting a multi–step deposition technique, which utilizes a combination of sputter temperatures to deposit films with an improved piezoelectric response [222]. Low temperature seed layers along with subsequent high temperature steps may reduce the resistivity of the film and improve the piezoelectric response [222].

The system presented in this chapter is designed for parallel SICM imaging utilizing the conducting tips detection and positionng. To enable multipoint AFM imaging, a suitable deflection detection scheme for the cantilevers is necessary. Current research is on the development of novel detection schemes that are low noise. This effort is focused on the instrumentation of the AFM as opposed to microfabrication of cantilevers with integrated detection. When utilized with the array designed in this chapter, independent parallel AFM imaging will be realized.

Further testing on the fabricated devices will fully characterize the cantilever probes along with their resonant frequency and stiffness. The steps presented in this chapter outline the methods for successful fabrication of a SICM cantilever array.

Chapter 7 is in part a publication in preparation with *Meckes B, Yang Q, and Lal R.* The dissertation author was the primary author.

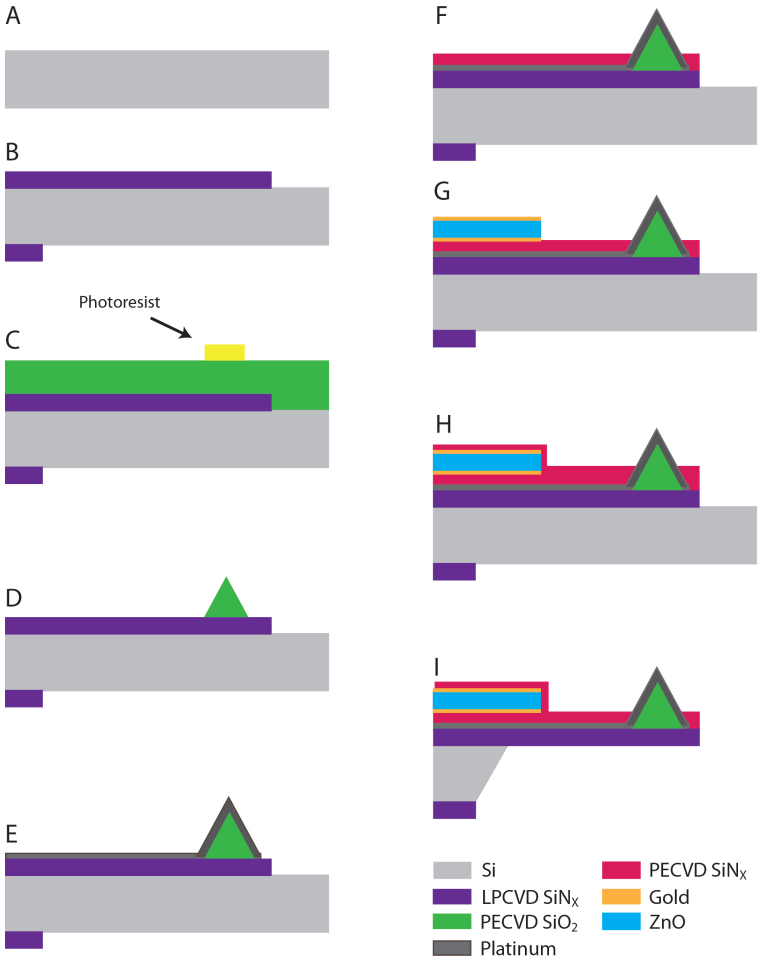

Figure 7.1: **Summary of microfabrication steps for the cantilever array**. **(A)** A piece of <100> silicon that is 500 μm thick. **(B)** Low stress silicon nitride is deposited with LPCVD and patterned on the frontside and backside with dry etching. **(C)** SiO_2 is deposited via PECVD and masked with photoresist. **(D)** The tip is etched with BOE and the photoresist is removed. **(E)** Platinum with a thin titanium adhesion layer is sputter deposited to make each cantilever conducting. **(F)** PECVD silicon nitride is deposited and patterned to insulate the platinum. **(G)** A piezostack consisting of gold upper and lower electrodes with chrome and titanium adhesion layers, respectively. A RF sputtered ZnO film is grown on the lower electrode. **(H)** PECVD silicon nitride was used to insulate the piezostack from fluid. **(I)** The cantilever was etched with KOH and XeF_2

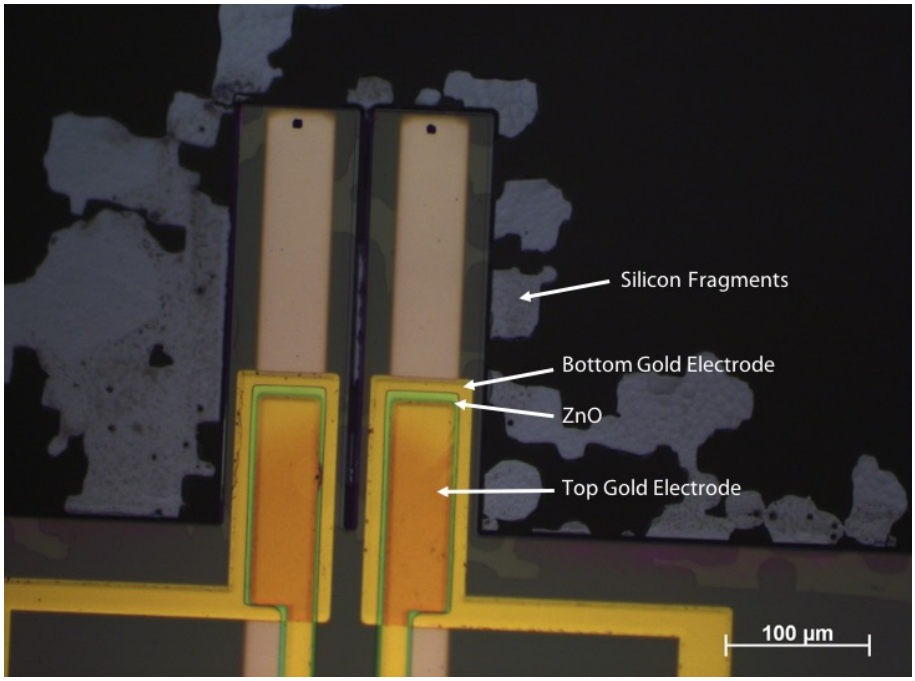

Figure 7.2: **Optical images of a cantilever before the final etch step.** Small flakes of silicon are still present following KOH etching as further etching can damage the cantilever due to stiction of bubbles to the cantilevers.

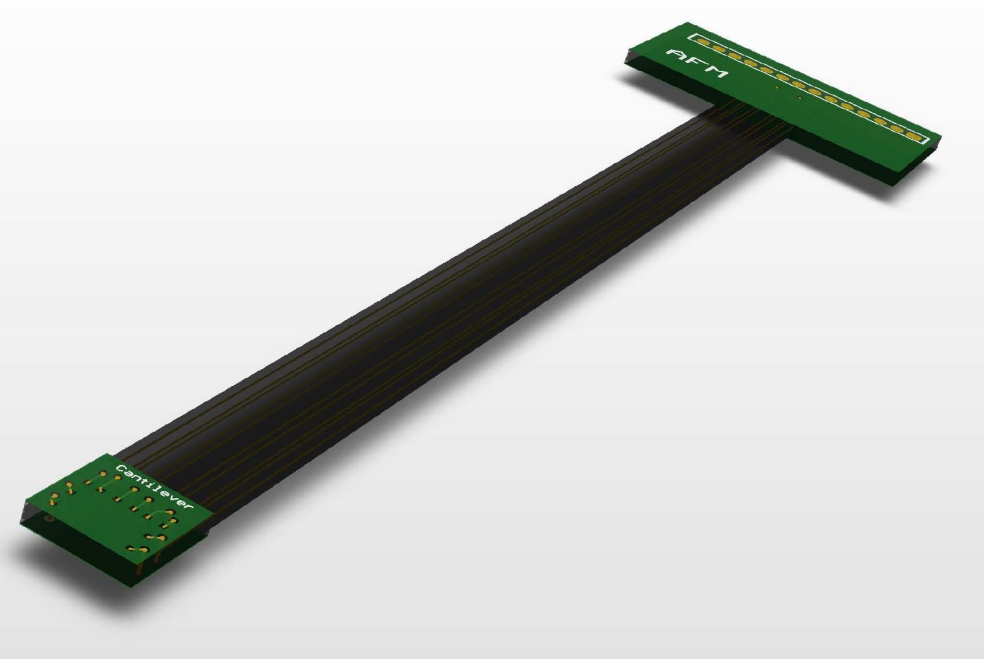

Figure 7.3: **3D projection of the PCB support for the cantilever array.** This was utilized as a mechanical support for mounting the cantilever in the AFM.

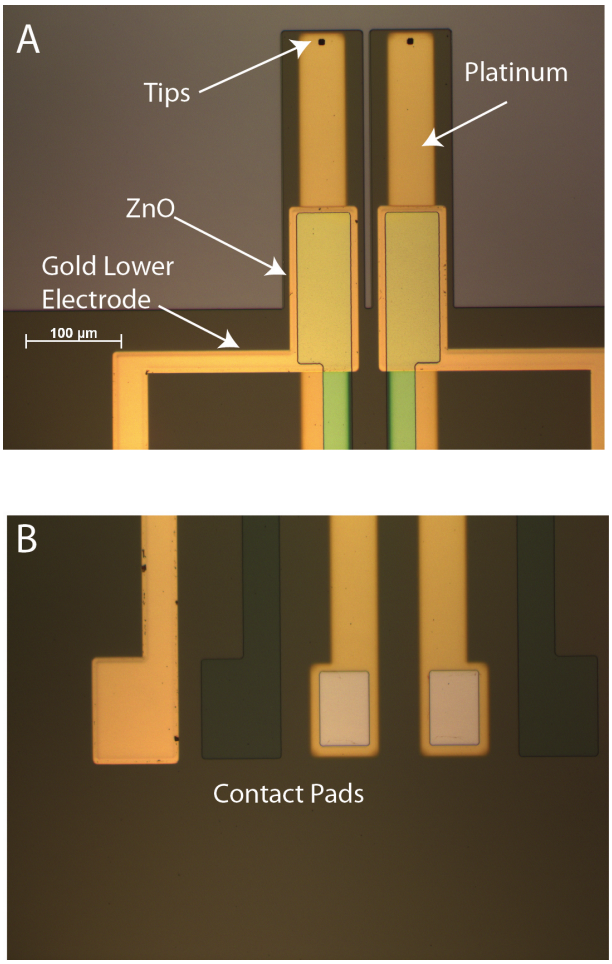

Figure 7.4: **Optical images of a partially fabricated parallel cantilever.** **(A)** The cantilevers with the piezoelectric-actuation shaped components are shown. The tips have been coated with platinum and further insulated with silicon nitride. **(B)** The contact pads are shown for inputting electrical signals.

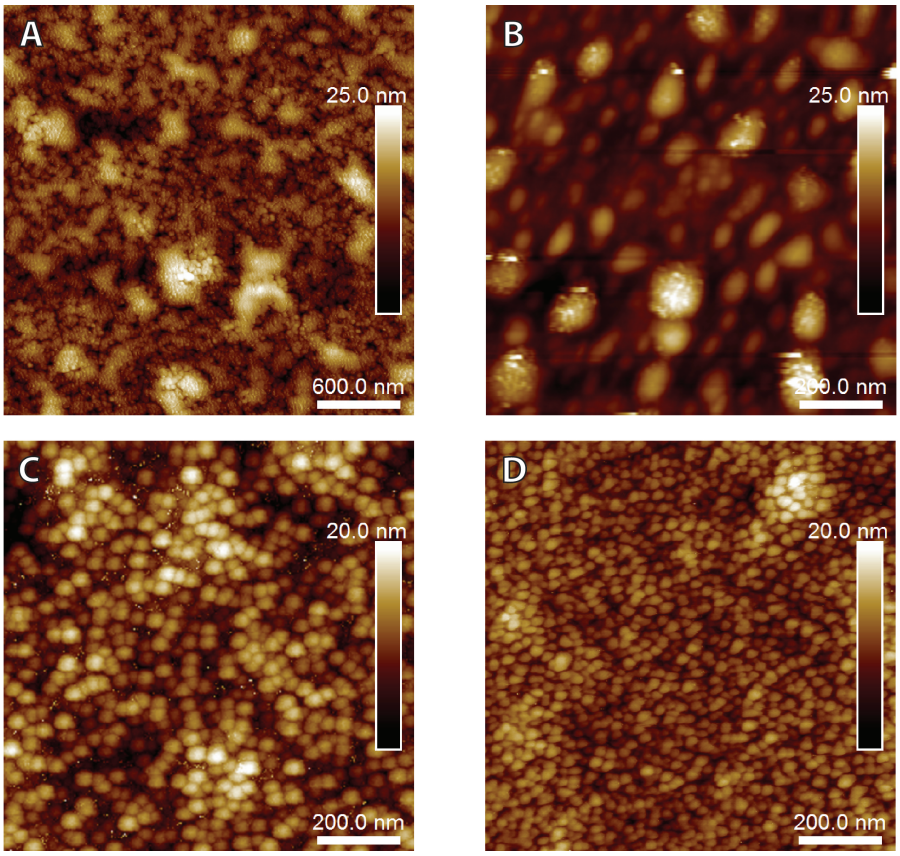

Figure 7.5: **AFM images of ZnO films deposited at different sputtering pressures.** **(A)** 2 mT. **(B)** 5 mT. **(C)** 7 mT. **(D)** 10 mT.

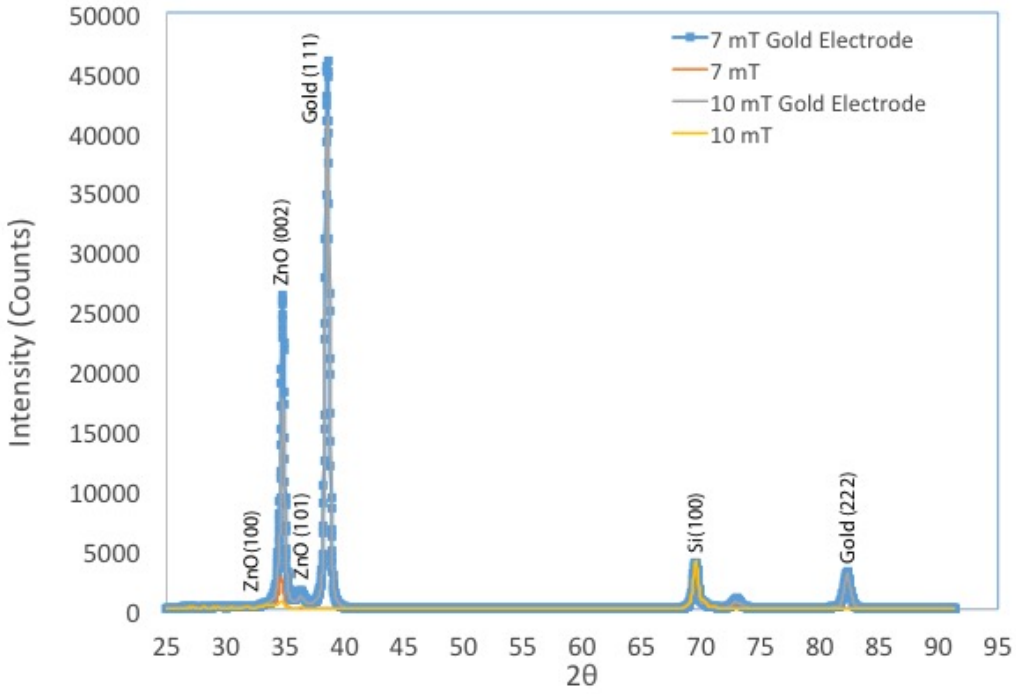

Figure 7.6: **X-ray diffraction spectra of ZnO films grown under different sputter pressures.** Gold substrates showed greater orientation of ZnO crystals compared with silicon nitride substrates. Films grown under 7 mT pressure showed the strongest x-ray diffraction intensity in the preferred orientation (ZnO 002).

Bibliography

[1] Binnig G, Rohrer H (1983) Scanning tunneling microscopy. Surface Science 126: 236 - 244.

[2] Binnig G, Quate CF, Gerber C (1986) Atomic force microscope. Physics Review Letters 56: 930–.

[3] Hansma PK, Drake B, Marti O, Gould SAC, Prater CB (1989) The scanning ion-conductance microscope. Science 243: 641–643.

[4] Bard AJ (1991) Chemical imaging of surfaces with the scanning electrochemical microscope. Science 254: 68–74.

[5] Hillner P, Walters D, Lal R, Hansma H, Hansma R (1995) Combined atomic force and confocal laser scanning microscope. Microscopy and Microanalysis 1: 127–130.

[6] Williams CC, Wickramasinghe HK (1986) Scanning thermal profiler. Applied Physics Letters 49: 1587–1589.

[7] Almqvist N, Bhatia R, Primbs G, Desai N, Banerjee S, Lal R (2004) Elasticity and adhesion force mapping reveals real-time clustering of growth factor receptors and associated changes in local cellular rheological properties. Biophysical Journal 86: 1753 - 1762.

[8] Alexander S, Hellemans L, Marti O, Schneir J, Elings V, Hansma PK, Longmire M, Gurley J (1989) An atomic–resolution atomic–force microscope implemented using an optical lever. Journal of Applied Physics 65: 164-167.

[9] Martin Y, Abraham DW, Wickramasinghe HK (1988) High-resolution capacitance measurement and potentiometry by force microscopy. Applied Physics Letters 52: 1103-1105.

[10] Tortonese M, Barrett RC, Quate CF (1993) Atomic resolution with an atomic force microscope using piezoresistive detection. Applied Physics Letters 62: 834-836.

[11] Hansma PK, Cleveland JP, Radmacher M, Walters DA, Hillner PE, Bezanilla M, Fritz M, Vie D, Hansma HG, Prater CB, Massie J, Fukunaga L, Gurley J, Elings V (1994) Tapping mode atomic force microscopy in liquids. Applied Physics Letters 64: 1738-1740.

[12] Kwok J, Grogan S, Meckes B, Arce F, Lal R, D'Lima D (2014) Atomic force microscopy reveals age-dependent changes in nanomechanical properties of the extracellular matrix of native human menisci: implications for joint degeneration and osteoarthritis. Nanomedicine: Nanotechnology, Biology and Medicine 10: 1777 - 1785.

[13] Arce FT, Meckes B, Camp SM, Garcia JG, Dudek SM, Lal R (2013) Heterogeneous elastic response of human lung microvascular endothelial cells to barrier modulating stimuli. Nanomedicine: Nanotechnology, Biology and Medicine 9: 875 - 884.

[14] Cross SE, Jin YS, Rao J, Gimzewski JK (2007) Nanomechanical analysis of cells from cancer patients. Nature Nanotechnology 2: 780–783.

[15] Butt HJ, Jaschke M (1995) Calculation of thermal noise in atomic force microscopy. Nanotechnology 6: 1.

[16] Hillner PE, Gratz AJ, Manne S, Hansma PK (1992) Atomic-scale imaging of calcite growth and dissolution in real time. Geology 20: 359-362.

[17] Giessibl FJ (1995) Atomic resolution of the silicon (111)-(7×7) surface by atomic force microscopy. Science 267: 68-71.

[18] Gross L, Mohn F, Moll N, Liljeroth P, Meyer G (2009) The chemical structure of a molecule resolved by atomic force microscopy. Science 325: 1110-1114.

[19] Weisenhorn AL, Egger M, Ohnesorge F, Gould SAC, Heyn SP, Hansma HG, Sinsheimer RL, Gaub HE, Hansma PK (1991) Molecular-resolution images of Langmuir-Blodgett films and DNA by atomic force microscopy. Langmuir 7: 8-12.

[20] Shinozaki Y, Sumitomo K, Tsuda M, Koizumi S, Inoue K, Torimitsu K (2009) Direct observation of ATP-induced conformational changes in single $P2X_4$ receptors. PLoS Biology 7: e1000103.

[21] Thimm J, Mechler A, Lin H, Rhee S, Lal R (2005) Calcium-dependent open/closed conformations and interfacial energy maps of reconstituted hemichannels. Journal of Biological Chemistry 280: 10646–10654.

[22] Allen MJ, Tung VC, Kaner RB (2010) Honeycomb carbon: A review of graphene. Chemical Reviews 110: 132–145.

[23] Müller DJ, Engel A (1999) Voltage and pH-induced channel closure of porin OmpF visualized by atomic force microscopy. Journal of Molecular Biology 285: 1347 - 1351.

[24] Walters DA, Cleveland JP, Thomson NH, Hansma PK, Wendman MA, Gurley G, Elings V (1996) Short cantilevers for atomic force microscopy. Review of Scientific Instruments 67: 3583-3590.

[25] Viani MB, Schäffer TE, Paloczi GT, Pietrasanta LI, Smith BL, Thompson JB, Richter M, Rief M, Gaub HE, Plaxco KW, Cleland AN, Hansma HG, Hansma PK (1999) Fast imaging and fast force spectroscopy of single biopolymers with a new atomic force microscope designed for small cantilevers. Review of Scientific Instruments 70: 4300–4303.

[26] Sulchek T, Hsieh R, Adams JD, Minne SC, Quate CF, Adderton DM (2000) High-speed atomic force microscopy in liquid. Review of Scientific Instruments 71: 2097-2099.

[27] Hoh J, Schoenenberger C (1994) Surface morphology and mechanical properties of MDCK monolayers by atomic force microscopy. Journal of Cell Science 107: 1105-1114.

[28] Schneider S, Sritharan K, Geibel J, Oberleithner H, Jena B (1997) Surface dynamics in living acinar cells imaged by atomic force microscopy: Identification of plasma membrane structures involved in exocytosis. Proceedings of the National Academy of Sciences 94: 316-321.

[29] Quist A, Doudevski L, Lin H, Azimova R, Ng D, Frangione B, Kagan B, Ghiso J, Lal R (2005) Amyloid ion channels: A common structural link for protein-misfolding disease. Proceedings of the National Academy of Sciences 102: Biophys Soc.

[30] Quist AP, Rhee SK, Lin H, Lal R (2000) Physiological role of gap-junctional hemichannels extracellular calcium-dependent isosmotic volume regulation. The Journal of Cell Biology 148: 1063–1074.

[31] Lal R, John SA (1994) Biological applications of atomic-force microscopy. American Journal of Physiology 266: C1–C21.

[32] Engel A, Müller DJ (2000) Observing single biomolecules at work with the atomic force microscope. Nature Structural & Molecular Biology 7: 715–718.

[33] Majumdar A, Carrejo JP, Lai J (1993) Thermal imaging using the atomic force microscope. Applied Physics Letters 62: 2501-2503.

[34] Proksch R, Lal R, Hansma PK, Morse D, Stucky G (1996) Imaging the internal and external pore structure of membranes in fluid: Tapping mode scanning ion conductance microscopy. Biophysical Journal 71: 2155–2157.

[35] Kim K, Jeong W, Lee W, Reddy P (2012) Ultra-high vacuum scanning thermal microscopy for nanometer resolution quantitative thermometry. ACS Nano 6: 4248-4257.

[36] Bocker M, Muschter S, Schmitt EK, Steinem C, Schaffer TE (2009) Imaging and patterning of pore-suspending membranes with scanning ion conductance microscopy. Langmuir 25: 3022–3028.

[37] Chen CC, Derylo MA, Baker LA (2009) Measurement of ion currents through porous membranes with scanning ion conductance microscopy. Analytical Chemistry 81: 4742–4751.

[38] Gardner CE, Unwin PR, Macpherson JV (2005) Correlation of membrane structure and transport activity using combined scanning electrochemical-atomic force microscopy. Electrochemistry Communications 7: 612–618.

[39] Gullo MR, Frederix PL, Akiyama T, Engel A, deRooij NF, Staufer U (2006) Characterization of microfabricated probes for combined atomic force and high-resolution scanning electrochemical microscopy. Analytical Chemistry 78: 5436-5442.

[40] Macpherson JV, Jones CE, Barker AL, Unwin PR (2002) Electrochemical imaging of diffusion through single nanoscale pores. Analytical Chemistry 74: 1841–1848.

[41] Burt DP, Wilson NR, Weaver JMR, Dobson PS, Macpherson JV (2005) Nanowire probes for high resolution combined scanning electrochemical microscopy-atomic force microscopy. Nano Letters 5: 639–643.

[42] Frederix PLTM (2005) Assessment of insulated conductive cantilevers for biology and electrochemistry. Nanotechnology 16: 997–.

[43] Macpherson JV, Unwin PR (2000) Combined scanning electrochemical-atomic force microscopy. Analytical Chemistry 72: 276–285.

[44] Schäffer TE, Ionescu-Zanetti C, Proksch R, Fritz M, Walters DA, Almqvist N, Zaremba CM, Belcher AM, Smith BL, Stucky GD, Morse D, Hansma PK (1997) Does abalone nacre form by heteroepitaxial nucleation or by growth through mineral bridges? Chemistry of Materials 9: 1731–1740.

[45] Novak P, Li C, Shevchuk AI, Stepanyan R, Caldwell M, Hughes S, Smart TG, Gorelik J, Ostanin VP, Lab MJ, Moss GWJ, Frolenkov GI, Klenerman

D, Korchev YE (2009) Nanoscale live-cell imaging using hopping probe ion conductance microscopy. Nature Methods 6: 279–281.

[46] Korchev YE, Negulyaev YA, Edwards CR, Vodyanoy I, Lab MJ, et al. (2000) Functional localization of single active ion channels on the surface of a living cell. Nature cell biology 2: 616–619.

[47] Goodenough DA, Paul DL (2009) Gap junctions. Cold Spring Harbor Perspectives in Biology 1: a002576.

[48] Makowski L, Caspar DLD, Phillips WC, Good DA (1977) Gap junction structures: Analysis of X-ray-diffraction data. Journal of Cell Biology 74: 629–645.

[49] Sorgen PL, Duffy HS, Sahoo P, Coombs W, Delmar M, Spray DC (2004) Structural changes in the carboxyl terminus of the gap junction protein connexin43 indicates signaling between binding domains for c-Src and zonula occludens-1. Journal of Biological Chemistry 279: 54695–54701.

[50] He DS, Jiang JX, Taffet SM, Burt JM (1999) Formation of heteromeric gap junction channels by connexins 40 and 43 in vascular smooth muscle cells. Proceedings of the National Academy of Sciences 96: 6495-6500.

[51] Jiang JX, Goodenough DA (1996) Heteromeric connexons in lens gap junction channels. Proceedings of the National Academy of Sciences 93: 1287-1291.

[52] Barrio LC, Suchyna T, Bargiello T, Xu LX, Roginski RS, Bennett MV, Nicholson BJ (1991) Gap junctions formed by connexins 26 and 32 alone and in combination are differently affected by applied voltage. Proceedings of the National Academy of Sciences 88: 8410-8414.

[53] Bruinsma R, Goulian M, Pincus P (1994) Self-assembly of membrane junctions. Biophysical Journal 67: 746–750.

[54] Bruinsma R, Pincus P (1996) Protein aggregation in membranes. Current Opinion in Solid State and Materials Science 1: 401 - 406.

[55] Bukauskas FF, Jordan K, Bukauskiene A, Bennett MVL, Lampe PD, Laird DW, Verselis VK (2000) Clustering of connexin 43-enhanced green fluorescent protein gap junction channels and functional coupling in living cells. Proceedings of the National Academy of Sciences 97: 2556–2561.

[56] Bennett MV, Contreras JE, Bukauskas FF, Sáez JC (2003) New roles for astrocytes: Gap junction hemichannels have something to communicate. Trends in Neurosciences 26: 610 - 617.

[57] Kumar NM, Gilula NB (1996) The gap junction communication channel. Cell 84: 381 - 388.

[58] Lo C (1996) The role of gap junction membrane channels in development. Journal of Bioenergetics and Biomembranes 28: 379-385.

[59] Levin M, Mercola M (1998) Gap junctions are involved in the early generation of left–right asymmetry. Developmental Biology 203: 90 - 105.

[60] Krutovskikh VA, Piccoli C, Yamasaki H, Yamasaki H (2002) Gap junction intercellular communication propagates cell death in cancerous cells. Oncogene 21: 1989—1999.

[61] Krysko D, Leybaert L, Vandenabeele P, D'Herde K (2005) Gap junctions and the propagation of cell survival and cell death signals. Apoptosis 10: 459-469.

[62] Stout CE, Costantin JL, Naus CCG, Charles AC (2002) Intercellular calcium signaling in astrocytes via ATP release through connexin hemichannels. Journal of Biological Chemistry 277: 10482-10488.

[63] Contreras JE, Sánchez HA, Véliz LP, Bukauskas FF, Bennett MV, Sáez JC (2004) Role of connexin-based gap junction channels and hemichannels in ischemia-induced cell death in nervous tissue. Brain Research Reviews 47: 290 - 303.

[64] Jiang JX, Siller-Jackson AJ, Burra S (2007) Roles of gap junctions and hemichannels in bone cell functions and in signal transmission of mechanical stress. Frontiers in Bioscience: a Journal and Virtual Library 12: 1450.

[65] Lal R, John SA, Laird DW, Arnsdorf MF (1995) Heart gap junction preparations reveal hemiplaques by atomic-force microscopy. American Journal of Physiology-Cell Physiology 268: C968–C977.

[66] Fiori MC, Figueroa V, Zoghbi ME, Saez JC, Reuss L, Altenberg GA (2012) Permeation of calcium through purified connexin 26 hemichannels. Journal of Biological Chemistry 287: 40826–40834.

[67] De Vuyst E, Decrock E, Cabooter L, Dubyak GR, Naus CC, Evans WH, Leybaert L (2005) Intracellular calcium changes trigger connexin 32 hemichannel opening. The EMBO Journal 25: 34–44.

[68] Allen MJ, Gemel J, Beyer EC, Lal R (2011) Atomic force microscopy of connexin40 gap junction hemichannels reveals calcium-dependent three-dimensional molecular topography and open-closed conformations of both the extracellular and cytoplasmic faces. Journal of Biological Chemistry 286: 22139–22146.

[69] Müller DJ, Hand GM, Engel A, Sosinsky GE (2002) Conformational changes in surface structures of isolated connexin 26 gap junctions. EMBO Journal 21: 3598–3607.

[70] Contreras JE, Sáez JC, Bukauskas FF, Bennett MVL (2003) Gating and regulation of connexin 43 (Cx43) hemichannels. Proceedings of the National Academy of Sciences 100: 11388–11393.

[71] Chen J, Gao Y, Zeng F, Li D, Pan F (2004) Effect of sputtering oxygen partial pressures on structure and physical properties of high resistivity ZnO films. Applied Surface Science 223: 318–329.

[72] Li HY, Liu TF, Lazrak A, Peracchia C, Goldberg GS, Lampe PD, Johnson RG (1996) Properties and regulation of gap junctional hemichannels in the plasma membranes of cultured cells. Journal of Cell Biology 134: 1019–1030.

[73] Mattson MP (2004) Pathways towards and away from Alzheimer's disease. Nature 430: 631–639.

[74] Ramachandran S, Xie LH, John SA, Subramaniam S, Lal R (2007) A novel role for connexin hemichannel in oxidative stress and smoking-induced cell injury. PLOS ONE 2: e712.

[75] Mattson MP, Chan SL (2003) Calcium orchestrates apoptosis. Nature Cell Biology 5: 1041–1043.

[76] Boehning D, Patterson RL, Sedaghat L, Glebova NO, Kurosaki T, Snyder SH (2003) Cytochrome c binds to inositol (1,4,5) trisphosphate receptors, amplifying calcium-dependent apoptosis. Nature Cell Biology 5: 1051–1061.

[77] Orrenius S, Zhivotovsky B, Nicotera P (2003) Regulation of cell death: the calcium-apoptosis link. Nature Review of Cellular Molecular Biology 4: 552–565.

[78] Oshima A, Tani K, Hiroaki Y, Fujiyoshi Y, Sosinsky GE (2007) Three-dimensional structure of a human connexin26 gap junction channel reveals a plug in the vestibule. Proceedings of the National Academy of Sciences 104: 10034–10039.

[79] Maeda S, Nakagawa S, Suga M, Yamashita E, Oshima A, Fujiyoshi Y, Tsukihara T (2009) Structure of the connexin 26 gap junction channel at 3.5 angstrom resolution. Nature 458: 597–U61.

[80] Unger VM, Kumar NM, Gilula NB, Yeager M (1999) Three-dimensional structure of a recombinant gap junction membrane channel. Science 283: 1176–1180.

[81] Bukauskas F, Elfgang C, Willecke K, Weingart R (1995) Heterotypic gap junction channels (connexin26 – connexin32) violate the paradigm of unitary conductance. Pflügers Archiv 429: 870-872.

[82] Suchyna TM, Nitsche JM, Chilton M, Harris AL, Veenstra RD, Nicholson BJ (1999) Different ionic selectivities for connexins 26 and 32 produce rectifying gap junction channels. Biophysical Journal 77: 2968 - 2987.

[83] Gerido DA, DeRosa AM, Richard G, White TW (2007) Aberrant hemichannel properties of cx26 mutations causing skin disease and deafness. American Journal of Physiology - Cell Physiology 293: C337–C345.

[84] Levit NA, Sellitto C, Wang HZ, Li L, Srinivas M, Brink PR, White TW (2014) Aberrant connexin26 hemichannels underlying Keratitis–Ichthyosis–Deafness Syndrome are potently inhibited by mefloquine. Journal of Investigative Dermatology .

[85] Ambrosi C, Boassa D, Pranskevich J, Smock A, Oshima A, Xu J, Nicholson BJ, Sosinsky GE (2010) Analysis of four connexin26 mutant gap junctions and hemichannels reveals variations in hexamer stability. Biophysical Journal 98: 1809–1819.

[86] Bruzzone R, Veronesi V, Gomès D, Bicego M, Duval N, Marlin S, Petit C, D'Andrea P, White T (2003) Loss-of-function and residual channel activity of connexin26 mutations associated with non-syndromic deafness. FEBS Letters 533: 79 - 88.

[87] Lee JR, DeRosa AM, White TW (2008) Connexin mutations causing skin disease and deafness increase hemichannel activity and cell death when expressed in xenopus oocytes. Journal of Investigative Dermatology 129: 870–878.

[88] Fan FRF, Bard AJ (1999) Imaging of biological macromolecules on mica in humid air by scanning electrochemical microscopy. Proceedings of the National Academy of Sciences 96: 14222–14227.

[89] Korchev YE, Bashford CL, Milovanovic M, Vodyanoy I, Lab MJ (1997) Scanning ion conductance microscopy of living cells. Biophysical Journal 73: 653–658.

[90] Shevchuk AI (2006) Imaging proteins in membranes of living cells by high-resolution scanning ion conductance microscopy. Angewandte Chemie-international Edition 45: 2212–2216.

[91] Quist AP, Chand A, Ramachandran S, Daraio C, Jin S, Lal R (2007) Atomic force microscopy imaging and electrical recording of lipid bilayers supported

over microfabricated silicon chip nanopores: Lab-on-a-chip system for lipid membranes and ion channels. Langmuir 23: 1375–1380.

[92] Derylo MA, Morton KC, Baker LA (2011) Parylene insulated probes for scanning electrochemical-atomic force microscopy. Langmuir 27: 13925–13930.

[93] Wain AJ, Cox D, Zhou S, Turnbull A (2011) High-aspect ratio needle probes for combined scanning electrochemical microscopy - atomic force microscopy. Electrochemistry Communications 13: 78–81.

[94] Borzenets IV, Yoon I, Prior WM, Donald BR, Mooney RD, Finkelstein G (2012) Ultra-sharp metal and nanotube-based probes for applications in scanning microscopy and neural recording. Journal of Applied Physics 111: 074703.

[95] Bryant PJ, Kim HS, Zheng YC, Yang R (1987) Technique for shaping scanning tunneling microscope tips. Review of Scientific Instruments 58: 1115–.

[96] Angle MR, Schaefer AT (2012) Neuronal recordings with solid-conductor intracellular nanoelectrodes (SCINEs). PLOS ONE 7: e43194.

[97] Schulte A, Chow RH (1996) A simple method for insulating carbon-fiber microelectrodes using anodic electrophoretic deposition of paint. Analytical Chemistry 68: 3054–3058.

[98] Abbou J, Demaille C, Druet M, Moiroux J (2002) Fabrication of submicrometer-sized gold electrodes of controlled geometry for scanning electrochemical-atomic force microscopy. Analytical Chemistry 74: 6355–6363.

[99] Fantner GE, Barbero RJ, Gray DS, Belcher AM (2010) Kinetics of antimicrobial peptide activity measured on individual bacterial cells using high-speed atomic force microscopy. Nature Nanotechnology 5: 280–285.

[100] Bearinger JP, Orme CA, Gilbert JL (2001) Direct observation of hydration of TiO_2 on ti using electrochemical AFM: freely corroding versus potentiostatically held conditions. Surface Science 491: 370–387.

[101] Szunerits S, Pust SE, Wittstock G (2007) Multidimensional electrochemical imaging in materials science. Analytical and Bioanalytical Chemistry 389: 1103–1120.

[102] Davoodi A, Pan J, Leygraf C, Norgren S (2005) In situ investigation of localized corrosion of aluminum alloys in chloride solution using integrated EC-AFM/SECM techniques. Electrochemical and Solid State Letters 8: B21–B24.

[103] Wold DJ, Frisbie CD (2001) Fabrication and characterization of metal-molecule-metal junctions by conducting probe atomic force microscopy. Journal of the American Chemical Society 123: 5549–5556.

[104] Davis JJ, Morgan DA, Wrathmell CL, Axford DN, Zhao J, Wang N (2005) Molecular bioelectronics. Journal of Materials Chemistry 15: 2160–2174.

[105] Masuda T, Ikeda K, Uosaki K (2013) Potential-dependent adsorption/desorption behavior of perfluorosulfonated ionomer on a gold electrode surface studied by cyclic voltammetry, electrochemical quartz microbalance, and electrochemical atomic force microscopy. Langmuir 29: 2420–2426.

[106] Elving PJ, Schmakel CO, Santhanam KSV (1976) Nicotinamide nad sequence redox processes and related behavior behavior and properties of intermediate and final products. Critical Reviews in Analytical Chemistry 6: 1–67.

[107] Tse DCS, Kuwana T (1978) Electrocatalysis of dihydronicotinamide adenosine-diphosphate with quinones and modified quinone electrodes. Analytical Chemistry 50: 1315–1318.

[108] Jaegfeldt H, Kuwana T, Johansson G (1983) Electrochemical stability of catechols with a pyrene side-chain strongly adsorbed on graphite-electrodes for catalytic-oxidation of dihydronicotinamide adenine-dinucleotide. Journal of the American Chemical Society 105: 1805–1814.

[109] Periasamy AP, Umasankar Y, Chen SM (2011) Toluidine blue adsorbed on alcohol dehydrogenase modified glassy carbon electrode for voltammetric determination of ethanol. Talanta 83: 930–936.

[110] Amir L, Carnally SA, Rayo J, Rosenne S, Yerushalmi SM, Schlesinger O, Meijler MM, Alfonta L (2013) Surface display of a redox enzyme and its site-specific wiring to gold electrodes. Journal of the American Chemical Society 135: 70–73.

[111] Maurer J, Jose J, Meyer TF (1997) Autodisplay: One-component system for efficient surface display and release of soluble recombinant proteins from Escherichia coli. Journal of Bacteriology 179: 794–804.

[112] Chin JW, Santoro SW, Martin AB, King DS, Wang L, Schultz PG (2002) Addition of p-azido-L-phenylaianine to the genetic code of Escherichia coli. Journal of the American Chemical Society 124: 9026–9027.

[113] Kolb HC, Finn MG, Sharpless KB (2001) Click chemistry: Diverse chemical function from a few good reactions. Angewandte Chemie-international Edition 40: 2004–2021.

[114] Jose J, Maas RM, Teese MG (2012) Autodisplay of enzymes-molecular basis and perspectives. Journal of Biotechnology 161: 92–103.

[115] Laviron E (1979) General expression of the linear potential sweep voltammogram in the case of diffusionless electrochemical systems. Journal of Electroanalytical Chemistry 101: 19–28.

[116] Gorton L (1986) Chemically modified electrodes for the electrocatalytic oxidation of nicotinamide coenzymes. Journal of the Chemical Society-Faraday Transactions I 82: 1245–1258.

[117] Gaßmann O, Kreir M, Ambrosi C, Pranskevich J, Oshima A, Roeling C, Sosinsky G, Fertig N, Steinem C (2009) The M34A mutant of connexin26 reveals active conductance states in pore-suspending membranes. Journal of Structural Biology 168: 168–176.

[118] Ramachandran S, Arce FT, Patel NR, Quist AP, Cohen DA, Lal R (2014) Structure and permeability of ion-channels by integrated AFM and waveguide TIRF microscopy. Scientific Reports 4: 4424.

[119] Harris AL (2007) Connexin channel permeability to cytoplasmic molecules. Progress In Biophysics & Molecular Biology 94: 120–143.

[120] Axelsen LN, Calloe K, Holstein-Rathlou NH, Nielsen MS (2013) Managing the complexity of communication: regulation of gap junctions by post-translational modification. Frontiers in Pharmacology 4.

[121] Kondo RP, Wang SY, John SA, Weiss JN, Goldhaber JI (2000) Metabolic inhibition activates a non selective current through connexin hemichannels in isolated ventricular myocytes. Journal of Molecular and Cellular Cardiology 32: 1859–1872.

[122] Paul DL, Ebihara L, Takemoto LJ, Swenson KI, Goodenough DA (1991) Connexin46, a novel lens gap junction protein, induces voltage-gated currents in nonjunctional plasma-membrane of xenopus oocytes. Journal of Cell Biology 115: 1077–1089.

[123] Retamal MA, Cortes CJ, Reuss L, Bennett MVL, Saez JC (2006) S-nitrosylation and permeation through connexin 43 hemichannels in astrocytes: Induction by oxidant stress and reversal by reducing agents. Proceedings of the National Academy of Sciences 103: 4475–4480.

[124] Yu J, Bippes CA, Hand GM, Müller DJ, Sosinsky GE (2007) Aminosulfonate modulated pH-induced conformational changes in connexin26 hemichannels. Journal of Biological Chemistry 282: 8895–8904.

[125] Pfenniger A, Wohlwend A, Kwak BR (2011) Mutations in connexin genes and disease. European Journal of Clinical Investigation 41: 103–116.

[126] Ambrosi C, Walker AE, DePriest AD, Cone AC, Lu C, Badger J, Skerrett M, Sosinsky GE (2013) Analysis of trafficking, stability and function of human connexin 26 gap junction channels with deafness-causing mutations in the fourth transmembrane helix. PLOS ONE 8: e70916.

[127] Xu J, Nicholson BJ (2013) The role of connexins in ear and skin physiology - functional insights from disease-associated mutations. Biochimica Et Biophysica Acta-Biomembranes 1828: 167–178.

[128] Beahm DL, Oshima A, Gaietta GM, Hand GM, Smock AE, Zucker SN, Toloue MM, Chandrasekhar A, Nicholson BJ, Sosinsky GE (2006) Mutation of a conserved threonine in the third transmembrane helix of alpha- and beta-connexins creates a dominant-negative closed gap junction channel. Journal of Biological Chemistry 281: 7994–8009.

[129] Ambrosi C, Gaßmann O, Pranskevich JN, Boassa D, Smock A, Wang J, Dahl G, Steinem C, Sosinsky GE (2010) Pannexin1 and pannexin2 channels show quaternary similarities to connexons and different oligomerization numbers from each other. Journal of Biological Chemistry 285: 24420–24431.

[130] Oshima A, Tani K, Toloue MM, Hiroaki Y, Smock A, Inukai S, Cone A, Nicholson BJ, Sosinsky GE, Fujiyoshi Y (2011) Asymmetric configurations and n-terminal rearrangements in connexin26 gap junction channels. Journal of Molecular Biology 405: 724–735.

[131] Hand GM, Müller DJ, Nicholson BJ, Engel A, Sosinsky GE (2002) Isolation and characterization of gap junctions from tissue culture cells. Journal of Molecular Biology 315: 587–600.

[132] Leonenko ZV, Finot E, Ma H, Dahms TES, Cramb DT (2004) Investigation of temperature-induced phase transitions in DOPC and DPPC phospholipid bilayers using temperature-controlled scanning force microscopy. Biophysical Journal 86: 3783–3793.

[133] Musil LS, Le ACN, VanSlyke JK, Roberts LM (2000) Regulation of connexin degradation as a mechanism to increase gap junction assembly and function. Journal of Biological Chemistry 275: 25207–25215.

[134] Abney JR, Braun J, Owicki JC (1987) Lateral interactions among membrane-proteins - implications for the organization of gap-junctions. Biophysical Journal 52: 441–454.

[135] Braun J, Abney JR, Owicki JC (1984) How a gap junction maintains its structure. Nature 310: 316–318.

[136] Baker SM, Buckheit I Robert W, Falk MM (2010) Green-to-red photoconvertible fluorescent proteins: tracking cell and protein dynamics on standard wide-field mercury arc-based microscopes. BMC Cell Biology 11: 15.

[137] Lauf U, Giepmans BNG, Lopez P, Braconnot S, Chen SC, Falk MM (2002) Dynamic trafficking and delivery of connexons to the plasma membrane and accretion to gap junctions in living cells. Proceedings of the National Academy of Sciences 99: 10446–10451.

[138] Lal R, Yu L (1993) Atomic-force microscopy of cloned nicotinic acetylcholine-receptor expressed in xenopus-oocytes. Proceedings of the National Academy of Sciences 90: 7280–7284.

[139] Rico F, Oshima A, Hinterdorfer P, Fujiyoshi Y, Scheuring S (2011) Two-dimensional kinetics of inter-connexin interactions from single-molecule force spectroscopy. Journal of Molecular Biology 412: 72–79.

[140] Johnson RG, Hammer M, Sheridan J, Revel JP (1974) Gap junction formation between reaggregated novikoff hepatoma-cells. Proceedings of the National Academy of Sciences 71: 4536–4540.

[141] Merchant CA, Healy K, Wanunu M, Ray V, Peterman N, Bartel J, Fischbein MD, Venta K, Luo Z, Johnson ATC, Drndic M (2010) DNA translocation through graphene nanopores. Nano Letters 10: 2915–2921.

[142] Chang H, Kosari F, Andreadakis G, Alam MA, Vasmatzis G, Bashir R (2004) DNA-mediated fluctuations in ionic current through silicon oxide nanopore channels. Nano Letters 4: 1551–1556.

[143] Wanunu M, Sutin J, McNally B, Chow A, Meller A (2008) DNA translocation governed by interactions with solid-state nanopores. Biophysical Journal 95: 4716–4725.

[144] Wanunu M, Meller A (2007) Chemically modified solid-state nanopores. Nano Letters 7: 1580–1585.

[145] Branton D, Deamer DW, Marziali A, Bayley H, Benner SA, Butler T, Di Ventra M, Garaj S, Hibbs A, Huang X, Jovanovich SB, Krstic PS, Lindsay S, Ling XS, Mastrangelo CH, Meller A, Oliver JS, Pershin YV, Ramsey JM, Riehn R, Soni GV, Tabard-Cossa V, Wanunu M, Wiggin M, Schloss JA (2008) The potential and challenges of nanopore sequencing. Nature Biotechnology 26: 1146–1153.

[146] Jackson EA, Hillmyer MA (2010) Nanoporous membranes derived from block copolymers: From drug delivery to water filtration. ACS Nano 4: 3548–3553.

[147] O'Regan B, Gratzel M (1991) A low-cost, high-efficiency solar-cell based on dye-sensitized colloidal TiO_2 films. Nature 353: 737–740.

[148] Wang D, Zhang Y, Wang J, Peng C, Huang Q, Su S, Wang L, Huang W, Fan C (2014) Template-free synthesis of hematite photoanodes with nanostructured ATO conductive underlayer for PEC water splitting. ACS Applied Materials & Interfaces 6: 36–40.

[149] Sanchez C, Boissiere C, Grosso D, Laberty C, Nicole L (2008) Design, synthesis, and properties of inorganic and hybrid thin films having periodically organized nanoporosity. Chemistry of Materials 20: 682–737.

[150] Venkatesan BM, Estrada D, Banerjee S, Jin X, Dorgan VE, Bae MH, Aluru NR, Pop E, Bashir R (2012) Stacked graphene-Al_2O_3 nanopore sensors for sensitive detection of DNA and DNA-protein complexes. ACS Nano 6: 441–450.

[151] Wanunu M, Dadosh T, Ray V, Jin J, McReynolds L, Drndic M (2010) Rapid electronic detection of probe-specific microRNAs using thin nanopore sensors. Nature Nanotechnology 5: 807–814.

[152] Lin H, Bhatia R, Lal R (2001) Amyloid beta protein forms ion channels: implications for Alzheimer's disease pathophysiology. Faseb Journal 15: 2433–2444.

[153] Dobson CM (2003) Protein folding and misfolding. Nature 426: 884–890.

[154] Fotiadis D, Scheuring S, Müller SA, Engel A, Müller DJ (2002) Imaging and manipulation of biological structures with the AFM. Micron 33: PII S0968-4328(01)00026-9.

[155] Horber JKH, Miles MJ (2003) Scanning probe evolution in biology. Science 302: 1002–1005.

[156] Pelling AE, Li YN, Shi WY, Gimzewski JK (2005) Nanoscale visualization and characterization of *myxococcus xanthus* cells with atomic force microscopy. Proceedings of the National Academy of Sciences 102: 6484–6489.

[157] Czajkowsky DM, Iwamoto H, Cover TL, Shao ZF (1999) The vacuolating toxin from helicobacter pylori forms hexameric pores in lipid bilayers at low pH. Proceedings of the National Academy of Sciences 96: 2001–2006.

[158] Connelly L, Jang H, Arce FT, Capone R, Kotler SA, Ramachandran S, Kagan BL, Nussinov R, Lal R (2012) Atomic force microscopy and MD simulations reveal pore-like structures of all-D-enantiomer of alzheimer's beta-amyloid peptide: Relevance to the ion channel mechanism of AD pathology. Journal of Physical Chemistry B 116: 1728–1735.

[159] Connelly L, Jang H, Arce FT, Ramachandran S, Kagan BL, Nussinov R, Lal R (2012) Effects of point substitutions on the structure of toxic alzheimer's beta-amyloid channels: Atomic force microscopy and molecular dynamics simulations. Biochemistry 51: 3031–3038.

[160] Lal R, Kim H, Garavito RM, Arnsdorf MF (1993) Imaging of reconstituted biological channels at molecular resolution by atomic-force microscopy. American Journal of Physiology 265: C851–C856.

[161] Lal R (1996) Imaging molecular structure of channels and receptors with an atomic force microscope. Scanning Microscopy Supplement 10: 81–95;.

[162] Yang J, Tamm LK, Tillack TW, Shao Z (1993) New approach for atomic force microscopy of membrane-proteins - the imaging of cholera-toxin. Journal of Molecular Biology 229: 286–290.

[163] Hansma PK, ELINGS VB, MARTI O, BRACKER CE (1988) Scanning tunneling microscopy and atomic force microscopy - application to biology and technology. Science 242: 209–216.

[164] Lal R, Arnsdorf MF (2010) Multidimensional atomic force microscopy for drug discovery: a versatile tool for defining targets, designing therapeutics and monitoring their efficacy. Life Sciences 86: 545–62.

[165] Ionescu-Zanetti C, Cheung K, Lal R, Lee LP (2003) Simultaneous imaging of ionic conductivity and morphology of a microfluidic system. Journal of Applied Physics 93: 10134–10136.

[166] Venkatesan BM, Bashir R (2011) Nanopore sensors for nucleic acid analysis. Nature Nanotechnology 6: 615–624.

[167] Wanunu M (2012) Nanopores: A journey towards DNA sequencing. Physics of Life Reviews 9: 125–158.

[168] Bahrami A, Dogan F, Japrung D, Albrecht T (2012) Solid-state nanopores for biosensing with submolecular resolution. Biochemical Society Transactions 40: 624–628.

[169] Iqbal SM, Bashir R (2009) Nanoelectronic-based detection for biology and medicine. Springer Handbook of Automation : 1433–1449.

[170] Jiang CY, Markutsya S, Pikus Y, Tsukruk VV (2004) Freely suspended nanocomposite membranes as highly sensitive sensors. Nature Materials 3: 721–728.

[171] Smeets RMM, Keyser UF, Krapf D, Wu MY, Dekker NH, Dekker C (2006) Salt dependence of ion transport and DNA translocation through solid-state nanopores. Nano Letters 6: 89–95.

[172] Oukhaled A, Bacri L, Pastoriza-Gallego M, Betton JM, Pelta J (2012) Sensing proteins through nanopores: Fundamental to applications. ACS Chemical Biology 7: 1935–1949.

[173] Banerjee S, Shim J, Rivera J, Jin X, Estrada D, Solovyeva V, You X, Pak J, Pop E, Aluru N, Bashir R (2013) Electrochemistry at the edge of a single graphene layer in a nanopore. ACS Nano 7: 834–843.

[174] Wells DB, Belkin M, Comer J, Aksimentiev A (2012) Assessing graphene nanopores for sequencing DNA. Nano Letters 12: 4117–4123.

[175] Storm AJ, Chen JH, Ling XS, Zandbergen HW, Dekker C (2003) Fabrication of solid-state nanopores with single-nanometre precision. Nature Materials 2: 537–540.

[176] Ennos AE (1953) The origin of specimen contamination in the electron microscope. British Journal of Applied Physics 4: 101–106.

[177] Ackerman MJ, Clapham DE (1997) Mechanisms of disease - ion channels - basic science and clinical disease. New England Journal of Medicine 336: 1575–1586.

[178] Kongsuphol P, Fang KB, Ding Z (2013) Lipid bilayer technologies in ion channel recordings and their potential in drug screening assay. Sensors and Actuators B-Chemical 185: 530–542.

[179] Venkatesan BM, Polans J, Comer J, Sridhar S, Wendell D, Aksimentiev A, Bashir R (2011) Lipid bilayer coated Al_2O_3 nanopore sensors: towards a hybrid biological solid-state nanopore. Biomedical Microdevices 13: 671–682.

[180] Garaj S, Hubbard W, Reina A, Kong J, Branton D, Golovchenko JA (2010) Graphene as a subnanometre trans-electrode membrane. Nature 467: 190–U73.

[181] Venta K, Shemer G, Puster M, Rodriguez-Manzo JA, Balan A, Rosenstein JK, Shepard K, Drndic M (2013) Differentiation of short, single-stranded DNA homopolymers in solid-state nanopores. ACS Nano 7: 4629–4636.

[182] Wonderlin WF, Finkel A, French RJ (1990) Optimizing planar lipid bilayer single-channel recordings for high-resolution with rapid voltage steps. Biophysical Journal 58: 289–297.

[183] Storm AJ, Chen JH, Zandbergen HW, Dekker C (2005) Translocation of double-strand DNA through a silicon oxide nanopore. Physical Review E 71: 051903.

[184] Yeager M, Harris AL (2007) Gap junction channel structure in the early 21st century: Facts and fantasies. Current Opinion in Cell Biology 19: 521–528.

[185] Studer A, Han X, Winkler FK, Tiefenauer LX (2009) Formation of individual protein channels in lipid bilayers suspended in nanopores. Colloids and Surfaces B-Biointerfaces 73: 325–331.

[186] Tokumasu F, Jin AJ, Dvorak JA (2002) Lipid membrane phase behaviour elucidated in real time by controlled environment atomic force microscopy. Journal of Electron Microscopy 51: 1–9.

[187] Danker T, Oberleithner H (2000) Nuclear pore function viewed with atomic force microscopy. Pflügers Archiv 439: 671-681.

[188] Hussain MA, Agnihotri A, Siedlecki CA (2005) AFM imaging of ligand binding to platelet integrin α iib β3 receptors reconstituted into planar lipid bilayers. Langmuir 21: 6979-6986.

[189] Shinozaki Y, Sumitomo K, Tsuda M, Koizumi S, Inoue K, Torimitsu K (2009) Direct observation of ATP-induced conformational changes in single $P2X_4$ receptors. PLoS Biology 7: e1000103.

[190] Kodera N, Yamamoto D, Ishikawa R, Ando T (2010) Video imaging of walking myosin V by high-speed atomic force microscopy. Nature 468: 72–76.

[191] Zhou L, Kasperek EM, Nicholson BJ (1999) Dissection of the molecular basis of pp60v-src induced gating of connexin 43 gap junction channels. The Journal of Cell Biology 144: 1033-1045.

[192] Spray D, White R, de Carvalho A, Harris A, Bennett M (1984) Gating of gap junction channels. Biophysical Journal 45: 219 - 230.

[193] Peracchia C (2004) Chemical gating of gap junction channels: Roles of calcium, pH and calmodulin. Biochimica et Biophysica Acta (BBA) - Biomembranes 1662: 61 - 80.

[194] Zelante L, Gasparini P, Estivill X, Melchionda S, D'Agruma L, Govea N, Milá M, Della Monica M, Lutfi J, Shohat M, Mansfield E, Delgrosso K, Rappaport E, Surrey S, Fortina P (1997) Connexin26 mutations associated with the most common form of non-syndromic neurosensory autosomal recessive deafness (DFNB1) in mediterraneans. Human Molecular Genetics 6: 1605-1609.

[195] Kelsell DP, Dunlop J, Stevens HP, Lench NJ, Liang JN, Parry G, Mueller RF, Leigh IM (1997) Connexin 26 mutations in hereditary non-syndromic sensorineural deafness. Nature 387: 80–83.

[196] Nollert P, Kiefer H, Jähnig F (1995) Lipid vesicle adsorption versus formation of planar bilayers on solid surfaces. Biophysical Journal 69: 1447 - 1455.

[197] Mager MD, Almquist B, Melosh NA (2008) Formation and characterization of fluid lipid bilayers on alumina. Langmuir 24: 12734-12737.

[198] Zhang Y, Qiu Z, Cheng X, Xie H, Wang H, Xie X, Yu Y, Liu R (2014) Direct growth of high-quality Al_2O_3 dielectric on graphene layers by low-temperature H_2O-based ALD. Journal of Physics D: Applied Physics 47: 055106.

[199] Tero R, Watanabe H, Urisu T (2006) Supported phospholipid bilayer formation on hydrophilicity-controlled silicon dioxide surfaces. Physical Chemistry Chemical Physics 8: 3885–3894.

[200] Sanchez HA, Bienkowski R, Slavi N, Srinivas M, Verselis VK (2014) Altered inhibition of Cx26 hemichannels by pH and Zn^{2+} in the A40V mutation associated with Keratitis-Ichthyosis-Deafness Syndrome. Journal of Biological Chemistry 289: 21519-21532.

[201] Binder H, Zschörnig O (2002) The effect of metal cations on the phase behavior and hydration characteristics of phospholipid membranes. Chemistry and Physics of Lipids 115: 39 - 61.

[202] Arispe N, Pollard HB, Rojas E (1996) Zn^{2+} interaction with alzheimer amyloid beta protein calcium channels. Proceedings of the National Academy of Sciences 93: 1710–1715.

[203] Kim YS, Nam HJ, Cho SM, Hong JW, Kim DC, Bu JU (2003) PZT cantilever array integrated with piezoresistor sensor for high speed parallel operation of AFM. Sensors and Actuators A: Physical 103: 122 - 129.

[204] Indermühle PF, Schürmann G, Racine GA, de Rooij N (1997) Fabrication and characterization of cantilevers with integrated sharp tips and piezoelectric elements for actuation and detection for parallel AFM applications. Sensors and Actuators A: Physical 60: 186 - 190.

[205] Schneider A, Ibbotson RH, Dunn RJ, Huq E (2011) Arrays of su-8 microcantilevers with integrated piezoresistive sensors for parallel AFM applications. Microelectronic Engineering 88: 2390 - 2393.

[206] Fantner GE, Schumann W, Barbero RJ, Deutschinger A, Todorov V, Gray DS, Belcher AM, Rangelow IW, Youcef-Toumi K (2009) Use of self-actuating and self-sensing cantilevers for imaging biological samples in fluid. Nanotechnology 20: 434003.

[207] Minne SC, Manalis SR, Quate CF (1995) Parallel atomic force microscopy using cantilevers with integrated piezoresistive sensors and integrated piezoelectric actuators. Applied Physics Letters 67: 3918-3920.

[208] Despont M, Brugger J, Drechsler U, Dürig U, Häberle W, Lutwyche M, Rothuizen H, Stutz R, Widmer R, Binnig G, Rohrer H, Vettiger P (2000) VLSI-NEMS chip for parallel AFM data storage. Sensors and Actuators A: Physical 80: 100 - 107.

[209] Lutwyche M, Andreoli C, Binnig G, Brugger J, Drechsler U, Haeberle W, Rohrer H, Rothuizen H, Vettiger P, Yaralioglu G, Quate C (1999) 5×5 2D AFM cantilever arrays a first step towards a terabit storage device. Sensors and Actuators A: Physical 73: 89 - 94.

[210] Mirkin CA (2007) The power of the pen: Development of massively parallel dip-pen nanolithography. ACS Nano 1: 79-83.

[211] Lenhert S, Sun P, Wang Y, Fuchs H, Mirkin CA (2007) Massively parallel dip-pen nanolithography of heterogeneous supported phospholipid multilayer patterns. Small 3: 71–75.

[212] Favre M, Polesel-Maris J, Overstolz T, Niedermann P, Dasen S, Gruener G, Ischer R, Vettiger P, Liley M, Heinzelmann H, Meister A (2011) Parallel AFM imaging and force spectroscopy using two-dimensional probe arrays for applications in cell biology. Journal of Molecular Recognition 24: 446–452.

[213] Tao Y, Fasching RJ, Prinz FB (2004). Ultrasharp high-aspect-ratio probe array for SECM and AFM analysis. doi:10.1117/12.547655.

[214] Schäffer TE, Cleveland JP, Ohnesorge F, Walters DA, Hansma PK (1996) Studies of vibrating atomic force microscope cantilevers in liquid. Journal of Applied Physics 80: 3622-3627.

[215] Kokavecz J, Mechler A (2007) Investigation of fluid cell resonances in intermittent contact mode atomic force microscopy. Applied Physics Letters 91: 023113.

[216] Xu T, Wu G, Zhang G, Hao Y (2003) The compatibility of ZnO piezoelectric film with micromachining process. Sensors and Actuators A: Physical 104: 61 - 67.

[217] Dang W, Fu Y, Luo J, Flewitt A, Milne W (2007) Deposition and characterization of sputtered ZnO films. Superlattices and Microstructures 42: 89 - 93.

[218] Lee JB, Kim HJ, Kim SG, Hwang CS, Hong SH, Shin YH, Lee NH (2003) Deposition of ZnO thin films by magnetron sputtering for a film bulk acoustic resonator. Thin Solid Films 435: 179 - 185.

[219] Puchert MK, Timbrell PY, Lamb RN (1996) Postdeposition annealing of radio frequency magnetron sputtered ZnO films. Journal of Vacuum Science & Technology A 14: 2220-2230.

[220] Wacogne B, Roe MP, Pattinson TJ, Pannell CN (1995) Effective piezoelectric activity of zinc oxide films grown by radio–frequency planar magnetron sputtering. Applied Physics Letters 67: 1674-1676.

[221] Hata T, Noda E, Morimoto O, Hada T (1980) High rate deposition of thick piezoelectric ZnO films using a new magnetron sputtering technique. Applied Physics Letters 37: 633–635.

[222] Lin RC, Chen YC, Kao KS (2007) Two-step sputtered ZnO piezoelectric films for film bulk acoustic resonators. Applied Physics A 89: 475-479.